Study of Snow Geophysical Parameters using Advanced Geospatial Techniques: Inferences from Parts of Northeastern Indian Himalayas

Thesis submitted in partial fulfillment of the requirements of the degree of

Doctor of Philosophy

By

Manmit Kumar Singh

Roll No: 196104014

Under the Supervision of

Dr. Rishikesh Bharti

DEPARTMENT OF CIVIL ENGINEERING
INDIAN INSTITUTE OF TECHNOLOGY GUWAHATI
GUWAHATI- 781039, INDIA

August 2025

Dedicated to

My Family

Indian Institute of Technology Guwahati

DECLARATION

I, Manmit Kumar Singh, declare that this Ph D thesis entitled "Study of Snow Geophysical Parameters Using Advanced Geospatial Techniques: Inferences from Parts of Northeastern Indian Himalayas" is carried out by me under the guidance of my supervisor.

I certify that,

1. This thesis is a presentation of my original research work.
2. Any part of this thesis has not been submitted for any degree or diploma or any other qualification either in this institute or in any other university.
3. Whenever I have referred to any published things or quotes from other resources, every effort has been accredited by citing them in the text of the thesis work.
4. Whenever the contributions of others are involved, I have acknowledged to indicate this.
5. I confirm that the present thesis is free from plagiarism to the best of my knowledge, and I take the whole responsibility if any complaint arises.
6. I also affirm that my supervisors are not able to check for any possible plagiarism within this submitted work.

Date: 13-August-2025

Manmit Km Singh

MANMIT KUMAR SINGH

Indian Institute of Technology Guwahati

CERTIFICATE

This is to certify that the thesis entitled " **Study of Snow Geophysical Parameters Using Advanced Geospatial Techniques: Inferences from Parts of Northeastern Indian Himalayas,** " submitted by Manmit Kumar Singh, in partial fulfillment of the requirements for the award of the degree of Doctor of Philosophy, to the Indian Institute of Technology Guwahati, Assam, India, is a record of the original bonafide research work carried out by his under our supervision and guidance at the Department of Civil Engineering, Indian Institute of Technology Guwahati, Assam, India. The thesis work, in my opinion, is worthy of consideration for the award of the degree of Doctor of Philosophy in Civil Engineering of the Institute. The work presented in this thesis has not been submitted in part or whole to any other university or institute for the award of any degree/ diploma.

Date: 13-August-2025
Place: Guwahati

Rishikesh Bharti

Dr. Rishikesh Bharti / डा० ऋषिकेश भारती
Associate Professor / सह प्राध्यापक
Department of Civil Engineering
सिविल अभियांत्रिकी विभाग
Indian Institute of Technology Guwahati
भारतीय प्रौद्योगिकी संस्थान गुवाहाटी
गुवाहाटी-781039, भारत
Guwahati-781039, India

RISHIKESH BHARTI
Associate Professor
Earth System Science and Engineering Division
Department of Civil Engineering
Indian Institute of Technology Guwahati

ACKNOWLEDGEMENT

I take this opportunity to express my sincere thanks to many people who supported and helped me make this dissertation possible.

First and foremost, I express my sincere gratitude to my PhD supervisor, Dr. Rishikesh Bharti, Associate Professor, Department of Civil Engineering, IIT Guwahati, for his guidance, encouragement, and support in every aspect during my Ph.D. tenure at IIT Guwahati. I am extremely thankful to my doctoral committee members, Prof. Bimlesh Kumar, Prof. Rajan Choudhary, and Dr. Kanhaiya Pandey, for their guidance and valuable advice throughout this thesis work.

I would like to thank the Department of Civil Engineering and the Indian Institute of Technology Guwahati for all the necessary facilities provided during this thesis work. I would also like to sincerely thank all the data providers for the open-source datasets and the other secondary information collected from different authorities (DRDO), which helped successfully complete this work. I also thank the Ministry of Education, Government of India, for financial assistance during my PhD.

Finally, I would like to extend my heartfelt gratitude to my family—my beloved Maa, Papa Ji, Priya (Sister), Sunny (Brother), my wonderful wife Shreya Sharma, and my in-laws (Papa, Mummy, Soham Bhaiya, and Madhavi Bhabhi)—whose unwavering love and support have been the cornerstone of my journey. Their encouragement, understanding, and belief in my abilities have given me the strength to persevere through the highs and lows of my Ph.D. pursuit. Family is not just a pillar of support; they are the foundation upon which dreams are built and challenges are conquered. They provide the emotional resilience and motivation needed to face even the most daunting obstacles. I am equally grateful to my friends—Prakash Singh (Malik), Praveen Chakrawarti (Zakir Bhai), Tukaram Zore, Mahesh More, Ankit Kumar, Vatsal D. Patel, Pooja Ajay Gatagat, Sachin Raj, Lalit, Ronit, Priya Sejule, Ritu Anilkumar, and Hrik Chaudhary—who have stood by me as constant sources of encouragement and positivity. Additionally, I owe a deep sense of appreciation to my respected seniors— Dr. Lekshmi K., Dr. Sutapa Bhattacharjee, Dr. Chandan Pradhan, Dr. Sandeep Kumar Mondal, Dr. Ankit P Goswami, Nitish Bhaiya (RKMV), Dr. Samiran Mandal, Anup Subudhi, Dr. Himadri Bisaya, and Dr. Anshul Sisodia, —for their invaluable guidance and support during my time at IIT Guwahati. The collective contribution of my family, friends, and mentors has been instrumental in shaping my journey, and I will forever remain indebted to them for their presence and kindness.

MANMIT KUMAR SINGH

ABSTRACT

The sustainability of the eco-hydrology of the Indian Himalayas depends on snow and glacial dynamics. Glaciers, permanent and seasonal snow are the freshwater flow regimes and also act as an indicator of climate variability. The cryosphere also plays a pivotal role in managing the heat regimes, thus controlling the planet's radiation balance on a local, regional, and global scale. At the local level, snow cover influences different parameters of soil, such as hydraulic conductivity, moisture, and temperature of the soil strata; it also affects carbon sequestration and microbial colonization. On the other hand, snow coverage controls the discharge of snowmelt-fed perennial rivers, water availability, and groundwater recharge. Also, it governs the flora (type, density, and community structure), thus indirectly controlling the fauna at the regional scale. Therefore, it can be said that snow and its properties, such as albedo, depth, density, and thermal insulation, influence geological and biochemical processes.

The increasing natural and anthropogenic activities could cause climate change, affecting the frequency of the natural hazards in the Indian Himalayas. The glacial hazards in high mountain areas are frequent over the globe; recent disasters (Chamoli landslides, floods, forest fires, earthquakes, and landslides) in the Himalayas are evident, causing loss of human lives, infrastructural damage, and affecting day-to-day activities. The geophysical properties of snow/glaciers (SGP) are important indicators of the status of the snow/glaciers and related hazards. Important SGPs, such as dielectric constant, density, and liquid water content, play a vital role in avalanche studies, hydrological modeling, and flood monitoring. Conventional geophysical parameter studies require continuous in-situ measurements of snowfall and snowpack. Since in-situ measurements are challenging and expensive in such difficult terrains, satellite images have proved to be an important source of information for retrieving geophysical parameters. However, the high-altitude regions mostly have cloud cover, which motivates us to explore the potential of microwave remote sensing data in geophysical parameter studies. The study uses multispectral, synthetic aperture radar (SAR), and hyperspectral datasets in conjunction with in-situ measured parameters to develop models/estimate important SGPs, such as dielectric, density, wetness, grain size, snow depth, and snow impurities. Several field investigations were performed using field instruments (Snow Fork and Spectroradiometer) to measure the in-situ parameters and further integrated with the satellite-derived results to evaluate and improve the model performance.

A state-of-the-art inversion model has been developed using Sentinel-1 derived Stokes parameters to estimate snow dielectric and subsequently used to model density and wetness employing Looyenga's and Denoth's equations. The proposed inclusion of Stokes parameters in the inversion model has significantly improved the results. The respective modeled and in-situ snow dielectric, density, and wetness show a good coefficient of determination ($R^2 > 0.7$) with 95% confidence. Utilizing the field-measured values, the estimated root mean squared error (RMSE) of snow dielectric, density, and wetness is 0.26, 0.08 g/cm^3, and 0.84, respectively. The snow grain size estimation has been attempted using the PRISMA dataset. Analyzing reflectance spectra at specific wavelengths can infer snow grain size more accurately than multispectral sensors. This study presents the results from the Sikkim Himalayas and shows that a characteristic absorption position around 1.03μm is sensitive to snow grain size. Further, snow depth has been estimated using SAR interferometry (InSAR) techniques. A state-of-the-art methodology has been proposed for snow depth estimation in vegetated areas of Arunachal Pradesh, whose RMSE is less than 10 cm. This research also provides critical insight into studying snow conditions (non-contaminated and contaminated) using satellite remote sensing, which is not limited to visible regions of the electromagnetic spectrum. The methodology employs the harmonic use of Landsat-9 and Sentinel-1 datasets for the parts of Arunachal Pradesh, India. It is evident from the results that SAR backscattering is significantly affected by snow contamination due to changes in the snowpack's physical parameters.

This study presents three advanced inversion models and a novel methodology for estimating snow geophysical parameters (SGPs), employing synthetic aperture radar (SAR), multispectral, and hyperspectral datasets. The effectiveness of these models has been rigorously validated against in-situ measurements, demonstrating significant advantages of microwave remote sensing over optical sensors, particularly in overcoming cloud cover limitations, improving sensitivity to surface roughness, and enabling deeper penetration. These models enable accurate, continuous monitoring of SGPs, supporting critical applications in climate engineering, such as improved water resource management, disaster risk reduction, and permafrost stability prediction. Nonetheless, continued data collection and enhanced pre-processing are essential to strengthen the robustness of these models further. This research offers a foundational framework for analyzing the spatiotemporal dynamics of glaciers and permafrost through SGPs, aiming to guide sustainable adaptation strategies for the Indian Himalayan region and bolster climate resilience at regional and global scales.

Contents

List of Figures

List of Tables

Abbreviations

SAR	Synthetic Aperture Radar
InSAR	Interferometric Synthetic Aperture Radar
DInSAR	Differential Interferometric Synthetic Aperture Radar
SCM	Snow Cover Map
Pol-SAR	Polarimetry Synthetic Aperture Radar
MODIS	Moderate Resolution Imaging Spectroradiometer
SNAP	Sentinel Application Platform
GEE	Google Earth Engine
NDSI	Normalized Difference Snow Index
NDVI	Normalized Difference Vegetation Index
NDFSI	Normalized Difference Forest Snow Index
SCI	Snow Contamination Index
SGP	Snow Geophysical Properties/Parameters
MSL	Mean Sea Level
SLL	South Lhonak Lake
GLOFs	Glacial Lake Outburst Floods
NIR	Near-Infrared
PRISMA	PRecursore IperSpettrale dells Missione Applicativa, or Hyperspectral Precursor of the Application Mission
MAE	Mean Absolute Error
RMSE	Root Mean Squared Error
SWE	Snow Water Equivalent
LWC	Liquid Water Content
W	Snow Wetness
EMR	Electromagnetic Radiation
SWIR	Shortwave Infrared
ASTER	Advanced Spaceborne Thermal Emission Reflection Radiometer
ENVI	Environment for Visualizing Images
USGS	United States Geological Survey
ESA	European Space Agency
ASI	Agenzia Spaziale Italiana
TOA	Top of the Atmospheric Correction
BOA	Bottom of the Atmospheric Correction
DN	Digital Number
DOS	Dark Object Subtraction
FLAASH	Fast Line-of-Sight Atmospheric Analysis of Spectral Hypercubes
SIAC	Sensor Invariant Atmospheric Correction
IW	Interferometric Wide Swath
SLC	Single Look Complex
dB	Decibels

SID	Spectral Information Divergence
SAM	Spectral Angle Mapper
JHU	Johns Hopkins University
HMI	Himalayan Mountaineering Institute
RGP	Rathong Glacier Path
FIPPI	Fast Iterative Pixel Purity Index
LST	Land Surface Temperature
DRDO	Defence Research and Development Organization
SRTM	The Shuttle Radar Topography Mission
ESD	Enhanced Spectral Diversity
LIA	Local Incidence Angle

1

INTRODUCTION

The Himalayas offer one of the most extensive snow and ice resources outside the polar regions. Snow and glacier meltwater from the Himalayan region keep the major Indian river systems flowing year-round (such as the Indus, Ganga, and Brahmaputra). The physical properties of the Himalayan snow and glaciers require monitoring due to their hydrological importance and the associated natural hazards. Several regional disasters have been caused by debris flow, mass wasting, avalanches, and the bursting of high-altitude lakes that overflow downstream. Thus, it is important to continuously monitor the accumulated snow conditions in the complex terrain of the Himalayas. The snow condition is mainly characterized by its physical parameters. This thesis aims to work on comprehending the estimation of snow geophysical parameters through satellite remote sensing datasets, field investigation, numerical modeling, and cloud computing techniques.

1.1. Motivation

The area of the Indian Himalayas (which ranges from west to east) has a vast amount of snow-covered area with varying levels of glaciation, providing freshwater reservoirs (Singh et al., 2006). The Eastern Indian Himalayan region has continuous snow precipitation patterns in the higher altitudes from February through the end of May, in contrast to the Western Himalayas, where the extent of snow areas exhibits a falling tendency from March onwards (Kulkarni et al., 2010). The catchment area of this region is formed by the Himalayan snow-fed Teesta River and Brahmaputra River, which almost cut through from north to south. Notably, the depletion of the Sikkim snow cover (Rai and Mukherjee, 2021) is affecting the agriculture, hydropower, and tourism sectors and also resulting in the vulnerability of glacier lakes (Worni et al., 2013). Additional natural hazards, such as a snow avalanche that follows an ice avalanche trajectory around some glacier lakes with a moraine barrier, might cause floods in the downstream area as a result of lake outbursts (Worni et al., 2012; Vilimek et al., 2014; Carrivick and Tweed, 2016; Emmer et al., 2016; Dubey and Goyal, 2020). In 2023, we witnessed one of the largest and fastest-growing South Lhonak Lake (SLL) failures. The SLL is a moraine-dammed glacial lake in Sikkim's northern district (27˚54.741' N and 88˚11.857'E). Situated at an elevation of 5200 msl (mean sea level), the lake is east-west elongated and located in the tongue of the South Lhonak glacier. The date of October 4, 2023, marks a significant event in Sikkim, India.

Investigation reports reveal a severe outburst of flood triggered by the breach of the moraine dam embankment around SLL. This wreaked havoc in the Northeastern state, causing substantial damage and loss, especially downstream along the Lachen and Chungthang regions.

Snow Geophysical Parameters Estimation refers to the methodologies employed to measure and analyze critical characteristics of snow, including dielectric properties, density, wetness, grain size, depth, and contamination levels. These parameters are vital in hydrological modeling, water resource management, and climate change research, as they influence snowpack dynamics and water availability in ecosystems. Accurate estimating of these properties is essential for predicting snowmelt timing, assessing flood risks, and enhancing our understanding of snow's impact on regional and global hydrological cycles. Remote sensing techniques have emerged as powerful tools in estimating snow geophysical parameters, allowing for large-scale monitoring of snow conditions in challenging terrains. Instruments such as passive microwave sensors, satellite-based multispectral systems, and airborne imaging spectrometers provide valuable data that can be analyzed to derive insights into snowpack characteristics. Despite technological advancements, challenges remain due to complex topographical effects, variable snow conditions, and the need for regional calibration, which can affect the accuracy of remote sensing algorithms.

1.2. Need for the Study

Southeast Asia's freshwater tower, the Himalayan cryosphere, is regarded as the planet's third pole. Strong effects of persistent climate change are being seen in the related glaciated regions (Vohra, 2007; Bolch et al., 2008). In these areas, snow cover loss and glacier retreat have led to the rapid growth of numerous glacier lakes, most of which are blocked by unstable and unconsolidated materials (Richardson and Reynolds, 2000). Glacial Lake Outburst Floods (GLOFs) result from such dammed lakes failing. These devastating flash floods destroy infrastructure and human life in downstream areas. The Himalayan regions are seeing a decline in their ability to thrive due to anthropogenic activities and population growth. These regions are particularly vulnerable to severe devastation in the event of GLOFs. (Cherry et al., 2017). There are a few examples of such events in recent decades, such as one related to South Lhonak Lake, Sikkim, India, which occurred on 4th October 2023, and another disaster associated with Shisper Lake, in the Karakoram range of the Himalaya, which drained twice within one year (Khan et al., 2021). Such comprehending variations in Himalayan snow cover extent, glacier retreat, GLOFs, and freshwater supply require need-of-the-hour attention to be monitored continuously. One of the ways to forecast and safeguard from these low-frequency hazards is to study the variation of snow geophysical parameters over the region.

1.3. Aim and Objective of the Thesis

The main aim of this study is to explore the potential of optical and microwave remote sensing in studying the geophysical properties of snow in the Northeastern Indian Himalayas.

Objectives:

1) Inversion Modeling for Snow Grain Size Estimation.
2) To develop a model to estimate snow's dielectric, density, and wetness.
3) To estimate the snow depth.
4) To develop a state-of-the-art methodology to study the snow quality regarding contamination.

1.4. Thesis Structure

This thesis presents its findings in seven chapters. It focuses on comprehending the models and methods employed to estimate snow geophysical parameters, integrating state-of-the-art empirical equations, field research, and datasets from satellite remote sensing. Chapters of the thesis are organized based on the objectives of the present study. The chapter-wise summary of the thesis is given as follows:

- Chapter 1 describes the brief introduction, motivation, aim, objectives, and thesis structure.
- Chapter 2 reports a detailed literature review and conceptualizes the various methods applicable for snow geophysical parameters estimation through a wide range of satellite remote sensing datasets and other ancillary datasets.
- Chapter 3 deals with snow grain size estimation using Hyperspectral remote sensing datasets.
- Chapter 4 deals with snow wetness, dielectric, and density estimation using Multispectral, Hyperspectral, and Microwave remote sensing.
- Chapter 5 shows snow depth estimation using Microwave remote sensing.
- Chapter 6 deals with snow condition monitoring in terms of clear and contaminated using microwave remote sensing in conjunction with the multispectral dataset.
- Chapter 7 summarizes the present research and suggests the future scope of the current work.

2

LITERATURE REVIEW

Snow is a solid precipitation characterized by ice crystals that form in the atmosphere and accumulate on the ground. The definition of snow is usually restricted to the material composed of air and ice that has not changed much since it fell on the ground (Cuffey and Paterson, 2010). This study focuses on accumulated snow under continuous transformation due to Earth's physics. Such snow is a compacted layer incorporating fresh and older snow. The accumulated snow has experienced various physical transformations, such as melting, refreezing, and compression. It becomes denser and more cohesive with time as it compacts under its weight and undergoes a repetitive melt and refreeze cycle by phenomena known as snow metamorphism (Colbeck, 1982). This phenomenon is widely studied by monitoring changes in snow cover properties in response to changing weather and loading conditions (Brun et al., 1989; Lehning et al., 1998). Monitoring snowpacks for scientific and practical applications requires measuring various snow properties, including their spatial and temporal variations (Meier, 1975). Conventional methods offer detailed data at localized scales. However, remote sensing techniques provide significant potential for observing changes in snow properties across diverse spatial scales, ranging from research sites to global extents. Snow Geophysical Parameters Estimation refers to the methodologies employed to measure and analyze critical characteristics of snow, including dielectric properties, density, wetness, grain size, depth, and contamination levels.

2.1. Snow Geophysical Parameters and Their Importance

Based on past studies, snow cover has the following properties: (1) optical properties (Warren, 1982, 2019), (2) electrical properties (Glen and Paren, 1975), (3) mechanical properties (Salm, 1982; Petrovic, 2003), (4) thermal properties (Yen, 1981). According to Mellor, M. (1977), engineering properties from applied research on snow cover could enhance attempts to disseminate information about snow conditions. Policymakers and research managers should be interested in it, and economics should also benefit from it. This thesis discusses the macroscopic properties of snow, which are suitable for direct application to practical work. These snow characteristics do not include essential physical attributes known as small-scale structures (atomic, single crystal). The properties of snow selected for monitoring snow conditions are (1) snow grain size, (2) density, (3) permittivity, (4) wetness, (5) depth, and (6) contamination. Earth's physics continuously changes these properties, referred to as snow geophysical parameters/properties (SGPs) in this study.

2.1.1. Snow Grain Size

Snow grain size can be characterized through various methods suited to specific applications. Traditional techniques, such as measuring the largest dimension of a snow grain, measured in millimeters, and are often assessed using a crystal card and hand lens for in-situ measurements (Fierz et al., 2009), offer simple observational data. In contrast, advanced metrics like specific surface area (SSA) and effective grain radius (r_e) provide deeper insights into the optical and physical properties of snow (Grenfell and Warren, 1999; Nolin, 2010). These parameters are crucial for accurately modeling snow scattering, absorption, and reflectance, contributing to a more comprehensive understanding of snowpack dynamics (Donahue et al., 2021). The characteristic decline in near-infrared (NIR) reflectance of snow due to increased ice absorptivity provides a robust basis for estimating effective grain radius (r_e) (Nolin and Dozier, 2000). This relationship, affected by snow metamorphism and grain coarsening, has enabled the development of retrieval methods using NIR reflectance data (Fair et al., 2022). These methods include discrete measurements and mapping techniques, which vary based on the spectral range and resolution of the instruments utilized.

Characterizing snow grain size can be performed using both ground-based and remote-sensing methods. The local-scale methods for retrieving snow grain size (r_e) have advanced significantly, leveraging field spectrometers, specialized instruments, and NIR photography (Painter et al., 2007; Matzl and Schneebeli, 2006; Gallet et al., 2009; Zuanon, 2013; Gergely et al., 2013). While discrete measurement techniques provide detailed vertical or sample-specific profiles, they are time-intensive and limited in spatial coverage. Mapping methods, such as digital NIR photography, offer higher spatial resolution but are constrained by empirical calibrations and illumination sensitivity. Despite these advancements, a comprehensive method combining high spatial and spectral resolution for local-scale mapping of r_e remains unavailable (Donahue et al., 2021). Thus, remote sensing has emerged as a powerful tool for mapping r_e on a pixel-wise basis. Spaceborne multispectral sensors like the Moderate Resolution Imaging Spectroradiometer (MODIS) can estimate r_e using band ratios or spectral unmixing techniques (Donahue et al., 2021). Furthermore, space-borne imaging spectroscopy advancement has provided the Hyperion and PRISMA (PRecursore IperSpettrale dells Missione Applicativa, or Hyperspectral Precursor of the Application Mission) dataset for effectively estimating r_e (Negi et al., 2011; Singh et al., 2022).

Snow grain size is a fundamental property of snow cover directly related to its surface area (Donahue et al., 2021). Its estimation is essential for understanding and monitoring the Earth's radiation balance, particularly within the cryosphere (Jin et al., 2008). Snow grain size influences snow reflectance (Wiscombe and Warren, 1980; Marshall and Oglesby, 1994; Gelman et al., 2020) and plays a key role in characterizing snow metamorphism and stratigraphy (Colbeck, 1991). Surface snow grain size is critical for modeling snow albedo, a significant factor in the snow energy balance and snowmelt timing (Marks and Dozier, 1992). Additionally, the vertical distribution of snow grain size, or stratigraphy, is vital for microwave radiative transfer modeling (Brucker et al., 2011) and for understanding the mechanical (Pielmeier and Schneebeli, 2003) and thermodynamic (Hammonds et al., 2015) properties of snowpacks. Snowpack stability has frequently been examined in snow avalanches utilizing information derived from snow grain size and snow shape (Schweizer et al., 2003).

2.1.2. Snow Density

Snow density is a critical geophysical property of snow and a reliable climate change indicator (Armstrong and Brun, 2010). Snow density represents the mass of snow per unit volume, commonly measured in kilograms per cubic meter (kg/m^3). It exhibits substantial variability depending on the type of snow and prevailing environmental conditions. For example, snow density increases progressively from freshly fallen snow (50–70 kg/m^3) to firn (400 to 830 kg/m^3) and ultimately to fully compacted glacial ice (830–923 kg/m^3) (Cuffey and Paterson, 2010). Field measurement of snow density provides reliable localized data but is labour-intensive and influenced by snow stratigraphy and environmental conditions. However, remote sensing enables large-scale snow density estimation but is limited by spatial-temporal resolution and uncertainties from surface heterogeneity and environmental factors. Singh and Venkataraman (2009) demonstrate the potential of C-band dual-polarimetric SAR data from ENVISAT-ASAR for estimating dry snow density in rugged Himalayan terrain, with an algorithm achieving a mean absolute error of 21.3 kg/m^3 when compared to field measurements. Surendar et al. (2015) propose a novel methodology for snow density estimation using full-polarimetric SAR data, achieving high accuracy with a mean absolute error (MAE) of 0.027 g/cm^3 and a root mean squared error (RMSE) of 0.032 g/cm^3, validated against in-situ measurements.

In-situ snow density measurements are conducted using various methods, including core samplers, snow forks, snow pits, and micro-CT scanning, each providing valuable data on snow density and stratigraphy (Su et al., 2022). Snow Fork can provide a direct in-situ measurement of snow density. Before starting actual in-situ measurements, the snow fork is calibrated in the air, and the frequency 890.1 MHz (888 – 892 MHz), bandwidth 20.8 MHz (18–23), and attenuation 1799 (1600–3000) should fall within the prescribed ranges.

It significantly influences various snow characteristics, including mechanical properties (e.g., snow load estimation), thermal properties (e.g., thermal conductivity) (Zhang, 2005), optical properties (e.g., albedo) (Warren, 1982), and electromagnetic attributes (Tiuri et al., 1984). Furthermore, snow density is integral to snow hydrology assessments, particularly for estimating snow water equivalent (SWE) and predicting snowmelt runoff (Martinec and Rango, 1986; Sturm et al., 2010; McCreight and Small, 2014; Sturm, 2015). It is also a crucial parameter for retrieving SWE using remote sensing data, enhancing land surface models (Dutra et al., 2010), and forecasting snow-related disasters such as avalanches, spring floods, and droughts (Keshari et al., 2010). Accurate measurement of snow density is essential for understanding the physical properties of snow, as it affects both the microstructure and the overall behavior of snowpacks (Su et al., 2022). It influences snow layers' thermal, mechanical, and optical properties (Bormann et al., 2013). Therefore, it is also valuable for the assessments of snow trafficability (Lee and Wang, 2009), slope stability calculations for avalanche prediction (Brun et al., 1989), and snow hydrology (Rango and Martinec, 1995; Sturm et al., 2010). It varies with time and space, so it must be measured all over the accumulated snow rather than assumed to be a constant value.

2.1.3. Snow Permittivity

Snow permittivity is one of the important electrical properties of snow, which varies with electromagnetic frequencies (Evans, 1965). It is the only one with complex values among all other snow geophysical properties. The fundamental part is permittivity (relative permittivity/dielectric constant), defined as the ratio of snow and free space permittivity. The imaginary part is called dielectric loss, which typically depends on snow liquid water content and temperature. Snow is an insulator made of air, ice, and water content, which makes it a three-component system. Thus, the snow complex dielectric constant is measured as the dielectric mixture of ice particles, air, and liquid water content (Evans, 1965; Sihvola et al., 1985; Denoth, 1989). The dielectric properties of snow cover differ if the snowpack shows the same density because of the different structure of its ice networks (Yosida et al., 1958). Thus, it is sensitive to surface roughness. Denoth's (1994) study shows that in the frequency range of 10 MHz to 1 GHz, snow permittivity is primarily determined by its density and moisture content, with minimal influence from frequency. In contrast, ionic conductivity, ice grain size, and water phase distribution have negligible impacts on permittivity within this range. The dielectric and scattering characteristics of wet snow exhibit distinct behaviors across different regions of the electromagnetic spectrum. Snow demonstrates high visible spectrum reflectivity, strong thermal infrared absorptivity, and variable transparency at longer wavelengths. As snow transitions to a wet state, liquid water notably impacts its electrical properties, particularly at higher microwave spectrum (Meier,1975). These diverse electromagnetic properties form a robust foundation for remote sensing techniques to monitor snow. However, spatial resolution limitations, especially in mountainous terrains, continue to pose challenges for accurate observation (Koike and Suhama, 1993).

Various in-situ instruments are employed to measure the dielectric properties of snow, each suited to specific applications. Time Domain Reflectometry (TDR) measures the travel time of electromagnetic waves through the snow (Schneebeli et al., 1998; He et al., 2021), while Snow Forks enable direct field measurements of permittivity (Bradford et al., 2009). Capacitance and impedance probes assess the electromagnetic response of the snowpack, and portable microwave radiometers facilitate high-frequency dielectric measurements (Avanzi et al., 2014; Reistad, 2018). Collectively, these tools provide comprehensive methods for characterizing the dielectric behavior of snow under varying conditions.

Meier (1975) highlights the significance of snow dielectric properties in understanding snow dynamics and their application in estimating snow water equivalent (SWE), snow depth, and other snowpack characteristics. Evans (1965) examines how the permittivity and loss tangent of ice and snow change across different frequencies, highlighting the influence of snow density, impurities, and temperature and their relevance to glaciological field studies. Glen and Paren (1975) have shown that the dielectric properties of snow and ice are critical for differentiating between temperate and polar glacial ice. These properties reflect how ice responds to an applied electric field, which is influenced by factors like temperature, impurity content, porosity, and the presence of air bubbles. Snow dielectric significantly contributes to snow sintering (Mellor, 1977) (a specialized technique that compacts snow into a cohesive solid by applying heat and pressure without inducing melting). This method is crucial for improving snow's mechanical properties and density, making it highly applicable in polar construction and infrastructure development (Hong et al., 2022; Xiao et al., 2024).

2.1.4. Snow Wetness/Liquid Water Content (LWC)

Snow wetness, the liquid water content within the snowpack, plays a critical role in the hydrological cycle and is essential for water resource management (Awasthi and Varade, 2021). The measurement of snow wetness provides insights into the temporal and spatial variability of snow properties, which are crucial for understanding snowmelt dynamics and their implications for downstream water availability (Meier,1975). Snow-containing liquid water can be categorized into two regimes with distinct physical characteristics (Colbeck, 1982; Parmentier, 2024): (1) the **pendular regime**, where isolated water bodies occupy the pore spaces at low wetness, and (2) the **funicular regime**, where increased wetness causes water droplets to connect and form continuous liquid pathways within the pore structure. The transition between these regimes occurs at approximately 10–15% saturation of the pore volume, as noted by Denoth (1980, 2003). In field practice, snow is classified based on its volumetric water content or wetness (W). The classification includes **dry (W = 0), moist (W = 0–0.03), wet (W = 0.03–0.08), very wet (W = 0.08–0.15), and slush (W > 0.15)** (Green et al., 2004). Moist and wet snow typically falls within the pendular regime, while very wet snow and slush exceed the pendular-funicular threshold. Field classification is often qualitative, relying on indicators such as the snow's tendency to clump or the amount of water released underhand squeezing. However, large-scale LWC monitoring satellite missions like Sentinel-2 use multispectral data and algorithms that link spectral reflectance to snow liquid water content to estimate surface snow wetness (Varade and Dikshit, 2018). Further, multi-frequency and polarization SAR have been utilized to estimate snow density and wetness by analyzing backscattering coefficient simulations (Shi and Dozier, 2000; Tanikawa et al., 2002).

The hand wetness test is a globally used method by avalanche workers and snow observers to classify snow wetness, such as dry, moist, wet, very wet, or slush (Fierz et al., 2009). Advancements in technology, particularly computerized snow wetness meters or electronic devices such as the Snow Fork or the Denoth meter, have enhanced the assessment of snow wetness by allowing the recording of variations over time and at different depths within the snowpack (Denoth, 1994; Awasthi and Varade, 2021)

Bousbaa et al. (2022) highlight that the seasonal snowmelt is a critical water resource in mountainous regions, playing a key role in shaping the hydrology of downstream ecosystems. Mitterer and Schweizer (2013) highlight the significance of snow wetness for wet-snow avalanche prediction. Further, Madore et al. (2022) also identify LWC as a key factor for snowpack stability analysis, as well as for snowpack evolution (Marks et al., 1998; Essery et al., 2009; Kinar and Pomeroy, 2015)

2.1.5. Snow Depth

Snow depth is the measurement of the total snowpack depth over the ground. It also varies in time and space. According to Barnett et al. (2005), snow cover provides low heat conductivity and strong thermal resistance, which can lower land surface temperature and stabilize thermal conditions. Thus, snow depth can control the regional temperature and the growth of different flora and fauna. It is a key parameter in hydrology and climate research, as it directly correlates with SWE, representing the snowpack's water content (Awasthi and Varade, 2021). Accurate snow depth measurement is critical for assessing seasonal water resource dynamics, as it significantly impacts runoff and water availability during warmer periods (Nolin, 2010). Estimating snow depth is essential for evaluating the impacts of climate change. Variations in snow cover and depth indicate shifting climatic patterns, including rising temperatures and changes in precipitation (Nasim et al., 2022; Dai and Che, 2022). Vegetation cover significantly impacts snow depth measurements and estimates (Taheri and Mohammadian, 2022). Wind exposure significantly affects snow depth by influencing its distribution. Wind-driven processes, such as redeposition, create spatial variability in snow cover (Yang et al., 2020).

Manual snow depth sampling is costly, time-intensive, and poses risks to field crews. Sampling snow depths in avalanche start zones and runout areas is particularly challenging, highlighting the need for remote-sensing technologies (Deems et al., 2013). Moreover, manual methods are constrained by limited spatial intervals, making it challenging to capture the natural variability of snow depth at slope or basin scales (Elder et al., 1991; Blöschl, 1999; Hiemstra et al., 2006). Recent advancements, such as GPS interferometry, have enabled snow depth measurements with an accuracy of 10 cm (Gutmann et al., 2012). While promising, these techniques are still limited in spatial coverage, similar to snow monitoring networks in the western USA. Snow depth estimation employs various methods that range from traditional manual techniques to advanced remote sensing technologies (Lenormand et al., 2002; Rees, 2005; Lei and Siqueira, 2015). SAR Polarimetry (Pol-SAR) and SAR interferometry (InSAR)-based access has proven to help estimate snow depth (Mahmoodzada et al., 2020). Lievens et al. (2019) used time series Sentinel-1 records to study the inconstancy of snow depth in the mountains of the Northern Hemisphere. Repeat-pass interferometric datasets and approaches entrenched in InSAR have been extensively employed for the calculation of snow water equivalent and the analysis of snowpack dynamics (Evans and Kruse, 2014; Lei and Siqueira, 2015; Leinss et al., 2015; Li et al., 2017; Varade et al., 2020). Thus, snow depth estimation is vital for advancing climate studies and supporting disaster management strategies. Accurate snow depth measurement and monitoring are essential to climate change-altering precipitation patterns and snow dynamics. These efforts are critical for effective water resource management and reducing risks associated with snowmelt and related natural hazards (Meehan et al., 2023; Harder et al., 2016).

2.1.6. Snow Impurity

Snow is considered contaminated when any foreign materials are deposited/mixed with it. Clear snow comprises ice, water, and air and has no inclusions/impurities. Snow is considered contaminated when foreign objects (ash, coal, wood, etc.) are deposited/mixed with it. Several studies (Nazarenko et al., 2016; Xu et al., 2009; Ramanathan and Carmichael, 2008; Barnett et al., 2005; Hansen and Nazarenko, 2004) have examined the impacts of snow contamination on the climate and humans. Snow contamination can accelerate melting and majorly impact the radiative balance of snow cover (Xu et al., 2009; Ramanathan and Carmichael, 2008; Hansen and Nazarenko, 2004). According to Hansen and Nazarenko (2004), understanding the connection between the cryosphere, the atmosphere, and climate depends on how a snow impurity affects snow albedo reduction. Further, the deposition of black carbon accelerates the melting of snow, resulting in a decrease in freshwater sources at the catchment level (Xu et al., 2009; Barnett et al., 2005). In addition to lowering snow albedo (Wiscombe and Warren, 1980,1981) and raising snow surface temperatures, snow contamination can have an impact on the water quality of rivers (Kirchner et al., 1993) that receive runoff during snowmelt (Balla and Garg, 2023). Snow contamination is widely studied through optical remote sensing using a normalizing difference index called the snow contamination index (SCI). This relies on the observation that the effect of snow contamination is most evident in the visible region (0.3 - 0.7 μm) and decreases with increasing wavelength (Warren and Wiscombe, 1980; Negi et al., 2006, 2010). In the visible region of the electromagnetic spectrum, the contaminated snow has lower reflectance than clear snow (Staenz and Haefner, 1981; Warren, 1982; Takeuchi, 2009; Casacchia et al., 2001). Based on spectroradiometer (Di Franco et al., 2022) readings, Negi et al. (2010) introduced the SCI, which uses blue and green wavelengths. They claimed that the SCI index decreases and remains harmful for contaminated snow. Snow contamination can be easily identified with hyperspectral or multispectral datasets. With climate change affecting weather patterns and pollution distribution, monitoring snow contamination is becoming increasingly essential. Effective tracking of this phenomenon is critical for predicting and mitigating potential health risks associated with contaminated snow (Tang et al., 2011).

2.2. Interaction of EMR with Snow

The electromagnetic properties of snow are fundamental to understanding its interaction with electromagnetic radiation and its behavior in the environment. Snow, composed primarily of air and ice, exhibits distinct electromagnetic characteristics depending on its state (dry or wet), significantly affecting its reflection, absorption, and emission of electromagnetic waves across various wavelengths. These differences are significant for remote sensing applications, enabling monitoring of snowpack conditions, evaluating hydrological impacts, and analyzing climate change effects.

2.2.1. Optical properties of snow

Snow exhibits a distinct reflectance profile in the visible and infrared spectrum compared to other materials. Its spectral signature is characterized by high reflectance in the visible spectrum and lower reflectance in the shortwave infrared (SWIR) region (Hall et al., 1995). Comparative analyses of spectral signatures, based on the Advanced Spaceborne Thermal Emission Reflection Radiometer (ASTER) spectral library (Baldridge et al., 2009), reveal that ice and water have considerably lower reflectance than snow. The high reflectivity in the visible spectrum, combined with strong absorption in the SWIR region around 1.5 µm and 2.0 µm, forms the basis for snow identification using the Normalized Difference Snow Index (NDSI) (Hall et al., 1995). The NDSI is the ratio of the difference to the sum of reflectance in the green and SWIR bands. While clouds also demonstrate high reflectance in the visible spectrum, they differ from snow by exhibiting relatively higher reflectance in the SWIR region, enabling differentiation. An exception to this is thin cirrus clouds, which display similar spectral responses to snow across the visible and infrared spectrum (Bian et al., 2016).

Freshly fallen snow consists of fine-grained particles of ice and air, characterized by a low density and powdery texture. Over time, atmospheric processes cause these particles to adhere to one another, increasing grain size and density (Meløysund et al., 2007). This transformation is often influenced by the presence of LWC within the snowpack (Colbeck, 1982). As a result, the spectral reflectance of snow decreases across the visible and infrared spectrum. Ice and water are strong light absorbers, significantly reducing incident energy across all wavelengths in these spectral regions. This distinction facilitates the differentiation of snow from ice and water (Shekhar et al., 2019).

Furthermore, snow grain size can be characterized using indices such as the Snow Grain Index (Chang et al., 1976), which relies on visible and NIR spectral reflectance. Dozier (1989) developed four indices based on Landsat Thematic Mapper band reflectance to derive qualitative insights into snow contamination and grain size. A normalized difference index utilizing blue and green wavelengths was proposed to differentiate contaminated from uncontaminated snow, while the other three indices employed combinations of blue, NIR, and SWIR reflectance. However, these latter indices do not account for grain size variations independent of contamination and are more generalized in nature.

Additionally, these indices do not apply to refrozen snow. Refrozen and wet snow exhibit similar grain sizes and reflectance, except in the 0.98–1.3 μm region, where the absorption coefficient transitions between water and ice (Dozier et al., 2009). Therefore, accurate spatiotemporal monitoring of wet or refrozen snow requires hyperspectral data covering the 0.98–1.3 μm infrared region for improved precision.

2.2.2. Microwave interaction with snowpack

The dielectric properties of a snowpack at a specific microwave frequency are determined by the relative proportions of liquid water and ice within it (Ulaby et al., 1977). The presence of liquid water significantly contributes to the absorption of microwaves in the snowpack. Its absorption within a snowpack increases with rising temperature and decreases with higher frequencies. Increased absorption leads to a reduction in the penetration depth of microwaves in the snowpack. For instance, the penetration depth for a 20 GHz microwave signal is approximately 1 meter (Derksen et al., 2003; Tsang et al., 2008). The penetration of an incident electromagnetic (EM) wave in the snowpack is governed by the extinction coefficient, which is the sum of the volume absorption coefficient and the volume scattering coefficient (Montpetit et al., 2013; Maslanka et al., 2019; Saberi et al., 2020). The imaginary component of the snowpack dielectric constant regulates the volume absorption coefficient. In contrast, the scattering coefficient is influenced by the geometry and inhomogeneities of the snowpack relative to the wavelength of the incident wave (Leinß and Hajnsek, 2012).

The primary microwave frequency bands utilized for snow studies include the Ku-band (~17.25 GHz), X-band (~9.65 GHz), and C-band (~5.52 GHz). Each band exhibits distinct backscatter characteristics influenced by snow structure and composition. For example, the Ku-band is highly sensitive to snow grain size and structural properties. In contrast, the X-band demonstrates significant backscatter variability due to snow thickness and surface roughness (Achammer and Denoth, 1994; Nandan et al., 2017). The C-band is characterized by strong reflective properties while demonstrating lower sensitivity to microstructural variations relative to other frequency bands (Brangers et al., 2024; Hoppinen et al., 2024).

The backscatter from a snowpack is influenced by various snow-layer properties, particularly the quasi-horizontal stratification within the snowpack. Variations in snow properties, such as density and dielectric constant, are typically observed across different stratigraphic layers (Strozzi et al., 1997; Mätzler et al., 1997; Nagler et al., 2016). These stratigraphic variations significantly impact the backscattering characteristics of the snowpack. However, for wet snow, the effect of stratigraphy on backscatter is minimal due to the reduced penetration depth of the electromagnetic (EM) wave (Nagler, 1996; Singh and Venkataraman, 2010). Backscattering from a snowpack is generally modeled as a two-layer problem involving the air-snow interface and the snowpack volume (Chang et al., 1996). An EM wave incident on the snowpack surface is partially reflected and transmitted into the snowpack volume. The transmitted wave undergoes attenuation within the snowpack due to absorption and scattering losses in the medium (Nagler, 1996; Nagler and Rott, 2000).

The total backscattering from a snowpack consists of contributions from the air–snow interface, the snowpack volume, and the snow–ground interface (Shi et al., 2016; Singh et al., 2017). Each component's relative scattering power depends on the snowpack's state and thickness. Surface scattering is influenced by surface roughness, which is generally low, as snow surfaces are often considered smooth, except in Sastrugi or disturbed snow (Leroux and Fily, 1998; Zhuravleva and Kokhanovsky, 2011). Surface roughness properties are characterized by statistical parameters such as surface correlation length, standard deviation of surface height variations, and the shape of the correlation function (Ulaby et al., 1981,2014).

Attenuation of microwaves in the snowpack is determined by scattering coefficients, which depend on snow particle size and the wavelength of the incident wave, and absorption coefficients, which are influenced by the dielectric constant of the snowpack and its LWC (Nagler, 1996; Tiuri et al., 1984; Kokhanovsky and Zege, 2004; Grody, 2008). The SAR backscatter exhibits significant variation between wet and dry snow due to differences in dielectric properties and penetration depths (Hallikainen, 1992). Snowpack with a temperature above 0 °C is typically classified as wet snow. In contrast, snowpack with temperatures below 0 °C and a LWC of less than 1% by volume is considered dry snow (Stiles et al., 1981; Ulaby et al., 1982; Thakur et al., 2016). In dry snow, the primary contribution to backscatter arises from volume scattering within the snowpack and scattering at the snow/ground interface. As dry snow ages, surface scattering at the air-snow interface increases due to the growth of snow grain size caused by the melting and refreezing of the top snow layer (Shi and Dozier, 1995; Yueh et al., 2009; Varade et al., 2020a). In contrast, the backscatter from wet snow is dominated by a more substantial surface component, with a weaker volume component and typically no contribution from the snow-ground interface (Thakur et al., 2012). For a given snowpack thickness, the backscatter from dry snow is generally higher than that from wet snow (Shi and Dozier, 1995; Nagler and Rott, 2000; Thakur et al., 2013; Awasthi et al., 2020).

The backscatter response of a snowpack is generally influenced by several factors, including radar wavelength, wave polarization, incidence angle, local incidence angle, surface roughness, and dielectric properties (Baghdadi and Zribi, 2006; Fung and Chen, 2010; Ulaby et al., 2014). Radar waves with shorter wavelengths exhibit higher backscatter compared to longer wavelengths. Long-range radar wavelengths render the snowpack nearly transparent for dry snow, with grain sizes ranging from 0.1 to 0.3 mm. This transparency indicates that the radar wave propagates through the snowpack with minimal scattering or reflection from snow particles. In shallow, dry snow covers with a SWE of less than 20 cm at the C-band (5.3 GHz, 5.6 cm), volume scattering is negligible as the snow is a transparent medium for microwaves at these wavelengths (Bernier, 1987). For wet snow, the increased compactness of the snowpack results in a larger effective snow-grain size and greater snowpack thickness, significantly influencing the backscatter characteristics (Riche et al., 2013; Leinss et al., 2016).

Changes influence temporal variations in the dielectric properties of the snowpack with temperature. An increase in snowpack wetness elevates its dielectric constant, which reduces the penetration of microwave energy into the snowpack volume. Consequently, the snowpack loses its transparency to microwaves, even at longer wavelengths. Under these conditions, the dominant backscatter contributions arise from the air-snow interface and the snowpack volume (Nagler, 1996). Additionally, the effective surface roughness and the propagation path of electromagnetic waves increase at lower incidence angles, leading to reduced backscatter. Electromagnetic waves at low incidence angles also encounter more pronounced layover and shadowing effects. For this reason, microwave datasets acquired at higher incidence angles are preferred for snow-related studies in high-altitude mountain regions (Thakur et al., 2012).

2.3. Remote Sensing for Snow Geophysical Parameters

Remote sensing has revolutionized the study of SGPs by enabling extensive, continuous, and accurate monitoring of snow-covered areas. Traditional in situ methods, although precise, are constrained by their labour-intensive nature and limited spatial coverage, particularly in remote or high-altitude regions. Introducing satellite-based remote sensing technologies, including optical, thermal, and radar sensors, has addressed these limitations by offering consistent and high-resolution observations across varied spatial and temporal scales. The SAR and multispectral or hyperspectral imaging facilitate estimating SGPs by analyzing electromagnetic wave interactions with snowpacks. These advancements significantly enhance modeling and forecasting efforts related to hydrology, climate change, avalanche risk, and ecosystem dynamics, highlighting the critical role of remote sensing in cryospheric studies.

The pre-processing of satellite imagery, including Multispectral, Hyperspectral, and SAR datasets, is vital in remote sensing workflows to improve data quality and usability for diverse applications. This stage mitigates distortions and artifacts arising from atmospheric effects, sensor inconsistencies, and geometric misalignments, facilitating precise land use analyses, environmental monitoring, and disaster management. Key pre-processing techniques, including atmospheric correction, geometric correction, radiometric calibration, and image registration, are essential for ensuring the reliability and accuracy of information extracted from these imaging systems. Multispectral and hyperspectral imagery provide detailed spectral insights for accurate material identification and vegetation health assessment, whereas SAR imagery offers reliable, all-weather, and day-and-night monitoring capabilities. With advancements in satellite technology, the demand for sophisticated pre-processing techniques is increasing, underscoring the necessity for ongoing innovation in this area. The pre-processing of satellite imagery faces significant challenges, including mitigating various noise types and the complexities associated with diverse data formats requiring distinct calibration and processing approaches. Moreover, evaluating the performance of pre-processing methods is an intricate, demanding method selection tailored to specific application needs. Key software platforms, including the Sentinel Application Platform (SNAP), ENVI, MATLAB, Google Earth Engine, ArcGIS, etc, play a critical role in enabling efficient data processing and analysis, facilitating the handling of large datasets. The ongoing development of these tools, in conjunction with interdisciplinary collaboration, is fostering the creation of innovative solutions to address the complex challenges of satellite image pre-processing, thereby advancing applications in environmental monitoring, disaster management, and other fields. However, nowadays, satellite data providers (such as USGS, ESA, ASI, etc.) perform geometric correction, radiometric correction, image registration, and atmospheric corrections and directly provide application-ready datasets.

Satellite imagery can be classified according to the spectral range captured, the sensor types employed, and their specific applications. The primary categories of satellite images used in this thesis are Optical (Multispectral and Hyperspectral) and SAR images.

2.3.1. Multispectral and Hyperspectral Remote Sensing

Multispectral images are acquired using sensors that capture data across multiple spectral bands, from visible light to near-infrared and thermal radiation. These images are instrumental in snow cover mapping, glacial lake identification, glacier surface classification, vegetation monitoring, land cover classification, and landscape archaeology applications. A prominent example of a multispectral satellite is the ESA's Sentinel-2, which delivers high-resolution imagery across 13 spectral bands and generates atmospherically corrected surface reflectance products.

Hyperspectral images capture contiguous spectral bands with ~10nm of spectral resolution, while multispectral images provide discrete spectral bands with much coarser spectral resolution. This high spectral resolution enables more accurate identification and differentiation of materials, making it valuable for applications such as mineral exploration, environmental monitoring, snow contamination, and agricultural assessments. Analyzing detailed spectral signatures in hyperspectral data improves the detection of subtle changes in land cover and land use over time.

Atmospheric correction is an essential preprocessing step in satellite imagery analysis to mitigate the influence of atmospheric effects on sensor data. It aims to eliminate atmospheric influences from satellite or airborne remote sensing data, thereby enabling the retrieval of the actual surface reflectance or radiance. This process accounts for the scattering and absorption of electromagnetic radiation caused by atmospheric constituents, including gases, aerosols, and water vapor.

The key scientific steps involved in atmospheric corrections are as follows:

Radiative Transfer Modeling: The study of radiative transfer and its role in atmospheric correction has a well-established history, closely tied to advancements in remote sensing technology (Thomas and Stamnes, 2002). The interaction of sunlight with the atmosphere is represented through modeling that accounts for scattering mechanisms, including Rayleigh and Mie scattering, as well as absorption by atmospheric components such as water vapor, carbon dioxide (CO_2), and ozone (O_3). Radiative transfer equations are employed to model light propagation through the atmosphere. Inspiring contributions, such as those by Clough et al.

(1981), who examined spectral transmittance, and Bohren (1987), who analyzed multiple scattering phenomena, underscored the intricate radiative processes influencing remote sensing observations.

Top-of-Atmosphere (TOA) Radiance/Reflectance: Top-of-Atmosphere (TOA) radiance represents the total electromagnetic radiation recorded by a satellite sensor at the Earth's atmospheric boundary. This measurement encompasses contributions from both the Earth's surface and atmospheric interactions, including scattering and absorption by gases, aerosols, and clouds. TOA reflectance is computed from TOA radiance by normalizing it against solar irradiance, sensor geometry, and observation conditions, thereby standardizing the data for further analysis. Atmospheric correction isolates the atmospheric components from the TOA signal to obtain the actual surface reflectance. BOA (Bottom-of-Atmosphere) reflectance accurately represents the Earth's surface reflectance, free from atmospheric interference. The conversion of TOA reflectance to BOA reflectance is crucial for various quantitative remote sensing applications.

Surface Reflectance Retrieval/BOA: Atmospheric correction algorithms estimate surface reflectance by eliminating the contributions from the following atmospheric components: (i) Downwelling irradiance- Scattered sunlight in the atmosphere before reaching the Earth's surface (ii) Upwelling radiance- Light scattered and reflected towards the sensor by the atmosphere (iii) Path radiance- Additional radiance is introduced into the signal due to scattering within the atmosphere.

Input Parameters: Precise atmospheric correction necessitates the following information- (i) Solar zenith angle: The angle between the Sun and the horizontal plane. (ii) Sensor viewing geometry: The angle between the sensor and the Earth's surface. (iii) Atmospheric conditions: Concentrations of gases (e.g., O_3, CO_2), aerosol optical thickness, and water vapor.

Further, several methods are available, each with distinct advantages and drawbacks. This section overviews some of the most widely used atmospheric correction algorithms.

Dark Object Subtraction (DOS) is a widely used, straightforward atmospheric correction method. It operates on the assumption that dark objects, which reflect minimal light, are present in the scene. The algorithm identifies the minimum Digital Number (DN) value in the image histogram and subtracts it from all pixel values to reduce the effects of atmospheric scattering. This approach benefits images moderately impacted by haze (Song et al., 2001).

Fast Line-of-Sight Atmospheric Analysis of Spectral Hypercubes (FLAASH) is a sophisticated atmospheric correction technique for hyperspectral imagery. It utilizes the MODTRAN radiative transfer model to incorporate atmospheric conditions and derive spectral reflectance from hyperspectral radiance data. As part of the Atmospheric Correction Module in various image processing software (such as ENVI), FLAASH is particularly valuable for applications that demand high spectral resolution and precision (Hernandez-Baquero, 2000).

Radiative Transfer Models, including 6S, LOWTRAN, and MODTRAN (Abreu and Anderson, 1996; Ignatov and Stowe, 2002; Anderson et al., 2007), provide advanced methods for atmospheric correction by simulating light propagation through the atmosphere, factoring in variables such as aerosol concentration and humidity. Although these models are effective, they necessitate scene-specific atmospheric data, which can be challenging to acquire, thus restricting their broader applicability in certain situations.

Sensor Invariant Atmospheric Correction (SIAC): Unlike traditional empirical approaches, SIAC (Yin et al., 2019) employs a data fusion method for atmospheric correction of satellite imagery, incorporating uncertainty information from multiple data sources. It leverages the high temporal resolution of MODIS observations to obtain a BRDF (*Bidirectional Reflectance Distribution Function*) description of the Earth's surface as prior information on surface properties. Additionally, it uses ECMWF CAMS Near-real-time data as prior information on atmospheric states to achieve optimal estimations of atmospheric parameters. The SIAC algorithm is implemented in Python and has been successfully tested with data from Sentinel-2, Landsat-8, Landsat-5, Sentinel-3, and MODIS, demonstrating its capability to correct atmospheric effects effectively.

Sen2Cor (Main-Knorn et al., 2017) is a processing tool for generating and formatting Sentinel-2 Level 2A products. It performs atmospheric, terrain, and cirrus corrections on Level 1C Top-of-Atmosphere (TOA) input data. The processor generates bottom-of-atmosphere (BOA) reflectance images, optionally corrected for terrain and cirrus effects. Additionally, it produces outputs such as Aerosol Optical Thickness, Water Vapor content, Scene Classification Maps, and Quality Indicators for cloud and snow probabilities. The output product maintains the Level 1C User Product format, consisting of JPEG 2000 images at three spatial resolutions: 60 m, 20 m, and 10 m.

2.3.2. Microwave Remote Sensing

Sentinel-1A is an active microwave imaging radar. Sentinel is a family of satellites built by the ESA to meet the needs of the EU Copernicus program. To date, Copernicus is the world's most extensive Earth observation program. Satellite-1 constellation is formed by two identical satellites- Sentinel-1A and Sentinel-1B: The same orbit, phased at 180° to each other. The constellation allows a repeat cycle of 6 days or 12 days over meditaranium, the North coast of Africa, and part of Antarctica. The satellite acquires data in imaging modes with swath and resolution given in Table 2.1.

Table 2.1: Sentinel-1 acquisition modes, products of mode, and Spatial resolution/Swath

Acquisition Modes	Products of Modes	Spatial Resolution/Swath
Strip map Mode (SM)	Level-0 Raw	5×5 m/ 80 km
Interferometric Wide Swath (IW)	Level-1 SLC	5×20 m/ 250 km
Extra-wide Swath	Level-1 GRD	25×100 m (5×20 m) / 400 km
Wave Mode	Level-2 OCN	20×20 m / 100 km

SAR data processing, exemplified by systems such as Sentinel-1, has become a pivotal advancement in remote sensing, offering high-resolution imaging of the Earth's surface regardless of weather conditions or lighting. SAR technology utilizes sophisticated computational methods to convert raw radar signals into meaningful information, supporting various applications, including environmental monitoring, urban development, disaster management, and agricultural analysis. A key advantage of SAR lies in its ability to penetrate cloud cover and operate effectively during nighttime, distinguishing it from optical imaging systems and underscoring its importance in continuous monitoring and surveillance. The processing of SAR data involves several systematic steps, including data preparation, preprocessing, and advanced analytical techniques. These processes are designed to enhance image quality and geolocation accuracy, ensuring the data can be effectively analyzed. The Sentinel Application Platform (SNAP) is a fundamental component of SAR data processing workflows, particularly for Sentinel-1, as it systematically enhances data quality and usability. Its advanced features, including batch processing and efficient memory management, facilitate effective handling of the large data volumes produced by SAR systems, establishing it as an essential tool in remote sensing applications.

The preprocessing workflow generally comprises a few critical steps to reduce error propagation and enhance data integrity.

Apply Orbit File (AOF): Accurate geolocation is critical for SAR data analysis. The AOF operator downloads updated metadata that enhances the precision of the initial downloaded orbit files. This step should be prioritized to ensure optimal results in subsequent processes

Speckle Filtering: Radar images often suffer from noise known as speckle, which can obscure relevant features. Speckle filtering techniques are employed early in the processing chain to enhance image quality and prevent speckles from affecting later operations such as terrain correction and decibel conversion. Various filtering methods are available, including Boxcar, Median, Frost, Gamma Map, Lee, and Refined Lee filters, with the latter being noted for its ability to preserve critical image details.

Terrain Correction: SAR images captured at varying angles may exhibit geometric distortions. Terrain correction methods, such as Range Doppler correction, are applied to align the image geometry with real-world coordinates. This step utilizes a digital elevation model (DEM) to accurately adjust the pixel locations in the image, thereby compensating for topographic effects like foreshortening and shadowing.

Calibration: This step converts digital pixel values into radiometrically calibrated backscatter values. The calibration process involves applying a constant offset and range-dependent gain to the image intensity values, allowing for a more accurate representation of the radar signal.

Conversion to Decibels: The pixel values are converted to a logarithmic scale, specifically decibels (dB), to improve visualization and analysis. This transformation stretches the radar backscatter values into a range approximating a Gaussian distribution, facilitating better data interpretability.

However, the preprocessing steps and techniques can vary considerably based on the specific goals and needs of the application. The variability comes from the wide range of fields where Synthetic Aperture Radar (SAR) data is used. These include environmental monitoring, agriculture, urban planning, disaster management, and climate studies. Each field requires specific processing methods to optimize the data for its analysis.

2.4. Inversion Models for Snow Geophysical Properties

Inversion models for snow geophysical properties are mathematical tools designed to interpret data on snow characteristics, including density, grain type, liquid water content, etc. These models are essential in environmental science, providing insights into snowpack dynamics. They also enhance understanding of hydrological processes, predicting avalanches, and assessing the impacts of global warming on snow and ice systems (Lehning et al., 2004; Rücker et al., 2019; Shea et al., 2021). Classical models focus on deterministic solutions based on the best fit to observed data, while advanced methods offer probabilistic insights, such as Bayesian models, which incorporate prior knowledge and uncertainty (Ismail-Zadeh et al., 2023; Wilder et al., 2024). Inversion models face challenges related to data quality, computational complexity, and the variability of snow properties influenced by environmental factors. Measurement errors and the dynamic nature of snow metamorphism further complicate accurate modeling.

Integrating data assimilation techniques and advanced remote sensing technologies is essential to improve the reliability of these models (Liu et al., 2022; Quéno et al., 2023). Overall, inversion models are fundamental for advancing the scientific understanding of snow geophysical properties. They play a critical role in meteorology, hydrology, and climate science (Durand et al., 1993; Krinner et al., 2018; Donahue et al., 2022). Ongoing advancements in these models are essential for addressing the challenges of changing climatic conditions and their impact on snowpack stability and hydrological processes.

The following table (Table 2.2) presents a summarized list of methods to streamline the complexity of various inversion models. These methods, referenced from existing literature, focus on estimating snow geophysical parameters using optical and microwave datasets.

Table 2.2: Techniques for characterizing snow cover using optical and microwave remote sensing methods.

Sl. No.	Methods	SCA/SGP, Sensor, resolution	Approach/Formulae	Remarks
01	Shi and Dozier (1997)	SCA, SIR-C/X-SAR, 30 m	Coherence and backscattering measurements	Investigation of interferometric coherence quantities
02	Shi, Hensley, and Dozier (2000)	SCA, SIR-C SAR, 30 m	Classification approaches for discriminating dry from wet snow	Integration of Digital Elevation Model (DEM) information for mapping seasonal snow
03	Nagler and Rott (2000)	Wet snow, ERS-1, 30 m	Investigating backscatter variation in multi-temporal SAR Datasets for mapping wet snow cover	The study examines the impact of varying look angles on the accuracy of wet snow mapping.
04	Singh et al. (2014).	SCA, ALOS-PALSAR-2, 6 m	Estimation of the snow-covered area utilizing scattering mechanism models	Evaluation of fully polarimetric L-band data for classifying snow-covered and snow-free areas.
05	Varade, Dikshit, and Manickam (2019)	Dry/wet snow, Sentinel-1 and Sentinel-2, 20 m	Building on the methodology proposed by Nagler et al. (2016) for wet snow mapping, dry snow is identified from the snow-covered area (SCA) using multispectral data.	A straightforward approach with challenges related to sensor synergy and limited applicability under cloud cover conditions.
06	Karbou et al. (2021).	Wet snow, Sentinel-1and Sentinel-2, 20 m	This study adopts the methodology of Nagler et al. (2016) to examine the impact of terrain parameters on snow distribution.	Investigations indicate discrepancies in snow cover estimations between Sentinel-1, which tends to underestimate, and Sentinel-2, particularly over forests and glaciers. For monitoring wet snow in the French Alps, ascending and descending Sentinel-1 passes provide complementary observations.
07	Varade and Dikshit, (2018)	Snow liquid water content, Sentinel-2, 20m	This study adopts NIR-NDSI feature space using B8A reflectance in the NIR spectrum.	A strong correlation was observed between the model estimates and the in-situ data, with a coefficient of determination of 0.94 and an error of 0.535.
08	Varade and Dikshit, (2018)	Snow liquid water content, density, and dielectric, Sentinel-2, 20m	This study adopts NIR-NDSI feature space using B8A reflectance in the NIR spectrum.	A strong agreement was found between the modeled and measured parameters under wet snow conditions, as indicated by coefficients of determination of 0.968, 0.521, and 0.969 for snow wetness, density, and fundamental part of permittivity, respectively.
09	Arslan et al. (1999)	SWE, Multifrequency polarimetric EMISAR data at C-band, 5m	The inversion of snow water equivalent at C-band VV polarization	The results demonstrate a positive correlation between the backscattering coefficient and snow water equivalent across all polarizations in the C-band.

Sl. No.	Methods	SCA/SGP, Sensor, resolution	Approach/Formulae	Remarks
10	Gulab Singh et al. (2017)	Snowpack density, fully polarimetric TerraSAR-X SAR datasets, 3m	The algorithm introduces a novel generalized hybrid decomposition model. The generalized volume scattering parameter derived from this model is utilized for the inversion-based estimation of snow density.	The mean absolute error, root mean square error, and index of agreement for snowpack density were 9.9 kg/m^3, 10 kg/m^3, and 0.96, respectively. These values fall within the acceptable range for accuracy.
11	Gulab Singh et al. (2006)	Snow wetness estimation using snow dielectric inversion, ENIVISAT-ASAR dual polarization (HH and VV) data, 10m	This study employs a Physical Optics Model (POM)-based inversion model for surface scattering. The POM-based inversion provides permittivity values, which can subsequently be used to estimate snow wetness.	Field measurements indicated that snow wetness estimates derived from ASAR data exhibited a correlation coefficient 0.8 at a 95% confidence interval. The observed snow wetness varied between 0% and 15% by volume.
12	Ravasio et al. (2024)	Snow wetness, PRISMA, 30m	This study developed a novel spectral index, the Snow Surface Wetness Index (SSWI), using the BioSNICAR radiative transfer model. The SSWI is calculated by determining the continuum-removed area of the absorption feature at 1030 nm and normalizing it to the absorption depth at 1025 nm.	A k-fold cross-validation analysis yielded a coefficient of determination of 0.7 and a Root Mean Square Error of 3%, highlighting the effectiveness of the proposed index in retrieving liquid water content (LWC) from field measurements and mapping LWC using PRISMA data.
13	Negi et al. (2011)	Snow albedo and effective snow grain size, ASD spectroradiometer in the spectral wavelength range of 350nm–2500nm with 3nm spectral resolution in VIR and 10nm spectral resolution at SWIR region	Snow grain sizes were retrieved using various models based on the ART theory. The two-channel model, utilizing one band in the visible region and another in the NIR region, demonstrated strong performance for Himalayan seasonal snow and showed consistency with temporal variations in grain size.	This method is highly effective for clean, dry snow, such as those in the upper Himalayan region. However, its application is limited in the lower and middle Himalayas, where older snow often exhibits low reflectance values (<20%) at the 1.24 µm wavelength, rendering the ART theory inapplicable.
14	Thakur et al. (2017)	Snow Dielectric, wetness, and density (RISAT)-1 C-band SAR data, Resources at 1/2, SRTM-X30 DEM, ASTER GDEM, MODIS and Landsat data	SAR-based inversion models were used to find wet and dry snow dielectric constant, dry and wet SCA, snow wetness, and snow density.	SAR-based inversion models were employed to estimate the dielectric constants of wet and dry snow, snow-covered area (SCA) for wet and dry conditions, snow wetness, and snow density.
15	Negi, Kulkarni, and Singh, (2006)	Snow contamination, ASD's (Analytical Spectral Devices, 1999) Field Pro FR Spectroradiometer.	The study revealed that increasing contamination reduces snow reflectance across all wavelengths, with the most significant decrease observed in the visible region. Furthermore, the reflectance peak shifts towards longer wavelengths as the level of contamination increases.	This study indicates that hyperspectral data can be utilized to estimate the proportion of snow within mixed pixels. The findings enhance existing Normalized Difference Snow Index (NDSI)-based algorithms for snow cover monitoring and facilitate the development of new algorithms when hyperspectral data is accessible.

Sl. No.	Methods	SCA/SGP, Sensor, resolution	Approach/Formulae	Remarks
16	Lievens et al., 2022	Snow depth, Sentinel-1 backscatter observations, European Alps	The snow depth retrieval algorithm assumes that increased signal depolarization and stronger cross-polarized scattering, influenced by snowpack characteristics and interactions, directly correlate with snow depth.	Sentinel-1 snow depth retrievals demonstrate strong correlations with regional model simulations and in situ measurements, especially under dry snow conditions at resolutions of 500 m and 1 km, with a Pearson correlation of 0.89 and mean absolute errors of 20%–30% for snow depths of 1.5–3 m, while higher uncertainties arise in wet, shallow, or forested regions.
17	Mantsis et al., 2020	Sentinel 1 image and Twitter data, Finland	This study demonstrates that integrating satellite backscatter measurements with social media data, particularly from platforms like Twitter, significantly enhances snow depth estimation accuracy by leveraging regression analysis to reduce bias and noise, with citizen-generated multimodal data acting as a critical component for model refinement.	Adding variables like social media indices and temperature or temporal factors into snow depth estimation models significantly enhances accuracy. Model 4 achieves the lowest MSE (47.11 and 54.98 cm) for both areas, demonstrating its superior predictive capability.
18	Feng et al., 2024	Snow Depth, Sentinel-1, PolSAR	this study was to develop a dual-polarimetric radar snow depth estimation (DpRSE) methodological framework that utilizes Sentinel-1 data for snow depth retrieval in the Scandinavian Mountains	The coefficient of determination (R^2) for the DpRSE method reached 0.66, representing a 26.9 % improvement over the cross-polarization ratio method. Moreover, the mean absolute error (MAE) decreased by 20 %. This study offers a novel SAR snow depth retrieval perspective utilizing polarization information.
19	Awasthi et al., 2021	Snow Depth, TerraSAR-X/TanDEM-X, PolInSAR	This study works on the development of a Polarimetric SAR Interferometry (PolInSAR) based modeling approach for snow-depth estimation using TerraSAR-X/TanDEM-X datasets acquired in the pursuit monostatic mode (temporal baseline = 10 seconds).	The estimated snow depth for both dates (21 January 2015 and 22 January 2015) shows a precise correlation with the ground datasets. The rise in model retrieved snow-depth value from 0.84 m to 1.24 m is observed during the period. The retrieved results were validated using the ground data of snow depth from the Automatic Weather Station (AWS) of Snow and Avalanche Study Establishment (SASE), Defence Research and Development Organization (DRDO), and Indian Institute of Remote Sensing (IIRS) installed in the Dhundi region of the study area for exact dates.

Sl. No.	Methods	SCA/SGP, Sensor, resolution	Approach/Formulae	Remarks
20	Varade et al., 2020	Snow Depth, Sentinel-1, DInSAR, 10m	This study demonstrates an improved approach for snow depth estimation in the Indian Himalayas using Sentinel-1 dual-polarimetric SAR data, where bias corrections for snow phase and residual errors significantly enhance accuracy, achieving a coefficient of determination of 0.628, with an ~0.4 improvement over conventional methods.	An improvement of above 0.4 in the R^2 coefficient and 1 cm in the RMSE was observed in the proposed snow depth estimates concerning those derived using the conventional method. It is worth mentioning that, with the availability of a higher quality DEM, an improvement in accuracy is possible.

2.5. Research Gaps

The key gaps and research opportunities in estimating snow geophysical parameters (SGPs), particularly in challenging regions like India's Eastern Himalayas. Here is an explanation of each point:

1. **Limited Research on Inversion Models for SGPs Estimation**:
    - SGPs such as density, dielectric constant, and wetness are crucial for understanding snowmelt dynamics and assessing hazards like avalanches and floods.
    - Despite their importance, minimal research has focused on developing inversion models tailored for SGP estimation in snowmelt-prone and hazard-prone regions.
    - This gap is particularly significant for regions like the Eastern Himalayas, where the challenging terrain and frequent climate-induced hazards demand advanced modeling tools.
2. **Need for Novel Inversion Models Using SAR Polarimetry and Interferometry**:
    - SAR polarimetry and SAR interferometry (InSAR) are promising techniques for retrieving SGPs, as they provide valuable information about snow and ice's physical and structural properties.
    - In cloud-prone, high-altitude regions, optical sensors face limitations due to poor visibility. SAR, which operates independently of cloud cover and daylight, can provide year-round data.
    - Developing novel inversion models that leverage SAR polarimetric and interferometric data is essential to estimate SGPs accurately and consistently in these regions.
3. **Study of Snow Impurity Using SAR**:
    - Snow contamination (e.g., by dust, soot, or pollutants) alters snow's physical and dielectric properties, impacting its reflectance and backscatter characteristics.
    - Sentinel-1 C-band SAR data, which operates in the microwave range of the electromagnetic spectrum, is particularly well-suited for snow studies, as it penetrates snow and ice layers better than visible or infrared sensors.
    - Further research is needed to understand how snow contamination affects SAR backscatter, enabling more accurate retrieval of SGPs under varying environmental conditions.

Addressing these research gaps through advanced SAR-based models and techniques will improve the understanding and monitoring of SGPs in the Eastern Himalayas. This will enhance the region's capacity for hazard prediction, water resource management, and climate resilience planning.

3

INVERSION MODELING FOR SNOW GRAIN SIZE

Snow grain size is a fundamental property of snow and is directly proportional to its surface area. The snowpack's stability has often been investigated in snow avalanches using data from the size and shape of the snow grains. The spatial and temporal change in the snow grain size can help characterize the snowpack's thermal state and estimate the temporal and spatial distribution of snowmelt. The grain size of snow becomes coarser with melting and shows lower spectral albedo.

This chapter presents a case study on developing an inversion model for snow grain size, focusing on the South Lhonak glacier region following a flash flood event on October 4, 2023. Snow grain size mapping was performed using recent PRISMA hyperspectral data acquired on October 8, 2023, by the Italian Space Agency. The mapping utilized the spectral information divergence method, with the Johns Hopkins University (JHU) spectral library for snow grain size as an input endmember. In the absence of in-situ measurements, the absorption band area method, which quantifies the energy absorbed by snow/ice particles, was employed to validate the mapped snow grain sizes.

3.1. Introduction

Estimating snow grain size is crucial for understanding and monitoring the Earth's radiation balance, particularly in the context of the cryosphere (Jin et al., 2008). The size of snow grains plays a key role in determining snow albedo, impacting the reflection of sunlight by the snow-covered surface (Marshall and Oglesby, 1994; Gelman Constantin et al., 2020). The snow grain size, which represents the course of snow metamorphism, has been identified as one of the most valuable snow physical parameters (Singh et al., 2022). Snowpack stability has frequently been examined in snow avalanches utilizing information derived from snow grain size and snow shape (Schweizer et al., 2003). Due to the rough topography of the Himalayas, many geophysical parameters are poorly sampled. As a result, developing sophisticated remote sensing techniques is critical for obtaining timely information on the spatiotemporal variability of snow cover and snow grain size (Awasthi and Varade, 2021). According to IAHS International Classification for Seasonal Snow on the Ground (Colbeck, 1985), the observer should select a homogenous snow mass and record the mean size of its predominant grains with a focus on measuring the diameter of the grain being its grain size (measured in millimeters). Although this approach might work well for field research, in the case of remote sensing-based research characterizing the average snow grain size over wide regions is necessary (Armstrong et al., 1993). Surface feature extraction and mapping based on spectral signatures are popular hyperspectral remote sensing applications (Varade et al., 2019). Snow surface features such as snow grain size, snow wetness, and snow albedo have all been studied using hyperspectral remote sensing (Dozier and Painter, 2004). The hyperspectral images and advancements in radiometric asymptotic models have led to the emergence of more precise snow grain size inversion models (Fair, 2021; Fair et al., 2022). Negi and Kokhanovsky (2011) used Hyperion sensor data to retrieve snow grain size and spectral albedo (planar and spherical albedo) for the western Himalayan snow cover. In contrast, Singh et al. (2022) employed PRISMA (PRecursore IperSpettrale dells Missione Applicativa, or Hyperspectral Precursor of the Application Mission) data. They used a semi-automatic way to estimate snow grain size, such as the Spectral Angle Mapper (SAM) classification, and the findings were compared with the snow grain size index method using a decision tree algorithm. Such inversion techniques depend on the absolute magnitude of the reflected radiance and, therefore, are sensitive to topography. Unlike SAM, spectral information divergence (SID) treats each pixel spectrum as a random variable. Then, it calculates the difference in probabilistic characteristics between two spectra. Spectral Angle Mapper (SAM) derives geometric information from two spectra (Chang, 1999). SID can be used to explain the statistics of a spectrum and is derived from the idea of divergence that appears in information theory. Nolin and Dozier (1993) show an inversion method for snow grain size called the absorption band area method, which is hardly affected by topographic error, solar illumination angle, and noise (Nolin and Dozier, 1993). The physical sense of this method is that the absorption feature is directly proportional to the amount of energy absorbed by the ice particles over that spectral region.

In this research, SID is used to map snow grain size, and then the absorption band area method is utilized to validate the trend of energy absorbed by each snow grain size. The grain size mapping method is applied to PRISMA data using the JHU snow spectral library. The South Lhonak glacial lake region is the study area due to the recent GLOF. October 4, 2023, marks a significant event in Sikkim. A severe flash flood generated by a fast and intense rainfall event over South Lhonak Lake in North Sikkim has wreaked havoc in the northeastern state, causing substantial damage and loss (Rawat, 2023). This study addresses the snow grain size mapping for the South Lhonak Glacier region following a major natural disaster, which is pertinent and timely. It highlights the advancements in remote sensing technologies for snow research using hyperspectral data from PRISMA level 2 (Bottom of the Atmosphere Reflectance). In the lack of in-situ data, this study sheds light on the possible use of snow grain size mapping to evaluate snowpack conditions and dangers.

3.2. Study Area

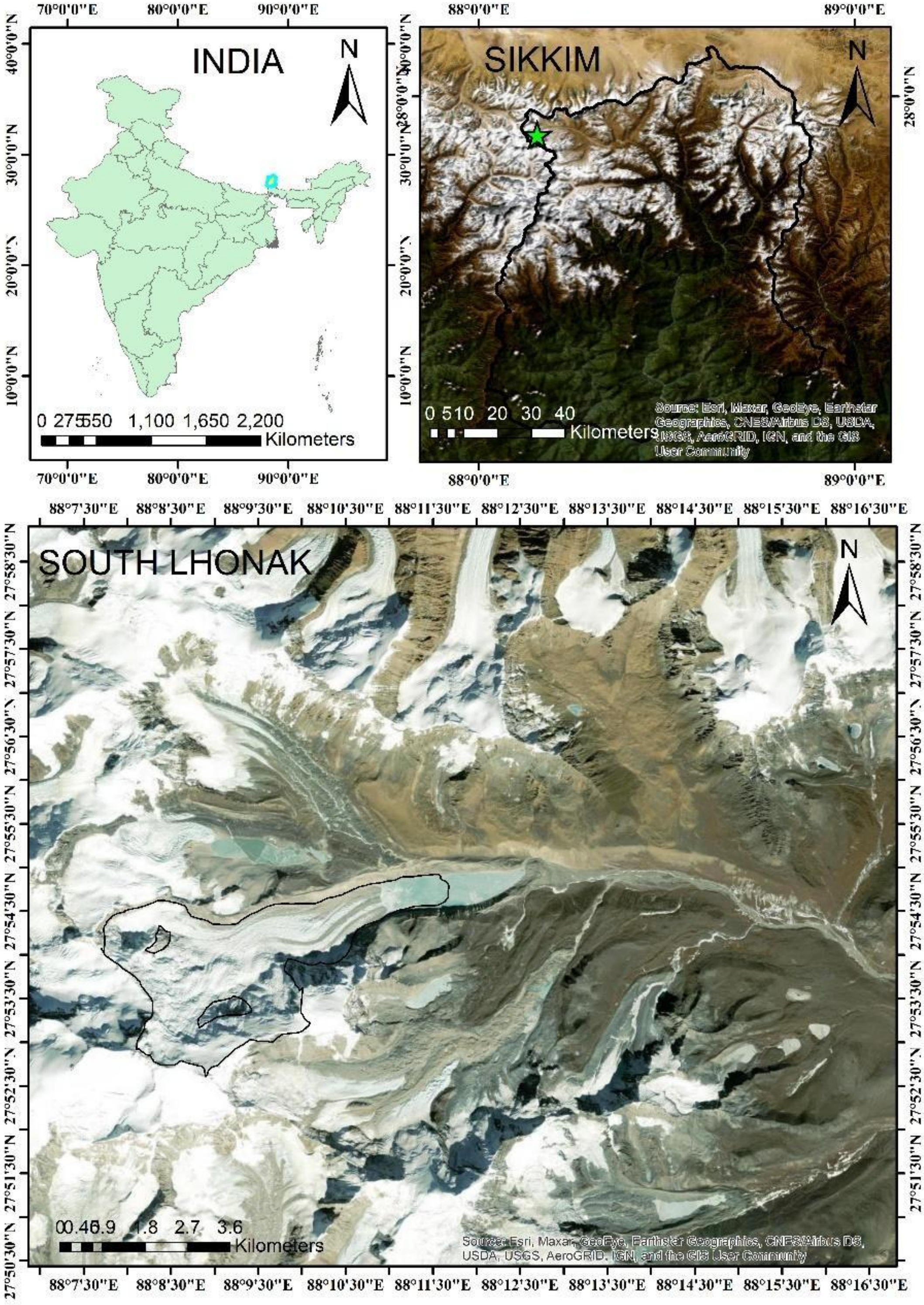

Figure 3.1. The study area is South Lhonak Lake in North Sikkim, India. The star mark shows the location of the glacial lake, and the lake imagery is at the bottom of the image.

South Lhonak Lake (SLL) (27°54'43.63"N and 88°11'37.06"E) is a moraine-dammed glacial lake located in the north district of Sikkim, India. The lake is east-to-west elongated and situated at the tongue of South Lhonak glacier at an elevation of 5200 mean sea level in the Lhonak valley. The headwaters of the valley are formed by the valley glaciers, viz. South Lhonak glacier, North Lhonak glacier, and Lhonak glacier (Sharma et al., 2018).

3.3. Data and Methodology

PRISMA, an Italian Space Agency (Agenzia Spaziale Italiana: ASI) hyperspectral satellite sensor, was sent into orbit on March 22, 2019, and has been used to investigate snow grain size measurement. PRISMA is a single satellite sensor with a repetition cycle of roughly 29 days in a sun-synchronous Low Earth Orbit (620 km altitude). Push broom sensors with 240 contiguous spectral bands (400–2500 nm wavelength region), 66 bands in the Visible Near Infrared (VNIR) range, and 173 bands in the Shortwave Infrared (SWIR) range comprise the PRISMA hyperspectral payload. These sensors have a coherent spectral resolution of about 12 nm narrow bandwidth and 30 m spatial resolution on a 30 km swath width. PRISMA L2D product type acquired on 8th October 2023 is used for this study, which can be directly downloaded from the PRISMA website (https://prisma.asi.it). The L2D product of PRISMA is geocoding (orthorectification) of atmospheric correction and geolocation of the L1 product (bottom-of-atmosphere reflectance, including aerosol optical thickness and water vapor map). The grain size of the JHU snow spectral library is shown in Table 3.1.

Table 3.1. Frost and Snow grain size. The mentioned grain size is the dimension of radius at snow density 250 kg/m³

Snow Grain Type	Grain Size
Frost	50 to 100 µm
Fine Grain Snow	200 µm
Medium Grain Snow	500 µm
Coarse Grain Snow	1 mm

This method requires a hypercube (PRISMA Hypercube) along with endmembers. The JHU snow spectral library is taken as endmembers. Before snow grain size mapping, the JHU snow endmembers (~0.01nm) are scaled to PRISMA satellite spectral resolution (~12nm) using a spline interpolation technique.

After mapping snow grain size, the corresponding energy absorbed by each grain size is estimated using the absorption band area method shown in Eq.3.1. The absorption band area utilizes the fact that both liquid water and ice have absorption features around 1 µm in the spectral region (Nolin and Dozier, 2000). The noise-induced fluctuations are averaged by integrating the absorption feature, yielding a precise estimate near the actual value (Nolin and Dozier, 2000).

$$A_b = \int_{\lambda} \frac{R_c - R_b}{R_c} \quad \text{.......... (3.1) (Nolin and Dozier, 2000)}$$

Where A_b is the absorption band area, R_b is the reflectance spectrum and R_c is the continuum removed spectrum. The equation within integration is called scaled band depth. The energy absorption by mapped snow grain size and JHU snow endmembers are compared to see the trend among the above-mentioned snow grain size (Table 3.1). In the absence of in-situ snow spectra, this absorption band area method is chosen as a validation technique, taking JHU snow grain size spectra as reference data.

3.4. Results and Discussion

The spatial subset of PRISMA hyperspectral data has been done before grain size mapping to focus on the study area. The NDSI threshold for snow cover is 0.4, generally taken in the literature (Marshall and Oglesby, 1994; Awasthi and Varade, 2021). The snow grain size mapping was done using the SID method in MATLAB. The default value of 0.05 is taken as the threshold of SID-based snow grain size classification (Fig.3.2). The SID-based classification shows that the majority of snow grains in the studied area had coarse and medium grain sizes, with much less frost and fine grain size present in comparison.

Due to the unavailability of in-situ measurement of snow grain size, the absorption band area (A_b) method is employed to validate these snow grain size mapping. The $A_b$trend of mapped snow grain size is also compared with their corresponding A_b values of the JHU snow spectral library. An inverse relationship exists between snow reflectance and grain size (Singh et al., 2022), also evident in Fig.3.3(a). The coarse-grain size snow has the lowest reflectance, while the frost has the maximum reflectance. When the grain radius rises, the reflectance spectrum (Fig.3.3(a)) and continuum removed reflectance (Fig.3.3(b-e)) both drop, while the scaled area (Fig.3.3(f)) of the absorption feature grows with the grain size, which is correlated with the absorption efficiency. In other words, a change in the grain size helps to identify the surface features of snow, such as melt area and snowpack energy balance. When the absorption depths for each grain size were investigated using continuum removed (Fig.3.3(b-e)), it was observed that apart from the 1.03 μm spectral region, there are two more prominent absorption depths near 1.5 µm and 2 µm. However, these two new wavelength regions are susceptible to water vapor and carbon dioxide absorption, so they are excluded from grain size mapping.

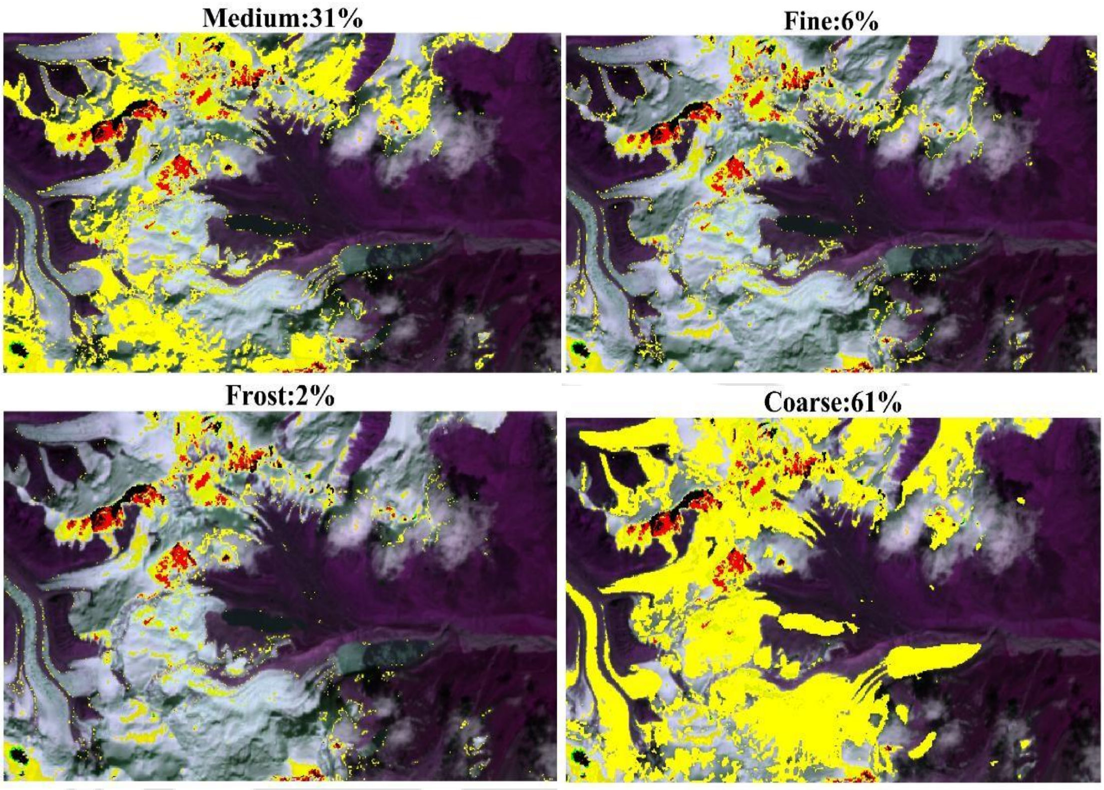

Figure 3.2. Snow grain size mapping using the SID method. The yellow color is overlaid on the true RGB composite PRISMA data. Fine granular snow-6%, Frost-2%, Medium granular snow-31%, Coarse Granular snow-61%.

The scaled band depth (Fig.3.3(f)) for each snow grain size is used in Eq.3.1, and the corresponding wavelength is selected based on the shoulders (Nolin and Stroeve, 1997) of the absorption features at 1.03µm from Fig.3.3(b-e)). The absorption band area in Eq.3.1 for each snow grain size is calculated using the trapezoidal rule. The A_b value of the JHU spectral library shown in Fig.3.4 shows that energy absorption increases with increasing grain size. A similar trend can also be observed for the mapped snow grain size in Fig.3.4.

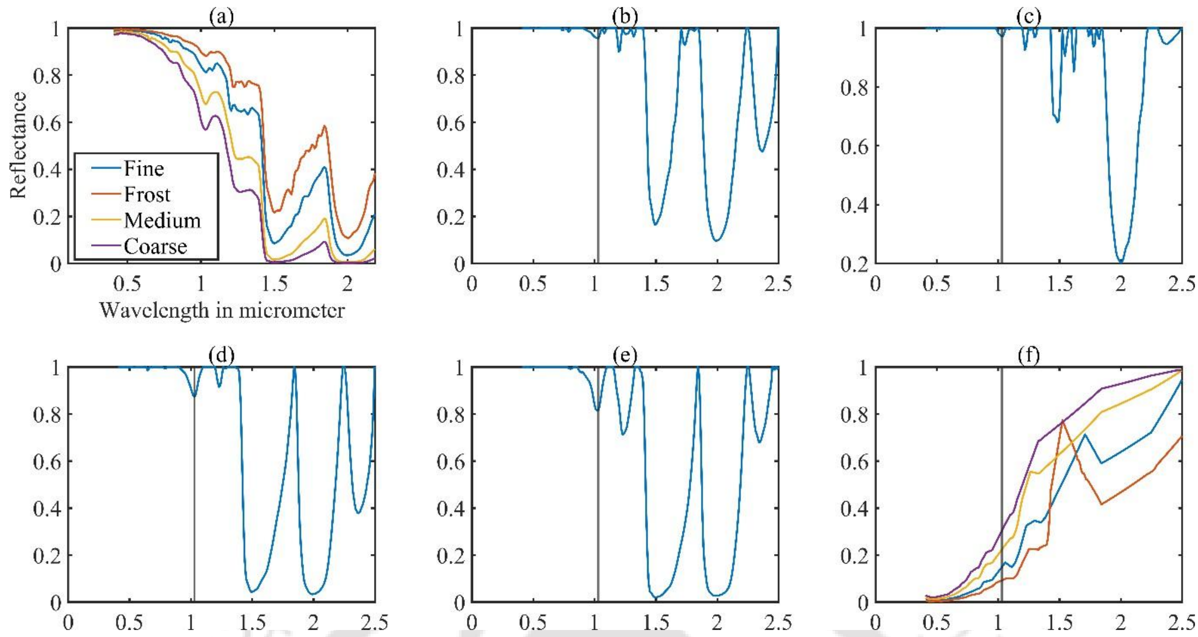

Figure 3.3. (a)-JHU Library Spectra at Satellite resolution; (b) to (e)-continuum removed spectra of fine granular, frost, medium granular, and coarse granular snow, whose y-axis is the continuum removed spectra (absorption) and x-axis is the wavelength (0.41μm-2.5μm); (f)- the scaled absorption depth of the snow grain size as mentioned in (a), whose y-axis is scaled band values and x-axis is the wavelength(0.41μm-2.5μm); The vertical line parallel to y-axis is at a wavelength equal to 1.03μm.

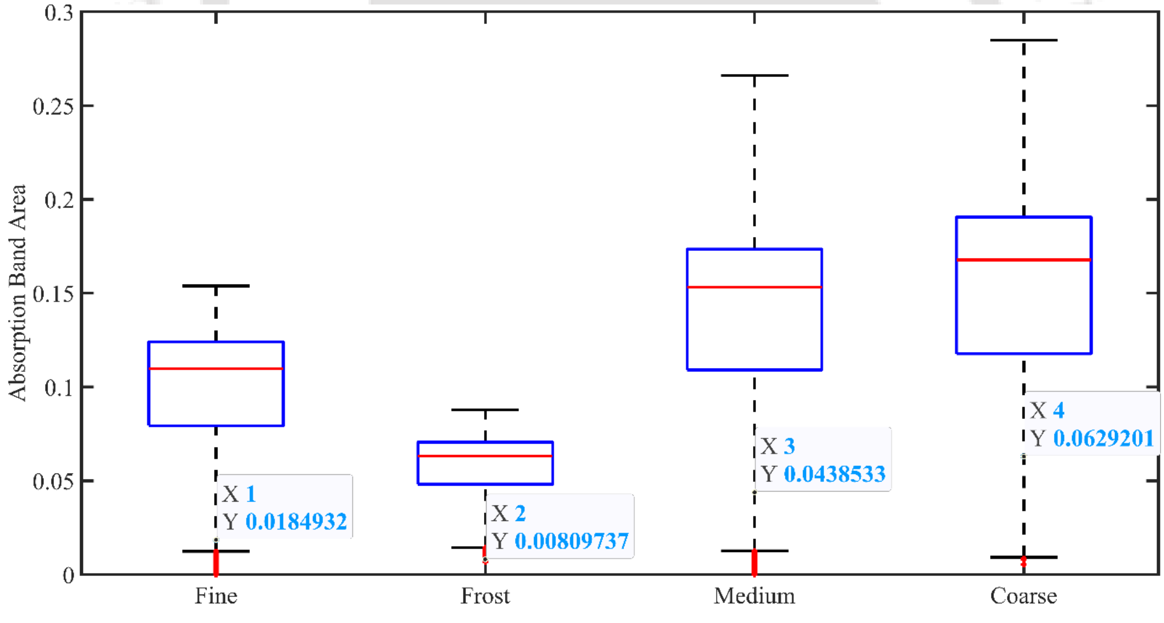

Figure 3.4. The boxplot of the absorption band area for each snow grain size. The marked values show the JHU snow spectral energy absorbed by each snow granular and Frost.

The underlying snow should have been exposed to the surface following the GLOF occurrence, and this snow's grain size should generally be considered coarse-grained, as this analysis's surface layer demonstrates. The spectroradiometer field study should be conducted to validate the modeled snow grain size; however, the tragic incident on October 4, 2023, raises some concerns. Grain size variation aids in determining snow's surface characteristics, including melt area and snowpack energy balance (Nolin and Stroeve, 1997), which agrees with the Himalayan field circumstances in October (when there is snow ablation), and is consistent with this observation.

3.5. Conclusion

The snow grain size mapping for the South Lhonak glacial lake region has been studied using PRISMA hyperspectral L2D. The spatial subset of the hyperspectral data has been confined to the study area. The SID method utilizing PRISMA and JHU snow spectral library for fine, frost, medium, and coarse granular snow has been employed for snow grain size mapping. To characterize the snow's surface characteristics, including melt area and snowpack energy balance, the absorption band area method is applied to map snow grain size. The wavelength region centered at 1.03μm is suitable for understanding the grain size of the snowpack. The energy absorbed by the mapped snow grain size is consistent with JHU snow grain size spectra and Himalayan field circumstances of melting in the ablation period of October.

4

INVERSION MODEL FOR SNOW DIELECTRIC, DENSITY, AND WETNESS

The geophysical properties of snow are essential to studying the snow/glacier system and can be used as an indicator for any related hazard. This study attempts to model the geophysical properties of snow, such as dielectric, density, and wetness, using the Sentinel-1 and PRISMA Hyperspectral datasets. The inversion model was developed utilizing datasets for two distinct glacial regions in Sikkim Himalaya, India.

4.1. Introduction

Snow and ice-based precipitation are the primary sources of mass for glacier systems. The important geophysical parameters of snow, like dielectric constant, density, and liquid water content, play a vital role in avalanche studies, hydrological modeling, and flood monitoring (Manickam et al., 2016). Studying snow geophysical parameters demands the continuous monitoring of snowfall and snowpack characteristics (Jonas et al., 2009). This requires in-situ measurements, which are necessary to evolve a robust model for estimating snow parameters (Foster et al., 1984; König et al., 2001; Rees, 2005; Negi et al., 2015). Though in-situ measurements are challenging and expensive in hilly terrains. This results in the exploitation of remote sensing datasets for retrieving the geophysical parameters of snow (Dozier and Marks,1987; Lenormand et al., 2002; Dietz et al., 2011; Lei and Siqueira, 2015; Dumont and Gascoin, 2016; Thakur et al., 2017; Varade and Dikshit, 2019; Varade et al., 2020; Varade and Dikshit, 2020). The higher altitude snow-covered regions have cloud coverage around the year; thus, optical remote sensing datasets have limitations in such studies (Dozier and Painter, 2004). However, microwave remote sensing has been widely exploited to retrieve snow attributes (Landes et al., 2007; Du et al., 2010). Synthetic Aperture Radar (SAR) data is now accessible in a variety of bands, including X-band (TerraSAR-X, COSMO-SkyMe), L-band (ALOS-2), and C-band (Sentinel-1) (Baghdadi et al., 2016). SAR polarimetry may considerably improve the data quality compared to conventional single-channel SAR. This improvement is due to polarimetric SAR's quantitative ability to scatter mechanisms. The SAR Polarimetry technique has been successfully used in estimating the snow dielectric (Frolov and Ya, 1999; Hajnsek et al., 2003; Singh et al., 2017; Varade et al., 2020), water content (SWC) (Patil et al., 2020; Ma et al., 2020), and density (Singh et al., 2017; Varade et al., 2019). For estimating snow dielectric, density, and liquid water content (LWC), several inversion models have been constructed utilizing dual co-polarized and quad-pol SAR data (Manickam et al., 2016; Snehmani et al., 2010; Thakur et al., 2012; Surendar et al., 2015). Such SAR data utilizes either the backscattering ratio or full-polarimetric SAR decomposition techniques. Unlike these SAR data, Sentinel-1 cannot utilize such techniques because it measures only a column of the scattering matrix for each pixel (VH and VV). However, Mascolo et al. (2021) recently proposed a model-based decomposition for dual-pol data like Sentinel-1. They formed the basis for our novel inversion model, further discussed in detail in the methodology section.

To study the physical parameters of snow, we have selected a region in the Indian Himalayas. The area of the Indian Himalayas (which ranges from west to east) has a considerable amount of snow-covered area with varying levels of glaciation, providing freshwater reservoirs (Singh et al., 2006). The state of Sikkim is located in the Eastern Indian Himalayan Region. The Sikkim Himalayas have continuous snow precipitation patterns in the higher altitudes from February through the end of May, in contrast to the Western Himalayas, where snow areal extent exhibits a falling tendency from March onwards (Kulkarni et al., 2010). Basnett et al. (2012) studied snow-cover monitoring for the four years between 2004 and 2008. They found that the Sikkim Himalayas have different snow accumulation and ablation (melt) patterns than the Western Himalayas. The Himalayan region forms the catchment area of this state's snow-fed Teesta River, which almost cuts through it from north to south. The snow cover in the Sikkim Teesta basin has 251.22 sq. km of permanent snowfields (Bahuguna et al., 2001). The river impacts the way of life of the Sikkimese and other ethnic groups and the economies of Eastern India, some parts of West Bengal, and Bangladesh (Mukhopadya, 1982). The yearly melting of snow cover is crucial for irrigation, hydropower, and adventure tourism. It is pretty concerning that parts of the Himalayas have snow cover. Notably, the state of Sikkim is melting and disappearing (Rai and Mukherjee, 2021), which results in dangerous glacier lakes in Sikkim, India (Worni et al., 2013). Additional natural hazards, such as a snow avalanche that follows an ice avalanche trajectory around some glacier lakes with a moraine barrier, might cause floods in the downstream area as a result of lake outbursts (Worni et al., 2012; Vilimek et al., 2014; Carrivick and Tweed, 2016; Emmer at al., 2016; Dubey and Goyal, 2020); also East Rathong Glacier (RG) in West Sikkim has shrunk by 460 m between 1976 and 2009, according to research by Luitel et al., (2012).

Recently, on October 4, 2023, the South Lhonak Glacial Lake outburst caused severe floods. This caused significant damage and loss, particularly downstream in the Lachen and

Chungthang regions. Due to such challenging field conditions and terrain, in-situ assessment of snow geophysical parameters is impractical. To overcome this challenge, spaceborne imaging spectroscopy emerged as an important tool for mapping snow characteristics. Researchers have pointed to the possibility of using hyperspectral remote sensing to predict snow geophysical parameters (Painter et al., 2013; Donahue et al., 2023; Ravasio et al., 2024). Negi and Kokhanovsky (2011) retrieved the spectral albedo and snow grain size for the western Himalayan snow cover using data from Hyperion sensors. PRISMA (PRecursore IperSpettrale dells Missione Applicativa, or Hyperspectral Precursor of the Application Mission) data was used by Singh et al. in 2022. Ravasio et al. (2024) have employed PRISMA data to retrieve snow liquid water content in the Italian Alps.

Such comprehending variations in Sikkim's snow cover extent, glacier retreat, GLOFs, and freshwater supply motivate us to study the snow geophysical parameters in this region. Studying snow geophysical properties throughout Sikkim may be highly expensive and time-consuming. So, East RG in West Sikkim is chosen as an appropriate test location based on the resources, time, and logistics needed to perform the study. The snow cover study for Sikkim is extensively covered in the research (Basnett et al., 2012; Rai and Mukherjee, 2021). To develop a Sentinel-1-based inversion model for snow physical parameters estimation, we utilize Sentinel-1-derived stokes parameters. Snow is a heterogeneous mixture of air, ice, and liquid water. To characterize snow, it is important to understand the dielectric properties of the mixture. Considering the above-mentioned points, the specific objectives of this study are to 1) propose a state-of-the-art inversion model to estimate the dielectric properties of snow based on Sentinel-1 derived stokes parameters and 2) test the efficiency of the proposed novel inversion model for the scene of the East RG, West Sikkim.

However, for the South Lhonak Glacier region, this study uses PRISMA data to estimate snow geophysical parameters such as snow grain size, wetness, density, and dielectric. For snow grain size mapping, the widely used spectral angle mapper (SAM) technique has been adopted (Singh et al., 2022). The Johns Hopkins University (JHU) snow spectral library is used as a reference spectral signature in the absence of in-situ snow spectra. Further, using the normalized differenced snow index (NDSI) and the triangular/trapezoidal feature space created using the Near-Infrared (NIR) band, the snow surface wetness is determined (Sadeghi et al., 2017; Varade and Dikshit,2018). Using this approach, a least squares-based framework incorporating state-of-the-art empirical models is then utilized to estimate the real part of the permittivity of snow based on the modeled snow LWC. A snow density estimate is obtained using the deduced permittivity and estimated LWC.

4.2. Area of Study and Datasets

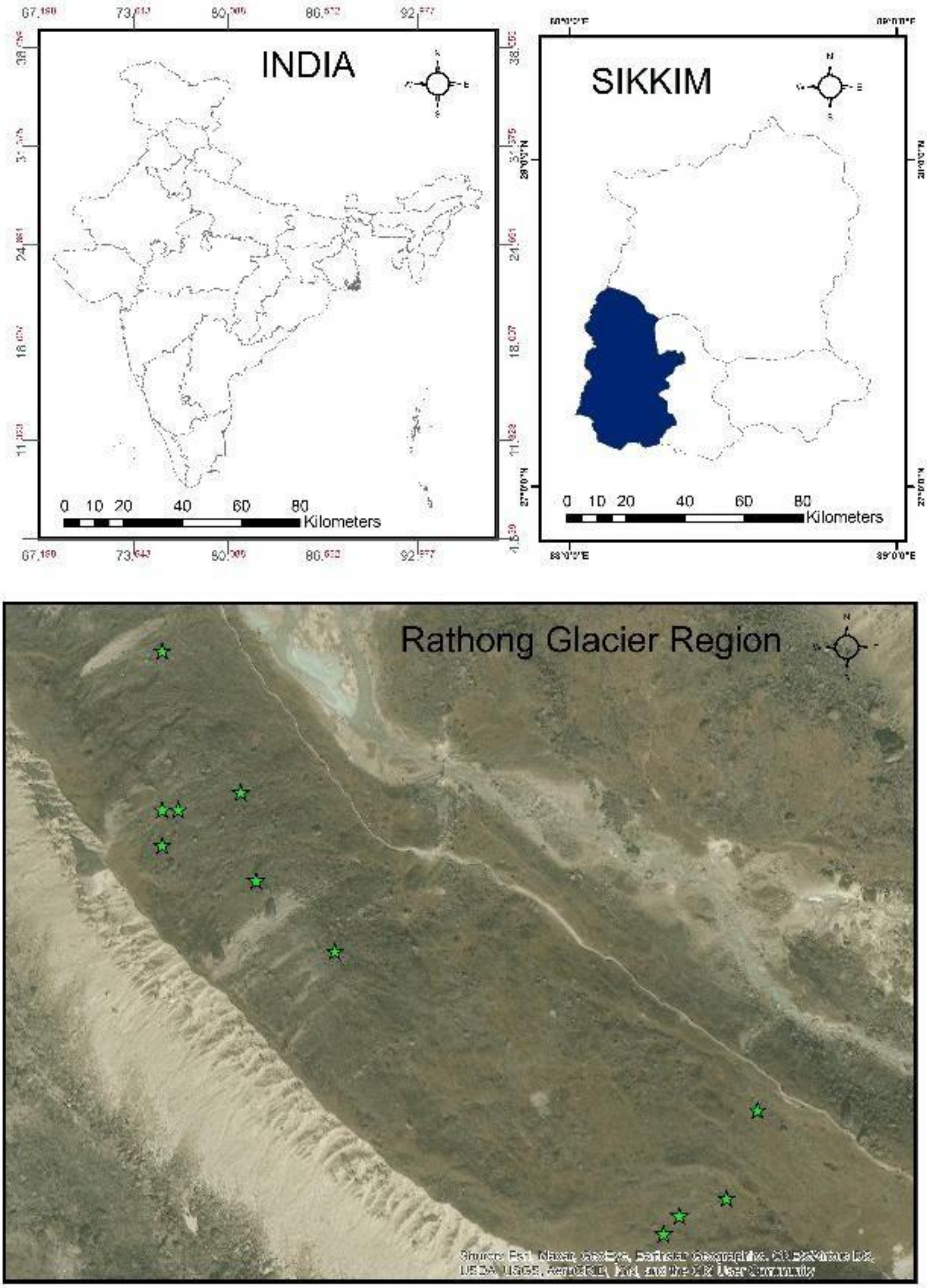

Figure 4.1: Map indicating the study area and the locations of in-situ measurements

The Sikkim Himalayas, which span an area of about 7096 km^2 and are located between latitudes 27° 00′ 46″ and 28° 07′ 48″ N and longitude 88° 00′ 58″ and 88° 55′ 25″ E, are the subject of the current study (Fig. 4.1). It has a steep slope and rocky terrain covering 43% of its land, especially in the state's northern region. The state is covered with roughly 35-40% snow during summers (Singh and Venkataraman, 2009; Basnett et al., 2013).

A field investigation has been carried out from 2 – 8 April 2022 to measure the in-situ snow properties. This investigation includes nearly 45 km of a one-way trek to reach the test site. It starts from Yuksom and ends at Rathong Glacier, near the Himalayan Mountaineering Institute (HMI) advance camp. The way to the test site and test site pictures can be seen in Fig. 4.2.

Figure 4.2: A: HMI base camp, location to stay near the Rathong Glacier, nearly 2 km away. The yellow line with the arrow shows the path to Rathong Glacier. B: Old contaminated snow accumulated in the path to RG. C: Moraine cover Glacier near RG

South Lhonak Lake (SLL) is a glacial lake dammed by moraine and located at 27°54'43.63''N and 88°11'37.06'' E (Fig. 4.3). The lake stretches from east to west and is located in the Lhonak Valley at an elevation of 5200 mean sea level, at the foot of the South Lhonak glacier. The valley's three glaciers—the South, North, and Lhonak glaciers—form the headwaters of the valley—the investigation of the geometric changes in the lake between 2015 and 2023 using C-band Sentinel-1 SAR datasets (Fig. 4.4). The lake's geometric information (length and areal coverage) is acquired through a coupled automated manual delineation approach on the Google Earth engine platform/ArcGIS software. Analyzing the backscatter information of Sentinel-1 datasets shows that the stretch of the lake has substantially increased by 575m (reaching up to 2.946 km) in 2023 before the outburst.

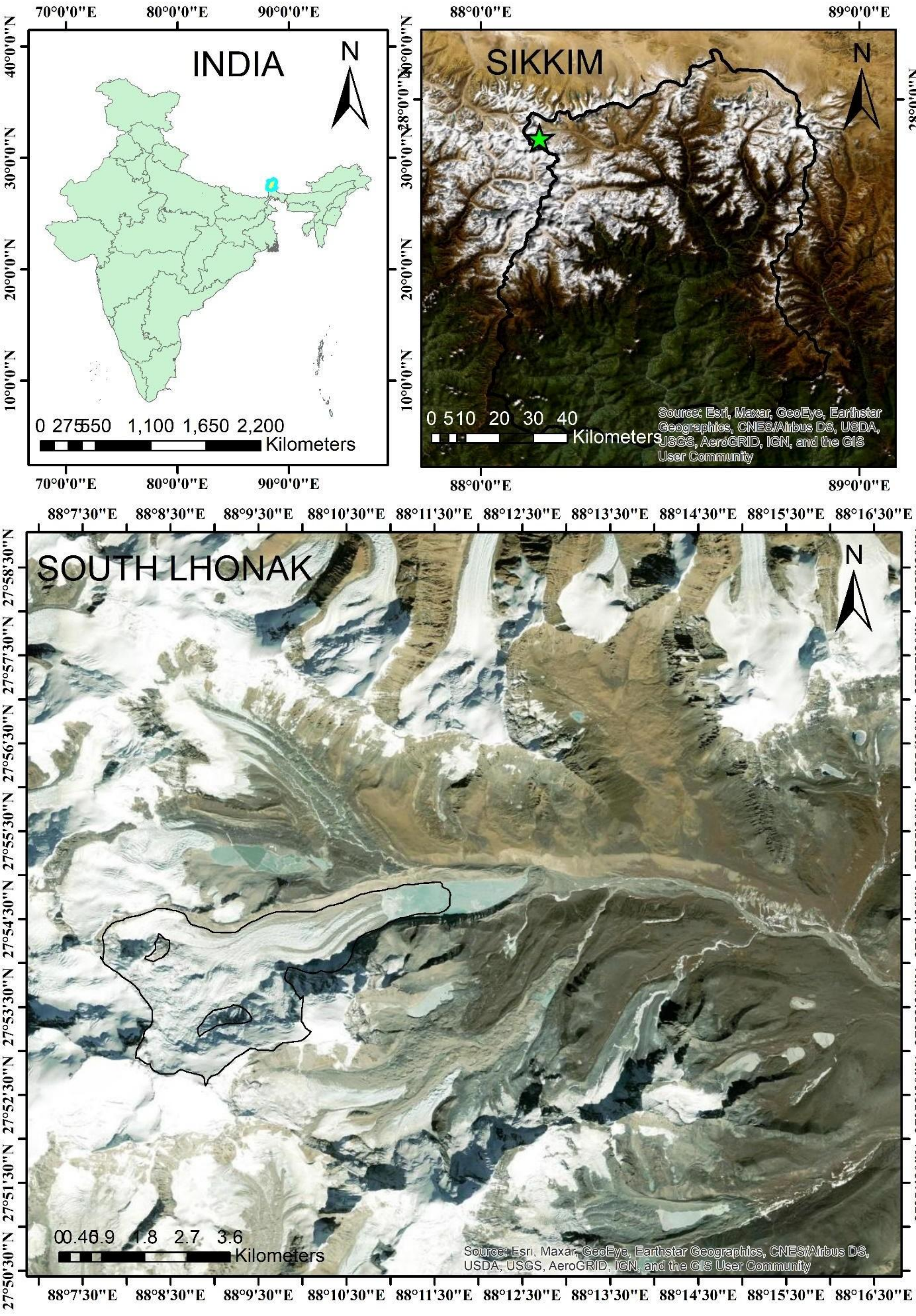

Figure 4.3: The study area map indicates the location of South Lhonak Glacial Lake.

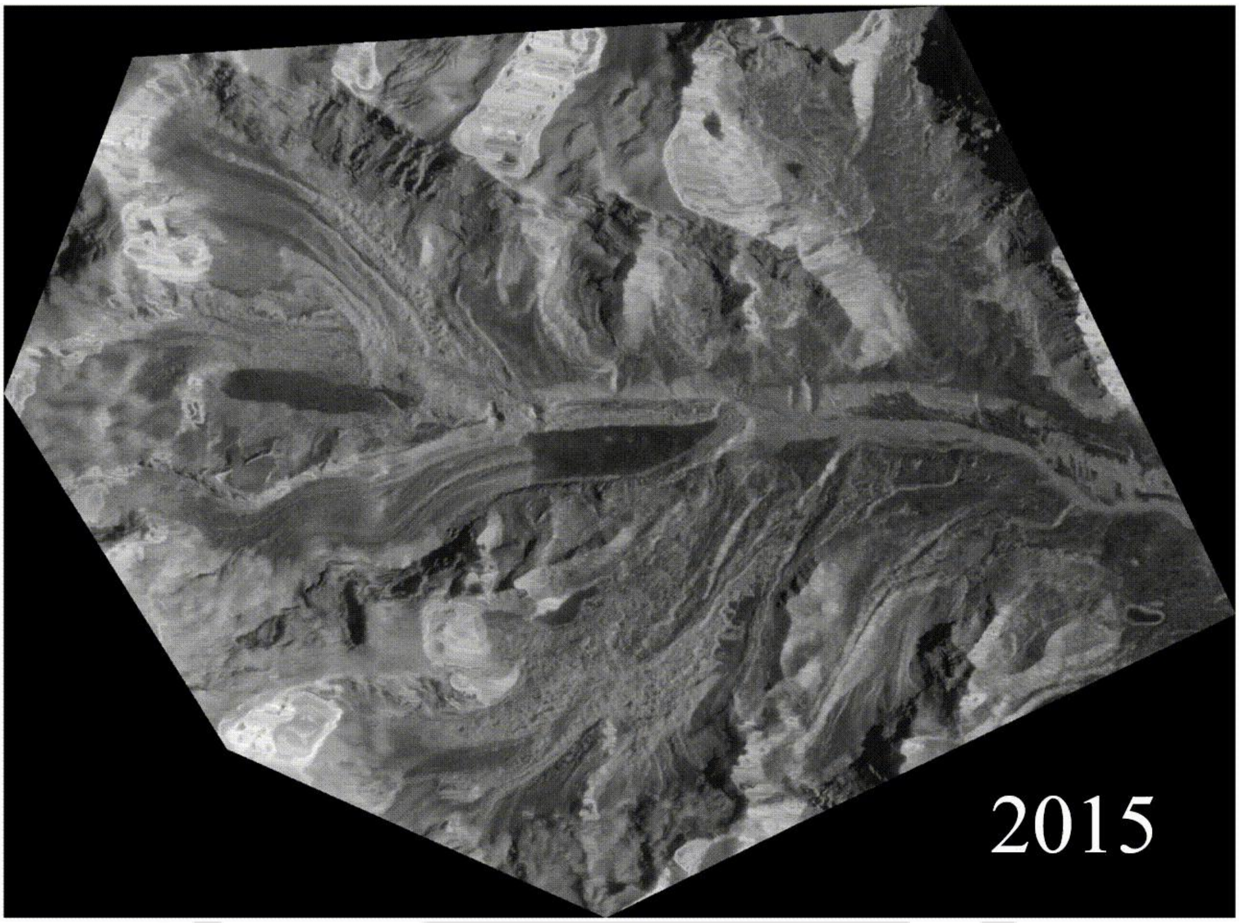

Figure 4.4: Temporal variation of Sentinel-1 (VV) backscattering over the South Lhonak Lake from 2015 to 2023-AE (01 Oct-15 Oct 2023). The event was marked on 04th October 2023.

Its average annual expansion rate is 0.05 km² in the last 8 years (2015 to 2022). As mentioned below, the lake volume (V) is calculated using the well-established empirical equation for South Lhonak Lake using the lake area (A).

$V = 0.0522 * A^{1.766}\ at\ R^2 = 0.99$ (Sharma et al., 2018)

Where, V: volume, A: Area and R^2: Coefficient of determination between V and A

The average volume of water in the lake from 2015 till 2023 (before the GLOF) is observed to be 102.4 million m^3, which is 55.59% more than the lake volume in 2014-2016 (65.8 million m^3). After the event, there is approximately a 79.44% decrease in the lake volume, a 59% decrease in the lake area, and a 48.40% decrease in lake length. The most significant change in the lake area is observed between 2020 and 2021 (Fig. 4.5).

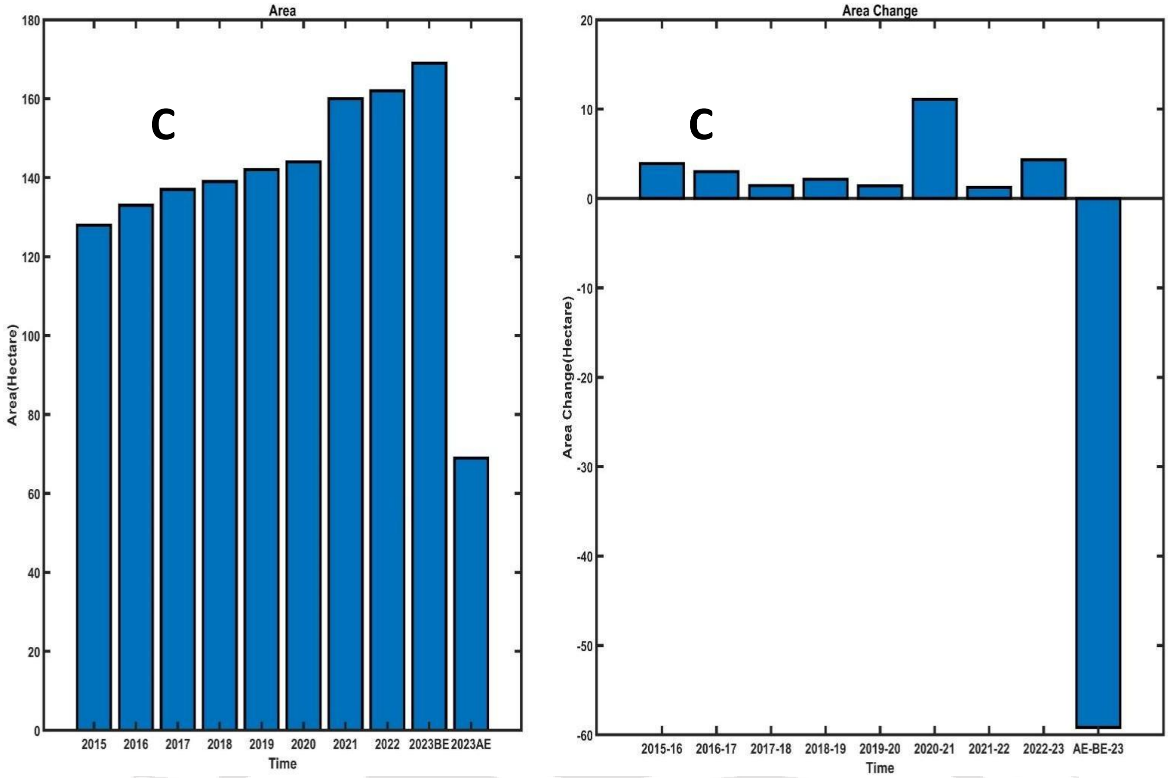

Figure 4.5: C1-Area (Hectare) of SLL from 2015 to 2023 AE; C2-Change in Area for the same time period.

4.3. Field Instrument

Snow dielectric, density, and wetness are measured using the Snow Fork instrument at an altitude between 4500 and 5000 meters above the mean sea level. The measurement utilizes the resonant frequency ranges from 0.5 – 1 GHz, density ranges 0 – 0.6 g/cm^3, liquid water content (LWC) ranges from 0 – 10%, dielectric constant ranges from 1 – 2.9 (Real) and 0 – 0.15 (Imaginary) with an accuracy of 0.02 and 0.002, respectively. Before starting actual in-situ measurements, the snow fork is calibrated in the air, and the frequency 890.1 MHz (888 – 892 MHz), bandwidth 20.8 MHz (18–23), and attenuation 1799 (1600–3000) fall within the prescribed ranges. To evaluate the modeled snow geophysical characteristics, field campaigns that matched the test datasets were scheduled in April 2022 to gather in-situ measurements. The in-situ measurements through the Snow fork have been considered reliable in determining snow's physical properties (Tiuri et al., 1984; Varade et al., 2010). The snow's dielectric, density, and moisture values were measured by placing the needle of a snow fork horizontally in the snow pit. Typically, the measurement should be taken at a 2 cm interval in the vertical direction. There were 11 different point measurements taken along the locations in the Rathong Glacier Path (RGP) (see Fig. 4.1).

4.4. Satellite Data

4.4.1. Rathong Glacier Region

The Sentinel-1A with descending pass acquired the data on 6 April 2022, while the field measurements were performed on 7 April 2022. The level-1 SLC product of Sentinel–1A dual polarimetric (VV/VH) Interferometric Wide (IW) swath mode C-band SAR dataset has been accepted in this study. The C–band of Sentinel–1A has a 5.405 GHz central frequency. The Sentinel Application Platform (SNAP) v8.0 has been used to pre-process the level-1 SLC product following the instructions provided by Elkharrouba et al. (2022) (see Fig. 4.6).

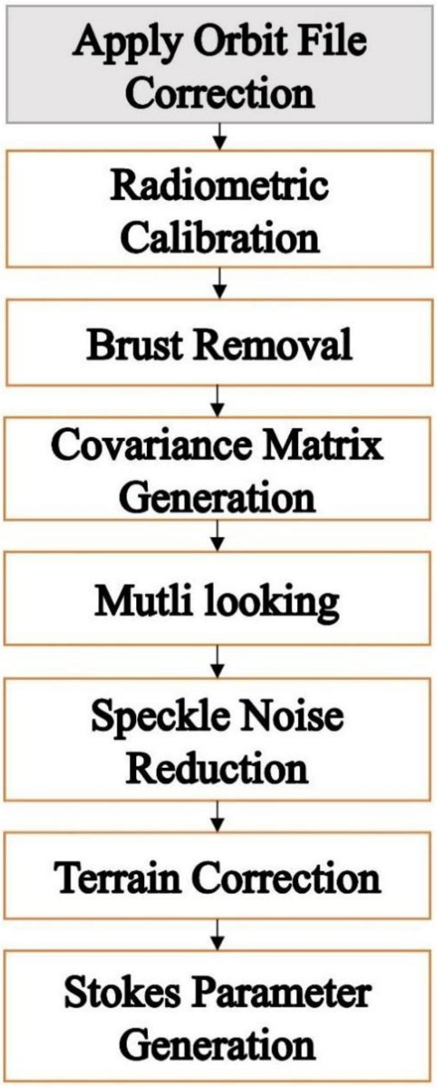

Figure 4.6: Flow chart of Sentinel-1 Pre-processing

4.1.2. South Lhonak Lake

PRISMA hyperspectral sensor was launched on March 22, 2019, by the Italian Space Agency (ASI) with approximately 29 days repeating cycle. It provides 240 continuous spectral bands between 400–2500 nm wavelength region with 30 m spatial resolution. This study uses the bottom-of-atmosphere reflectance data from PRISMA (L2D product) of October 8, 2023. The snow grain sizes considered in this study are from the JHU snow spectral library (Table 4.1).

Table 4.1: Frost and Snow grain size. The mentioned grain size is the dimension of radius at snow density 250 kg/m³

Snow Grain Type	Grain Size
Frost	50 µm to 100 µm
Fine Grain Snow	200 µm
Medium Grain Snow	500 µm
Coarse Grain Snow	1mm

4.5. Methodology

Method-I (Rathong Glacier Region): The adopted processing for the stokes parameters estimation includes orbital correction, radiometric calibration, splitting them into three sub-swaths (IW1, IW2, IW3), burst removal for each sub-swath, and subsequently merging them all. It is followed by covariance matrix production, multi-looking, speckle noise reduction, terrain correction, and Stokes parameters (Raney, 2006). The Stokes parameters of the received data contain all available polarimetric information (Raney, 2019). The formula to obtain Stokes parameters and other parameters needed for the inversion model is discussed in the subsequent sub-section.

4.5.1. Formulation of Dual-pol Stokes Vector

Sentinel-1 dual-pol SLC data, after applying the orbit file, undergoes radiometric calibration, which is saved as complex output, in order to obtain a 2-element complex vector called coherency matrix C2 (see Eq. 4.1) for each pixel in the image.

$$C2 = < \begin{bmatrix} E_{HT} \\ E_{VT} \end{bmatrix} \begin{bmatrix} E^*_{HT} & E^*_{VT} \end{bmatrix} > = \begin{bmatrix} C_{11} & C_{12} \\ C^*_{12} & C_{22} \end{bmatrix} \ldots\ldots\ldots (4.1)$$

Where subscript T is transmitted polarization of state

The Stokes vector (s) for a scattered wave is entirely determined from the C2 matrix as follows (see Eq. 4.2-4.3)

$$s = [s_1\ s_2\ s_3\ s_4]^T = [(c_{11} + c_{22})\ \ (c_{11} - c_{22})\ \ 2Re(c_{12})\ \ 2Im(c_{12})]^T \ldots\ldots (4.2)$$

$$C2 = 0.5 * \begin{bmatrix} s_1 + s_2 & s_3 - js_4 \\ s_3 + js_4 & s_1 - s_2 \end{bmatrix} \ldots\ldots\ldots\ldots\ldots\ldots (4.3)$$ (Lee and Pottier, 2017; Elkharrouba et al., 2022)

The mapping of the T3 matrix of quad-pol into the dual-pol Stokes vector is shown in Mascolo et al. (2021) (see Eq. 4.4)

$$s = \begin{matrix} t_{11} + t_{22} + t_{33} \pm 2\cos(2\theta)\,Re(t_{12}) \\ 2\cos(2\theta)\,Re(t_{12}) \pm (t_{11} + \cos(4\theta)\,(t_{22} - t_{33})) \\ 2\sin(2\theta)\,Re(t_{12}) \pm \sin(4\theta)\,(t_{22} - t_{33}) \\ 2\sin(2\theta)\,Im(t_{12}) \end{matrix} \quad \ldots\ldots\ldots\ldots\ldots (4.4)$$

Where t_{11}, t_{22}, t_{33} *and* t_{12} are the elements of the T3 matrix. Upper sign for H transit and lower for V and θ misalignment between radar coordinates (H or V) and the scene symmetric axis.

In quad-pol, under the assumption of reflection symmetry, the coherency matrix (Hajnsek et al., 2003) is written as follows (see Eq. 4.5), and this matrix is used to map the dual-pol stokes vector using the general mapping of reflection symmetry.

$$[T] = \begin{matrix} <|R_s + R_p|^2> & <(R_s - R_p)(R_s + R_p)^*> & 0 \\ <(R_s + R_p)(R_s - R_p)^*> & <|R_s - R_p|^2> & 0 \\ 0 & 0 & 0 \end{matrix} \ldots\ldots\ldots (4.5)$$

Hence $t_{11} = |R_s + R_p|^2$, $t_{22} = |R_s - R_p|^2$, *and* $t_{33} = 0$… .... (4.6)

Similarly, the mapped Stokes vector for the tilted Pauli phase (Mascolo et al., 2021) is as follows

$$s = \begin{matrix} 1 \pm \cos(2\theta)\cos(2\phi) \\ \cos(2\theta)\cos(\phi) \pm 0.5 * (1 + \cos(4\theta)) \\ \sin(2\theta)\cos(\phi) \pm 0.5 * (\sin(4\theta)) \\ \sin(2\theta)\sin(\phi) \end{matrix} \quad \ldots\ldots\ldots (4.7)$$

It also confirms that Eq.4.7 satisfies many natural media varying from forest to land-ice (Hajnsek et al., 2021). To represent dual-pol stokes vector in terms of R_s *and* R_p (See Hajnsek et al., 2003 for the representation of R_s *and* R_p in terms of complex permittivity and local incidence angle), Eq.4.4 to Eq. 4.7 has been employed to develop the inversion model. It has one transmitter for V polarization and two for V and H polarization receivers. Thus, in all equations, we use the minus (–) sign, which is the upper sign for H transit and the lower for V.

After rearranging the system of equations in Eq. 4.7, θ is found to be

$$\theta = (0.5) * tan^{-1}\left(\frac{s_1+s_2}{s_4-s_3}\right) \ldots\ldots\ldots\ldots (4.8)$$

Thus θ value can be calculated using Eq. 4.8 using dual-pol stokes vectors for Sentinel-1. Now replacing θ in Eq. 4.4 and rearranging Eq.4.4, we obtained our desired equations that we proposed as a novel inversion model based on Sentinel-1 derived Stokes vector (see Eq. 4.9)

$$\frac{|R_s - R_p|^2}{|R_s+R_p|^2} = \frac{\left(2*\frac{s_1+s_2}{\cos(4\theta)}\right)}{4s_1+2s_2+2s_3\cot(2\theta)} \ldots\ldots\ldots (4.9)$$

Thus Eq. 4.9 is independent of surface roughness and depends only on dielectric and local incidence angle—a similar ratio on the LHS of Eq. 4.9 can be seen in Eq. 22 of Hajnsek et al. (2003).

Hence, a new inversion model is formulated based on the Stokes parameters to obtain dielectric values. The efficiency of this model was tested using the Sentinel-1-derived Stokes parameter. The permittivity related to snow density is determined by Looyenga's equation (Eq. 4.10). The earlier studies (Tiuri et al., 1984; Denoth, 1989, 1994; Kendra et al., 1994) state that LWC, permittivity, and density are related in nature and are based on the linear mixing of the dry snow dielectric constant ρ_{ds} with the rise in dielectric constant generated by LWC in the snow, as shown in Eqs. 4.11, 4.12, 4.13, and 4.14, respectively.

$$(\varepsilon_r') = 1+1.5995\rho_s+1.861\rho_s^3 \ldots\ldots\ldots (4.10)$$

$$\varepsilon_s = \varepsilon_{ds} + \Delta\varepsilon_{ws} \ldots\ldots\ldots\ldots\ldots\ldots (4.11)$$

$$\varepsilon_{ds} = 1 + 1.7\rho_{ds} + 0.7\rho_{ds}^2 \ldots\ldots (4.12)$$

$$\Delta\varepsilon_{ws} = 0.187\text{w} + 0.0045w^2, \Delta\varepsilon_{ws} = 0.089\text{w} + 0.72w^2, \Delta\varepsilon_{ws} = 0.206\text{w} + 0.0046w^2 (4.13)$$

$$w = 5.35[\varepsilon_s - (1 + 1.92\rho_{ds})] \ldots\ldots\ldots (4.14)$$

Method-II (South Lhonak Lake): The endmembers are the JHU Snow Spectral Library (~0.01nm), resampled to the spectral resolution of PRISMA (~12nm) using spline interpolation. The atmospherically corrected PRISMA hyperspectral cube is subjected to dimensionality reduction to extract the most informative bands corresponding to the JHU snow spectra.

$$NDSI = \frac{R_{0.60}-R_{2.01}}{R_{0.60}+R_{2.01}} = \frac{Green-SWIR}{Green+SWIR} \ldots\ldots\ldots (4.15)$$

Where $R_{0.60}$ and $R_{2.01}$ is surface reflectance at a wavelength of 0.60µm and 2.01µm, respectively. The snow grain size endmembers are obtained from the snow hypercube using the Fast Iterative Pixel Purity Index (FIPPI).

The soil moisture assessment, the trapezoidal/triangular feature space based on the land surface temperature (LST) or NIR reflectance, and the NDVI have been utilized extensively in the literature (Sadeghi et al., 2017). The response of the near-surface snowpack can be studied using spectral data in the visible and infrared bands in an integrated framework for monitoring the LWC in the snowpack. The approach relies on the physical interaction between light and snow, where snow properties such as grain size and liquid water content affect the spectral reflectance observed in the electromagnetic spectrum's visible and near-infrared (NIR) regions. Due to higher absorption of the incident light wave caused by the increased liquid water content in the snow, wet snow has a considerably lower spectral reflectance in the visible and infrared spectrum when compared to dry snow. Using a trapezoidal/triangular feature space (Fig. 4.7) based on the NIR reflectance and the NDSI, the spectral reflectance's sensitivity to the liquid water content in the snow is used to establish a framework for determining snow geophysical parameters in this study.

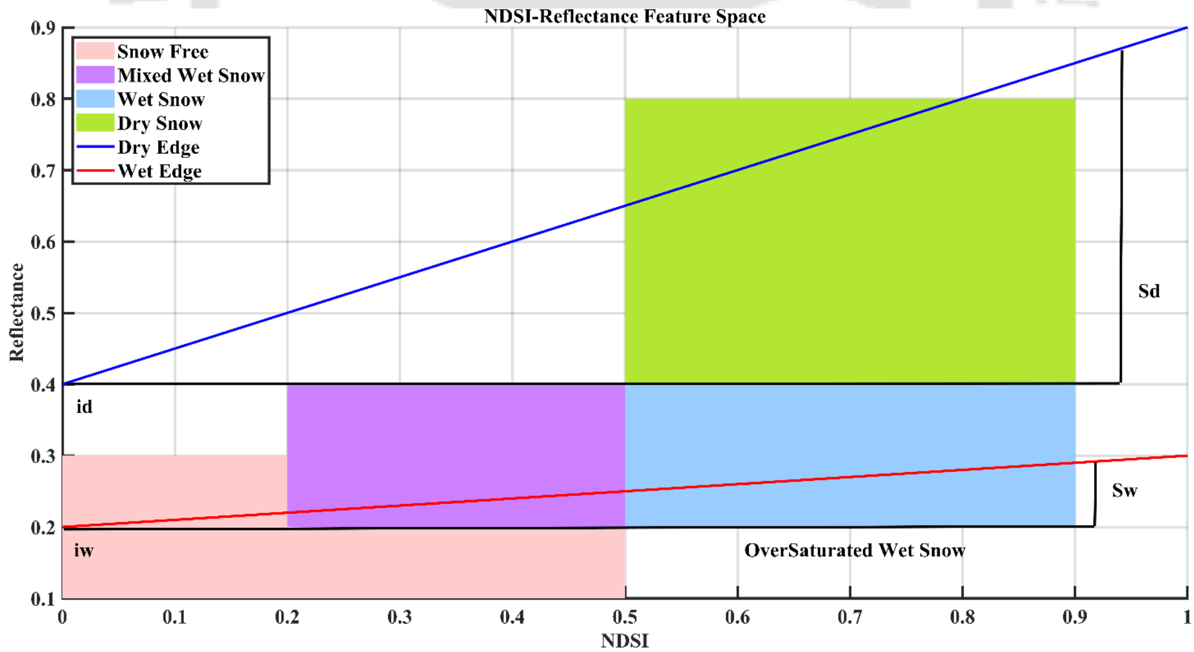

Figure 4.7: The X-axis represents the Normalized Difference Snow Index (NDSI), ranging from 0 to 1, differentiating snow from non-snow surfaces. The Y-axis corresponds to near-infrared (NIR) reflectance and is sensitive to snow grain size and liquid water content. Key regions include dry snow (high NDSI and reflectance), wet snow (high NDSI but lower reflectance due to increased absorption from liquid water), snow-free areas (low NDSI and reflectance), and mixed damp and dry snow (intermediate characteristics). The dry and wet edges define the upper and lower reflectance limits for dry and wet snow. Pixel distribution within this feature space reveals varying snowpack conditions, with clustering reflecting liquid water content levels. This

approach enables differentiation between snow types and supports estimating parameters like snow wetness, grain size, and surface conditions, which are critical for snowpack analysis and geophysical modeling

The NIR band sensitive to snow grain size is identified to be ~1.03µm (Ravasio et al., 2024), which is opted for snow surface wetness estimation. The modified NIR-NDSI feature space and the scatter distribution between NDSI and NIR band reflectance are used to estimate snow surface estimation. Lower liquid water content (LWC) pixels are found in the scatter distribution in the NIR-NDSI region surrounding the dry edge. In contrast, higher LWC pixels are found around the wet edge. In the NIR-NDSI feature space, dry snow pixels are found in the upper right corner, and wet snow pixels are found in the lower right corner. These observations allow for the following definition of snow wetness: (w):

$$w = \frac{i_d + (s_d * NDSI) - NIR}{(i_d - i_w) + (s_d - s_w) * NDSI} \ldots\ldots\ldots\ldots (4.16)$$

Where, i_d, i_w, s_d, s_w are the intercept and slope of the dry and wet edges.

LWC, permittivity, and density are among the snow geophysical parameters coupled in nature (Eqs. 4.11, 4.12, 4.13, and 4.14). Snow dielectric and density are estimated using the state-of-the-art empirical models shown in Eq. 4.11 to Eq. 4.14. The least squares solution for snow dielectric was found using the corresponding values of LWC. Further, the derived snow dielectric calculates snow density using the model defined by Looyenga (1965) (Eq. 4.10).

4.6. Results and Discussions

Rathong Glacier Region: Each component (s1, s2, s3, and s4) is considered nonzero when the Stokes vector for Sentinel-1 is calculated. The theta (θ) is the angle formed by the scatter's symmetry axis, and the radar transmits polarised signal axes. The return signal is always co-polarized with the transmitter when this θ value is zero, which denotes that the surface has no slopes (reflection like a simple mirror) (Mascolo et al., 2021). Since the study area is hilly terrain, hardly it will have such value. The histogram plot for θ is seen in Fig. 4.8 and is observed as non-zero.

According to Mascolo et al. (2021), as long as θ is non-zero, we will have the following inferences: (1) obtain a complete Stokes vector from dual-pol systems, (2) the dual-pol SLC data employed is entirely coherent, (3) s4 parameter is non-zero (thus meet the requirement for Eq. 7). The proposed inversion model based on Sentinel–1 derived Stokes coefficient is applied to a portion of the Sentinel–1 scene acquired on 6 April 2022. The model shown in Eq. 4.9 is solved to retrieve the dielectric values, and subsequently, density is estimated using Eq. 4.10. The wetness is modeled using a set of equations (4.11-4.14).

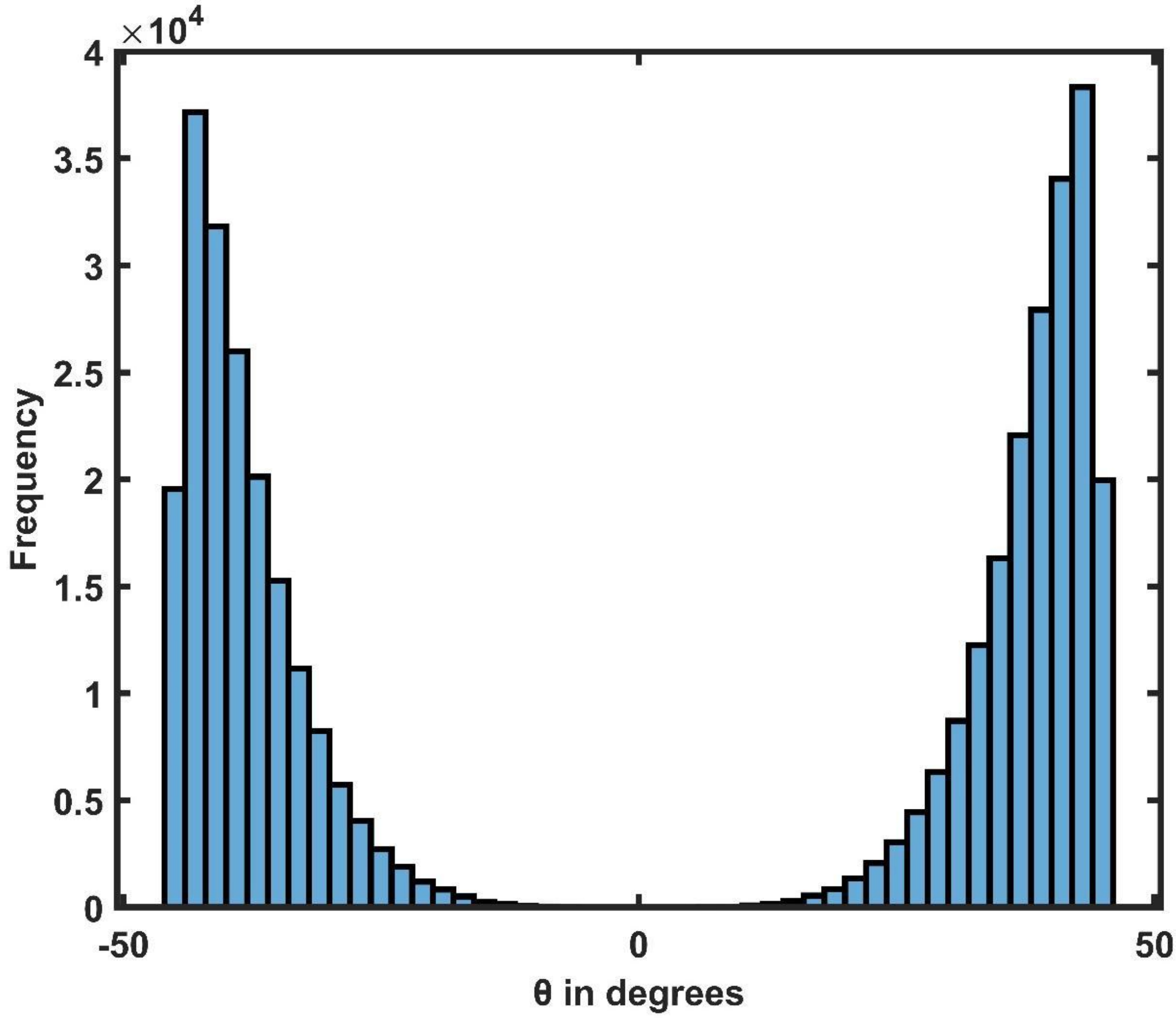

Figure 4.8: Histogram of the angle of the scatterer's symmetric axis with the radar V or H axes. It is also called the orientation angle

According to Ponnurangam et al. (2015), Eq. 4.10 is substituted in Eq. 4.14 to estimate the initial value of dry snow density by taking snow wetness equal to zero. The dry density of snow is found to be 0.415 g/cm^3. The dry snow density mainly varies from 0.25-0.30 g/cm^3, but it can be more than 0.350g/cm^3 due to trampling of snow by human activity (Li et al., 2022). It is observed that trekkers frequently visit the point of measurement along the RGP. Since the number of in-situ measurements is less and for a particular scene in the spatial stretch of around 200m, we have assumed the dry snow density to be constant. This constant value is used in Eq. 4.12 to determine the dry snow dielectric, and subsequently, Eq. 4.11 and Eq. 4.13 are utilized to obtain the wetness value. In the in-situ data, the dielectric constant, density, and wetness vary from (1.28 – 2.53), (0.145 – 0.511) g/cm^3, and (0.11–4.83) %. Among 11 points, there are two points, which are points number 3 and 8 (see Fig.4.1C), which have wetness of less than

1% and density range from 0.147-0.161 g/cm^3. This density range comes in the category of damp new snow (Cuffey et al., 2010), and this kind of snowfall is observed in the field. The rest of the in-situ locations have wetness of more than 1%, thus can be said to be wet snow, which is typically the case in the ablation period. Since the snow depth in the field was shallow, the physical properties along the vertical depth are not discussed. The snow dielectric, density, wetness, and an RGB composite image are shown in Fig.4.9.

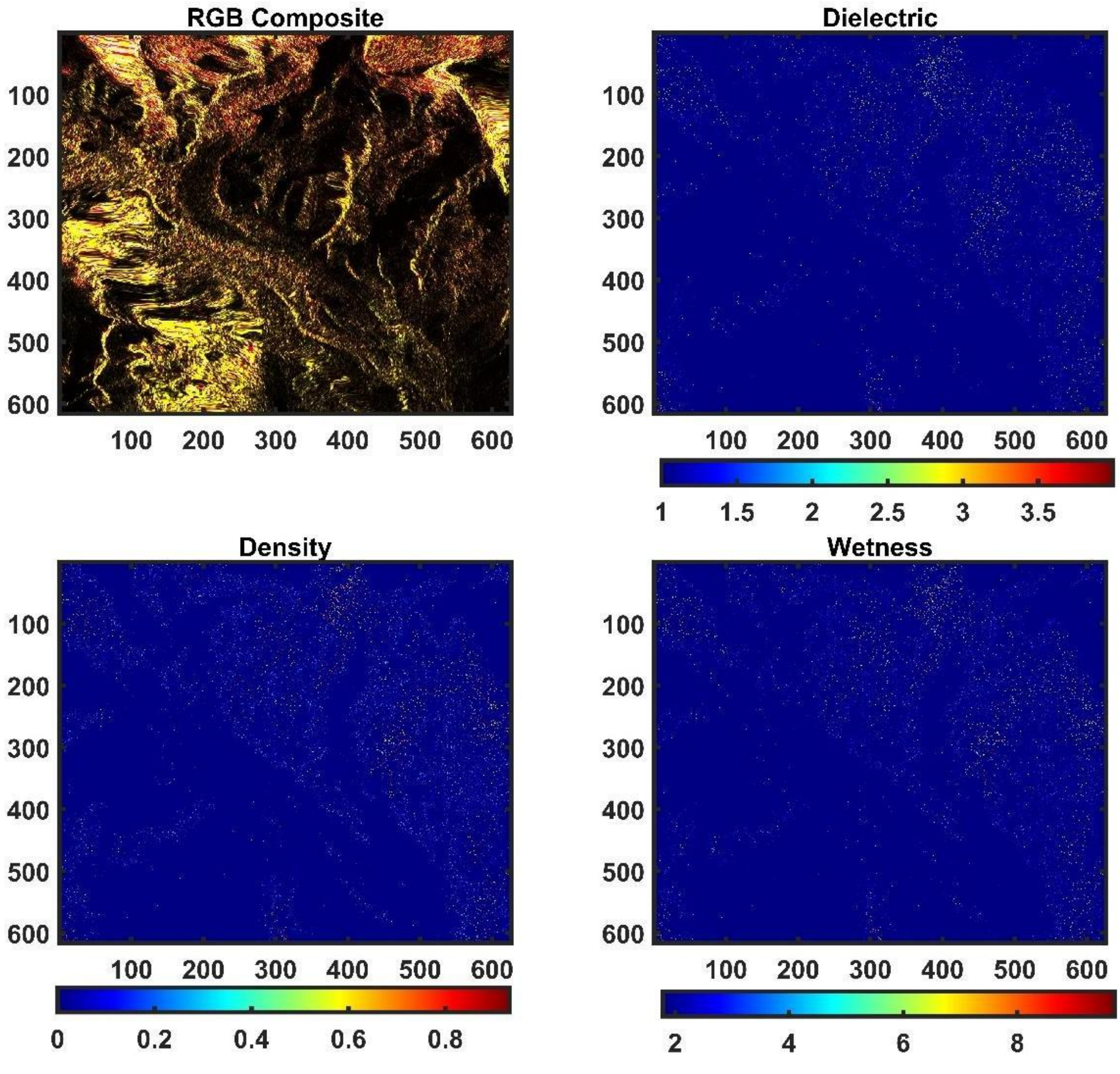

Figure 4.9: RGB composite image of Sentinel-1 derived Stokes coefficients (Red-s1, Green-s2, Blue- s3), Modeled snow dielectric, density, and wetness map for the subset of the scene including the investigating area as well as the Rathong Glacier region

Since the study area had cloud cover during the field investigation, the snow cover image using optical data has not been shown here. The map of the scene shown here also covers Rathong Glacier, and the density of the glacier ranges from 0.830-0.923 g/cm^3 (Cuffey et al., 2010). Based on the density ranges (0.10, 0.20, 0.25–0.30, and 0.40 g/cm^3), snow can be classified into four categories: fresh, settled, old, and moist (Melysund et al., 2007). The measured snowpack in the field has been determined to be settled, old snow, and moist. It is observed from the field data that there is snow, which reflects the continuous nature of snow transformation, which is very common in glacial environments (Cuffey et al., 2010). A few statistical analyses have been performed to check the efficiency of the proposed inversion model. The first one is the box plot, which shows a simple summary of the distribution of results. The box plot of the modeled (results) and observed data (in situ) is shown in Fig. 4.10.

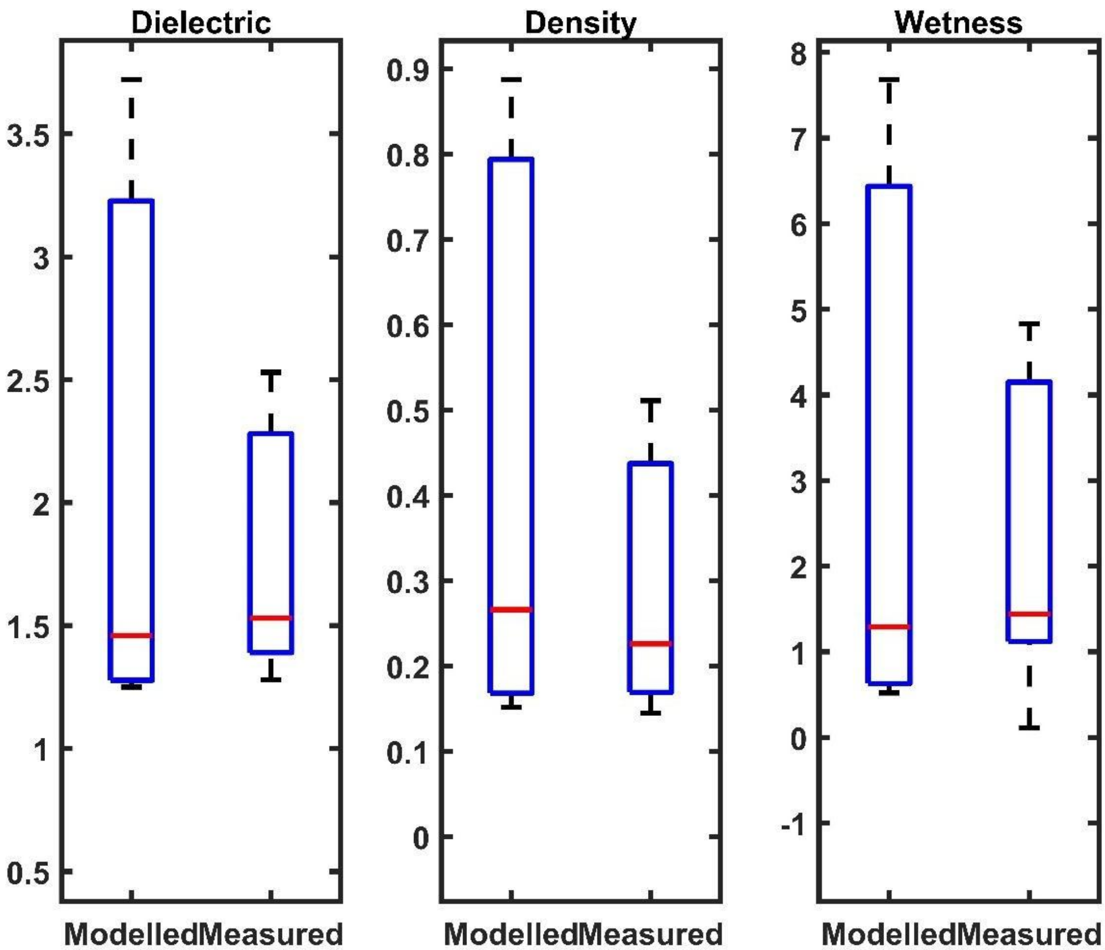

Figure 4.10: Box plot of the modeled and in-situ snow geophysical parameters. The dielectric constant is dimensionless, whereas density is measured in g/cm^3, and wetness is the percentage by volume

Snow dielectric, density, and wetness (LWC) are compatible with the measured values, according to the median seen from the boxplot. It is also evident from the box in the plot that modeled parameters are overestimated. The linear fit between the modeled and measured values is shown in Table 4.2, along with its scale and bias parameters. The graphs of the correlation between the modeled and measured parameters are shown in Fig. 4.11. The estimated values of the dielectric, density, and LWC are found to accord (R^2>0.7) with the measured values of these quantities. Due to the absence of intermediate values, it can be observed in the box plot that all parameters (left-skewed) are deviated from standard normal distribution.

Table 4.2: Linear fit of snow geophysical properties

Parameters	Coefficients (95% confidence bounds) (p1×(x)) +p2	R^2	RMSE
Snow Dielectric constant	(0.4, 0.97)	0.74	0.26
Snow Density	(0.38,0.13)	0.72	0.0781
Snow Wetness	(0.53, 0.73)	0.8	0.847

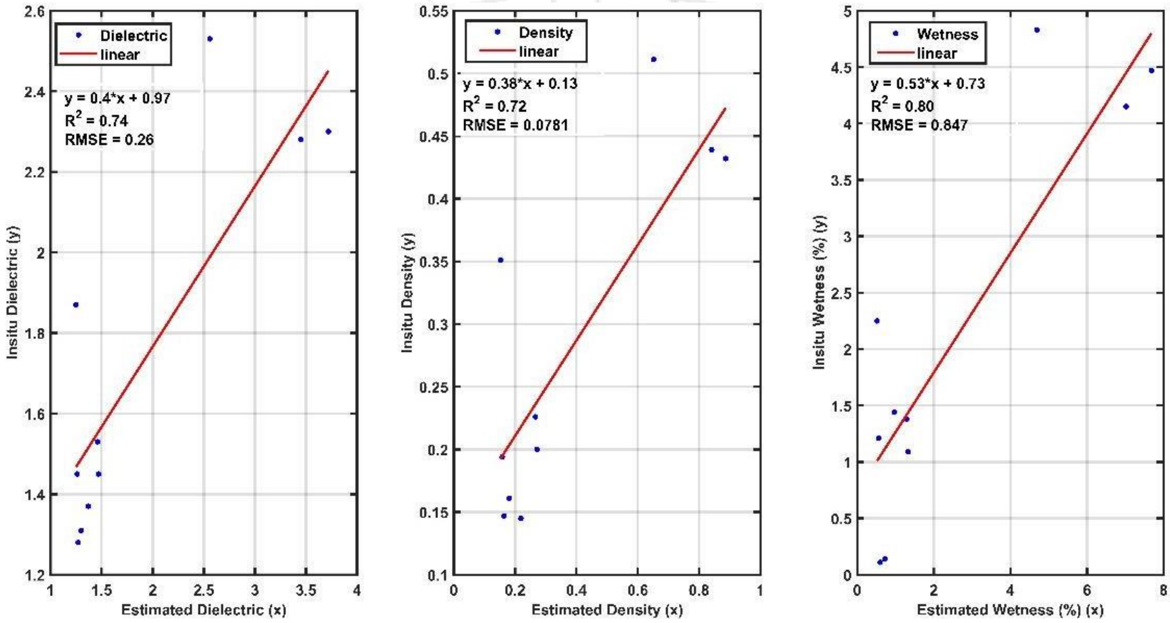

Figure 4.11: Showing the overall correlation between the estimated and in-situ values

So, it becomes necessary to perform additional tests to understand the assessment of the modeled and measured parameters. Due to the sample size (number of samples=11), a two-tailed t-test is used to compare the modeled and in-situ measured parameters to evaluate the suggested model's validity. The t-distribution value for the degree of freedom in the current case is 1.725 at the 0.05 (5%) significance level. Table 4.3 shows that every parameter's t-statistic (t-stat) is lower than this value, supporting the null hypothesis that the modeled and measured parameters are random samples from normal distributions with equal means and variance. It is also observed that the sample means of the modeled parameter are greater than the sample means of the observed parameters when the t-stat for snow dielectric, density, and wetness is positive.

The proposed model is compared with some existing models, shown in Table 4.4. The statistical parameters for linear fit, like R^2, RMSE, and Mean absolute error (MAE) of the proposed model, show improvement relative to the existing models. The advantage of this study is that the snow's physical properties can be estimated with freely available dual-pol Sentinel-1 data with significant accuracy.

Table 4.3: Results for the T-test for different snow geophysical parameters.

Test	H_0: h = 0	H_1: h = 1	Parameters	Dielectric	Density	LWC
t-test	The modeled and measured parameters were obtained from random samples drawn from normal distributions with equal means and unknown variances.	The modeled and the measured parameters come from populations with unequal means.	h p t-stats	0 0.4473 0.7752	0 0.2361 1.2215	0 0.5417 0.6208

Table 4.4: Performance evaluation of the proposed inversion models

Snow Properties	Proposed Model	Existing Model
Snow Dielectric	R^2 = 0.74, RMSE = 0.26, MAE = 0.4282	Varade et al., 2020: G4U effective: R^2=0.496, RMSE=0.063, MAE = 3.30
Snow Density	R^2 = 0.72, RMSE=0.08, MAE = 0.1688	Varade et al., 2020: G4U effective: R^2=0.485, RMSE=0.033, MAE= 7.51 Thakur et al., 2017 R^2 = 0.72
Snow Wetness	R^2 = 0.72, RMSE=0.85%, MAE = 1.2127%	Ma et al., 2020: R^2=0.72 RMSE=3.89%, MAE=3.35% (GaoFen3) andR^2=0.62, RMSE=1.66%, MAE=1.32%(Radarsat2) Thakur et al., 2017: R^2=0.74

However, it also has some limitations: the symmetry assumption for the proposed inversion model and the site location are also challenging because they require continuous trekking. The continuous monitoring of snow with electronic instruments is difficult as solar energy is minimal due to cloud cover most of the time. As this model also depends on the orientation angle of the scatterers, the satellite pass mode is also important. So, its efficiency should be tested for both ascending and descending passes. There are fewer in-situ measurements, which hinders the detailed analysis of the intermediate missing data values. Since the snow cover during the ablation period is shallow in this region, the model performance should also be tested for the winter season.

South Lhonak Glacier Region: To map snow geophysical parameters, it is important to map snow-covered pixels accurately. The NDSI (Eq. 4.15) threshold of 0.4 generally masks snow-covered areas. However, this also considers the glacial lake to be a snow-covered area. Based on the ability of the surface to reflect energy in the green and shortwave infrared (SWIR) bands, the NDSI is intended to differentiate between snow and non-snow areas. Nonetheless, glacial lakes frequently exhibit reflectance traits comparable to snow in these bands, especially if they are heavily turbid or glazed in ice. Because of this spectral similarity, NDSI couldn't segregate glacial lakes from snow cover. To mask the glacial lake from the NDSI-derived snow cover map, spectral unmixing is performed using the JHU snow spectral library. The resulting abundance fraction map shows the abundance of snow in each pixel in the range of (0 to 1). This study considered a threshold greater than or equal to 0.5 to be identified as snow-covered pixels.

In remote sensing imagery, natural surfaces generally comprise mixtures of multiple materials. Endmember extraction facilitates the identification of the most representative pure spectral signatures within a given scene, which may vary from those found in pre-existing spectral libraries. The endmembers derived from the snow pixels (Fig.4.12) are identified as coarse, medium, fine, and frost concerning the JHU snow grain size spectral library using a widely accepted and reliable SAM method (Singh et al., 2022).

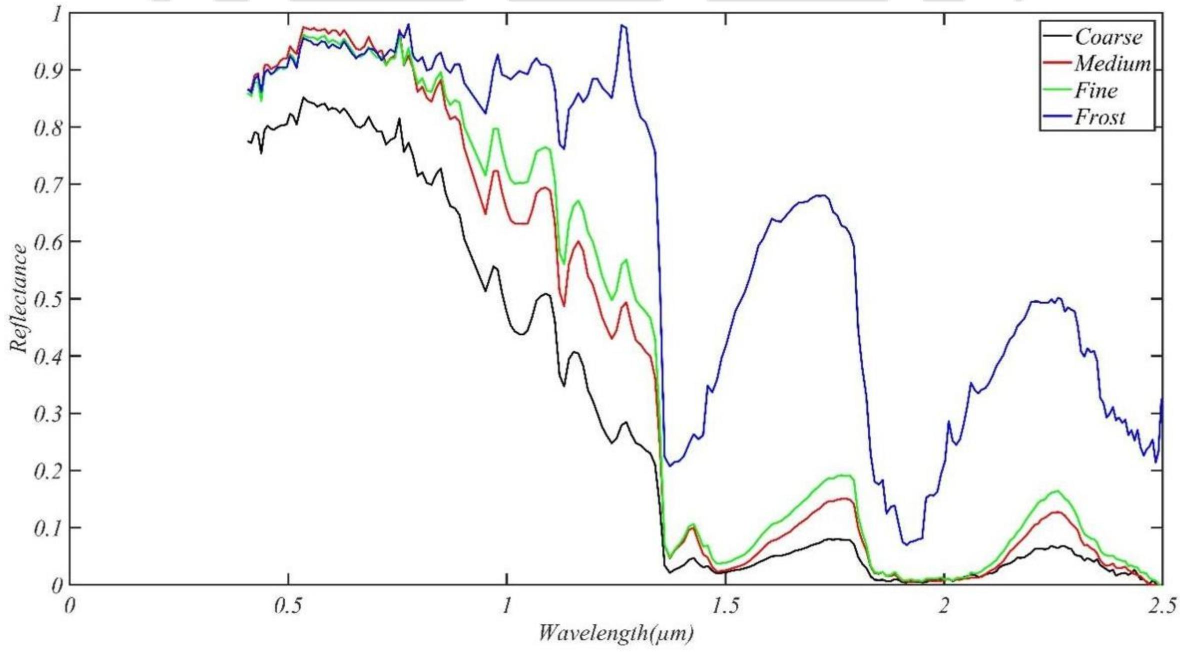

Figure 3.12: Endmembers of snow grain size derived from PRISMA Hypercube using FIPPI endmember algorithm.

SAM computes the angle in an n-dimensional space between two spectra and compares how similar they are. The similarity scores between the derived endmembers and the JHU snow library spectra are provided in Table 4.5. The derived endmembers map snow grain size using the SAM classification method. Fig. 4.13 represents the percentage of occurrence of each grain size mapped in the study area with the total snow cover area. The result indicates the dominance of coarse-grained snow in the region, which agrees with the ablation period condition of the Indian Himalayas (Singh et al., 2022).

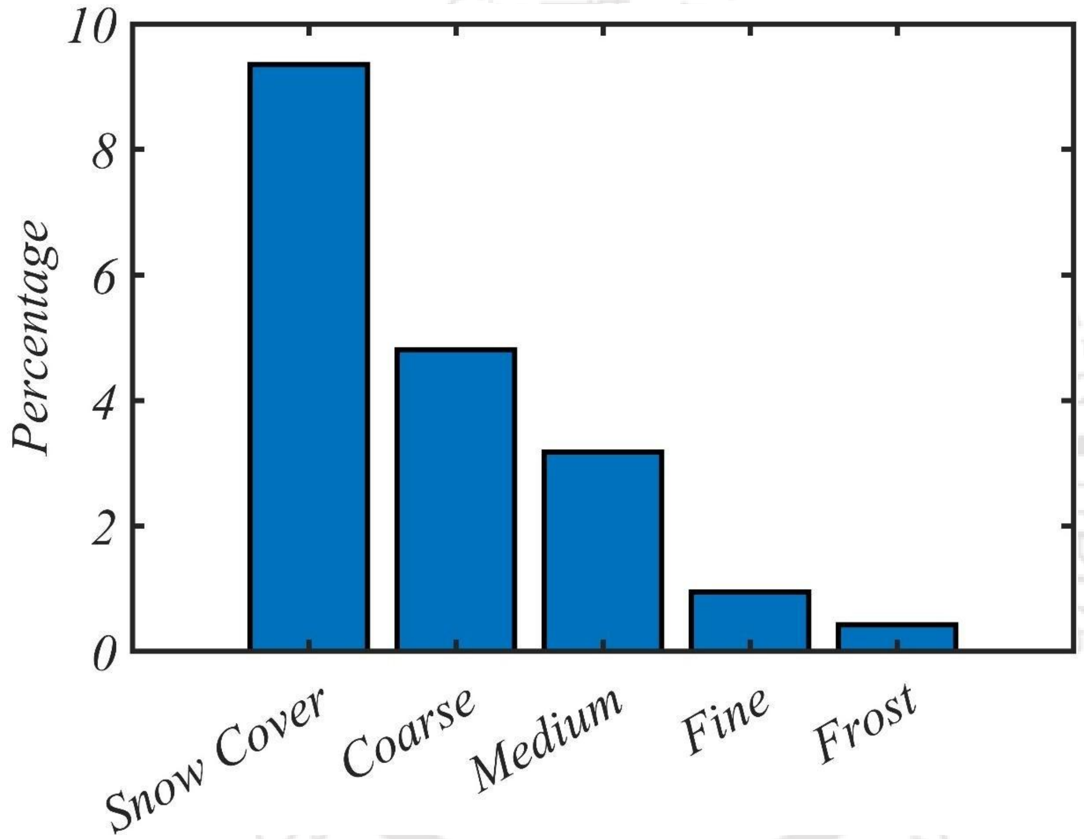

Figure 4.13: Percentage of occurrence of each grain size mapped in the study area.

Table 4.5: SAM similarity score between the JHU snow grain size and image-derived endmembers.

Sl No.	Snow Grain Type	Sam Similarity Score
01	Coarse	0.99
02	Medium	0.99
03	Fine	0.98
04	Frost	0.97

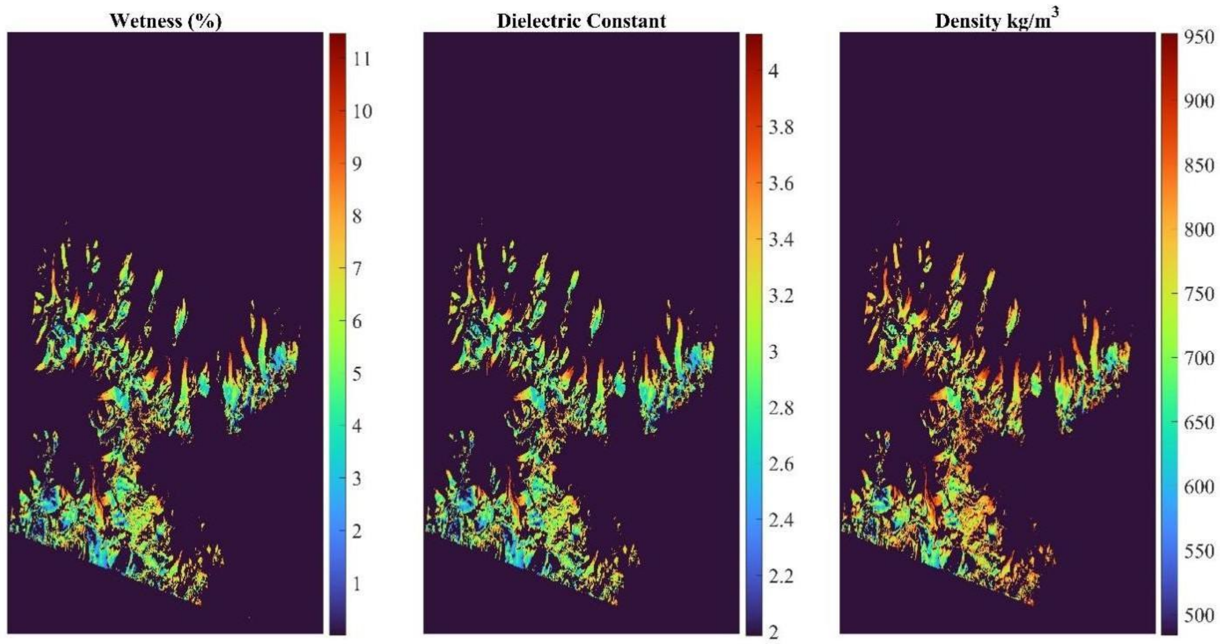

Figure 4.14: Snow wetness, dielectric constant, and density maps

The estimated snow wetness, dielectric, and wetness are represented in Fig.4.14 as maps. The wetness of each snow grain size agrees with the theory that the snow grain size increases with increasing water content. Through a process known as wet snow metamorphism, water functions as a lubricant, helping the snow grains bond and round. Grain clumps come together and form larger grains due to the capillary action produced by the liquid water. Additionally, this procedure promotes quicker melting and refreezing cycles, further enhancing grain growth. The firn density converted to glacial ice density equals 830-927 kg/m^3 (Cuffey et al., 2010). The proposed model can forecast the density of Indian Himalayan glaciers within the permissible range.

4.7. Conclusions

The study aimed to develop a state-of-the-art inversion model to estimate snow properties using the Sentinel-1 dataset. The proposed model uses VV and VH polarization to calculate the C2 matrix, providing stroke parameters. The Stokes parameters are represented as the combination of the T3 elements matrix using the general mapping of reflection symmetry. The inversion model is then formulated using elements of the T3 matrix, the Stokes parameter, the angle between the polarized signal with the symmetry axis of the scatterers, and the local incidence angles to calculate snow dielectric. The snow density is estimated using Looyenga's semi-empirical equation, while the snow wetness is determined using the formula given by Denoth. The following are the main conclusions of the study.

- A state-of-the-art inversion model has been developed using Sentinel-1 derived stokes parameters to estimate snow dielectric.
- It is evident from the estimated correlation coefficients that the modeled values of snow dielectric, density, and wetness corroborate well with the in-situ values (>0.7) with a 95 % confidence interval.
- The model can also predict the glacier density within specific ranges.
- The inversion model overestimates the geophysical properties of snow-cover regions with shallow snow depths.
- These snow physical parameters show relative improvement concerning some of the existing models.

The snow dielectric, density, and wetness model performed well for Western Sikkim, India. However, its efficacy should be tested using a wide range of in-situ datasets for broader utility.

The snow geophysical properties of snowpack of the South Lhonak glacial environment located in Sikkim, India has been estimated using PRISMA hypercube. The snow cover mask across the region is constructed at the subpixel level using the abundance fraction map and the widely used NDSI with a threshold of 0.4. For each grain size—coarse, medium, fine, and frost—the endmembers are obtained using a FIPPI. Subsequently, JHU snow grain size library spectra are used to characterize the image endmembers. The mapped snow grain size in the study region agrees with the ablation period condition of the Indian Himalayas. The proposed inversion model for snow wetness utilizes the NIR band (~1.03µm), which is also sensitive to snow grain size. In addition, it can estimate the glacial ice density well within the prescribed limit.

5

INVERSION MODEL FOR SNOW DEPTH

Assessing snow depth is crucial for various environmental, hydrological, and climatological studies. Snow depth measurement utilizing conventional techniques often encounters challenges in high-altitude remote locations. In this scenario, space-borne satellite remote sensing has proven to be a scientific tool to predict snow depth. With the availability of Sentinel-1, a C-band Synthetic Aperture Radar (SAR) data, snow depth estimation is being widely studied. This study introduces an improved snow depth inversion model utilizing the Differential Interferometric Synthetic Aperture Radar (DInSAR) technique in conjunction with Landsat-9. The Landsat-9 BOA dataset estimates the snow wetness and the snow cover map. Snow's physical properties, wetness, dielectric, and density are interrelated. The corresponding state-of-the-art empirical equations are utilized to predict snow dielectric, an essential input for the snow depth inversion model.

5.1. Introduction

The presence of snow cover is integral to upholding the ecological equilibrium within a given region. Its functions extend to temperature regulation, shaping climate patterns, and serving as a habitat for diverse plant and animal species. Beyond its ecological significance, snow is pivotal in governing the global water cycle and the freshwater flow rate. Moreover, it contributes significantly to regulating the Earth's overall temperature. Climate change and variations in snow cover are closely associated (Ulaby et al., 1977; Thakur et al., 2013). Consequently, snow is a significant component of global climate modeling and weather prediction. Snow depth is a critical parameter for understanding the extent and volume of snowpack, which plays a key role in hydrological studies (Singh et al., 2008). It is an essential indicator for assessing snow water equivalent (SWE). It provides valuable insights for water resource management, snowmelt forecasting, and various hydrological applications (Patil et al., 2020; Awasthi et al., 2020). However, conducting in-situ measurements to obtain such crucial parameters poses challenges, especially in mountainous regions like the Himalayas, owing to adverse weather conditions and limitations in human resources, logistics, and infrastructure (Varade and Dikshit, 2019; Varade et al., 2020; Varade and Dikshit, 2020). Under these circumstances, monitoring snow conditions has proven to be especially useful using satellite remote sensing techniques (Lenormand et al., 2002; Rees, 2005; Lei and Siqueira, 2015). The snow parameters have previously been retrieved by researchers employing a variety of optical and radar remote-sensing datasets (Dozier and Painter, 2004; Landes et al., 2007; Du et al., 2010). Optical remote sensing encounters constraints in foggy conditions, prevalent in snow-covered regions for much of the year. In contrast, radar remote sensing, functioning within the microwave spectrum's P, L, C, and X frequency bands, offers an advantage by acquiring images even under cloud cover.

Satellites equipped with Synthetic Aperture Radar (SAR) technology can acquire intricate image datasets at high resolution, with excellent temporal accessibility day and night, and achieve resolutions of up to a meter scale (Zink et al., 2006). Snow monitoring and parameter extraction have long benefited from the use of SAR. SAR Polarimetry (Pol-SAR) and SAR interferometry (InSAR)-based access has proven to help estimate snow physical parameters such as snow depth (Mahmoodzada et al., 2020), snow density (Varade et al., 2019), and snow water content (SWC) (Patil et al., 2020). Lievens et al. (2019) used time series Sentinel-1 records to study the inconstancy of snow depth in the mountains of the Northern Hemisphere. Patil et al., 2020 retrieved snow depth (SD) and snow water equivalent (SWE) using the link between particle anisotropy, snow depth, and the co-polar phase difference (CPD). The co-polar channels are typically provided by commercial polarimetric SAR data, which are expensive. In contrast, sensors like Sentinel-1, one co-polar, and one cross-polar channel (VV and VH) are freely available.

On the other hand, to understand surface dynamics, especially surface subsidence, interferometric methods that make use of spaceborne SAR have been thoroughly studied in the scientific literature (Sánchez and Navarro, 2017; Strozzi et al., 2018; Yu et al., 2018). Repeat-pass interferometric datasets and approaches entrenched in InSAR have been extensively employed for the calculation of snow water equivalent and the analysis of snowpack dynamics (Evans and Kruse, 2014; Lei and Siqueira, 2015; Leinss et al., 2015; Li et al., 2017; Varade et al., 2020). However, InSAR signals are mixed with the topographic phase (Principles, I., 2007). The Differential Interferometric Synthetic Aperture Radar (henceforth DInSAR) technique is used to solve this problem. This technique is considered more accurate than InSAR as it can provide relative measures up to a few centimeters or less (Danklmayer et al., 2009). Using interferometric phase information, the DInSAR path has been exploited to project the snow water equivalent for dry snow (Guneriussen et al., 2001). They utilized C-band interferometric SAR (InSAR) records from the European Remote Sensing Satellite (ERS-1/2). Subsequent research utilizing Sentinel-1 (C-band) datasets has focused on estimating snow depth through

DInSAR (Varade et al., 2020). The snow depth findings obtained indicate an enhancement in overall accuracy compared to conventional InSAR techniques (Liu et al., 2017; Varade et al., 2020). Awasthi et al. (2021) proposed a snow-depth inversion model using Polarimetric SAR Interferometry (PolInSAR) using TerraSAR-X/TanDEM-X datasets with a temporal baseline of 10 seconds. Their work focused on the Manali region of Himachal Pradesh, India, for the dates 21 January 2015 and 22 January 2015. The modeled snow depths for the corresponding period were observed to be 0.84 m to 1.24 m. The retrieved snow depth results were validated against ground-based measurements obtained from the Automatic Weather Station (AWS) operated by the Snow and Avalanche Study Establishment (SASE), Defence Research and Development Organization (DRDO), and the Indian Institute of Remote Sensing (IIRS) located in the Dhundi region of the study area for the corresponding dates.

Liu et al. (2017) highlight a novel scheme combining Sentinel-1 D-InSAR and the 3DVAR fusion algorithm to enhance snow depth estimation. Application in the Bayanbulak Basin demonstrates increased R^2 values and reduced RMSE, confirming the scheme's effectiveness. This approach offers a reliable regional snow depth estimation method, benefiting agriculture, hydrology, and climate studies. Li et al. (2022) proposed a snow depth inversion algorithm designed explicitly for forested regions by introducing a forest phase to account for the effects of forest cover on microwave backscattering. To estimate snow depth, this method utilizes DInSAR interferograms and distinct phase models for forested and non-forested areas. The algorithm was applied to the Jiagedaqi area in the Greater Xing'an Mountains, generating a snow depth map at a spatial resolution of 30 m on 7 December 2020. Estimated snow depths ranged from 40 to 120 cm, which strongly agreed with the reference data. Including the forest phase improved the average snow depth estimation in forested areas by 5.98 cm, reducing underestimation and enhancing overall accuracy. Torun and Ekercin (2021) estimate that snow density, depth, and snow water equivalents are equivalent using single-polarization TerraSAR-X data over Mount Erciyes, Turkey. Kriging and ISO-4355 methods were integrated with D-InSAR models to estimate snow parameters. Snow depth, volume, and water equivalent maps were produced, revealing variations based on the snow density calculation methods. The results, supported by in situ measurements, showed consistency and accuracy in estimating snow parameters using single-polarization data. Yang and Li (2021) investigated snow depth data from multiple sources, including automatic ultrasonic snow depth detectors, manual measurements, and high-precision, multi-angle, all-weather snow depth inversion using Sentinel-1 synthetic aperture radar. They employed D-InSAR technology to analyze relative phase information from Sentinel-1A SLC interferometric image pairs. This process involved phase unwrapping, removal of non-snow-related phase components, and subsequent conversion of snow-related phase data into snow depth measurements.

The snow depth inversion model is a function of the snow dielectric constant, radar wavelength, and incidence angle/local incidence angle, as mentioned in prior research (Guneriussen et al., 2001; Rott, Nagler, and Scheiber, 2003; Li et al., 2017; Varade et al., 2020). Studies also conclude that snow depth estimation largely relies on the accuracy of two components (i.e., snow phase contribution and snow dielectric constant). These two components can be determined through in-situ data or other remote sensing data sources such as multispectral data (Varade and Dikshit 2017, 2018, 2019) or full polarimetric SAR data (Singh et al., 2017). Varade et al. (2020) used a multispectral data (Landsat-8) based snow cover map threshold for snow phase correction. However, a snow mask derived from Landsat images is frequently used to extract the Sentinel-1 backscattering (Thakur et al., 2017; Nagler et al., 2016; Crawford, 2015). So, in this study, we employed Landsat-9-based snow cover product and snow geophysical parameters (wetness, density, and dielectric) for snow depth estimation. In this research, Sentinel-1 (C-band) datasets, supplementary data derived from in- situ measurements, and enhanced versions of optical datasets, such as Landsat 9, have been used to construct a snow depth inversion model. A state-of-the-art snow depth inversion model has been proposed by integrating information from Landsat 9 Level 2 data and Sentinel-1 data, focusing on a study area in Arunachal Pradesh, India, within the Eastern Himalaya region.

5.2. Study Area

The research area, depicted in Figure 5.1, encompasses Mechukha, situated within the Siang basin of Arunachal Pradesh. This region exhibits a varied topography, with elevations ranging from the district capital at 1,829 meters to the highest point reaching 5,248 meters. Positioned approximately at 93°58'26.4" E longitude and 28°43'8.4" N latitude, the central coordinates mark the focal point of the study area. Snow coverage within this locale peaks during March and April before undergoing ablation. The field site (Figure 5.2) features a diverse landscape, including subtropical pine forests, subalpine, and alpine forests.

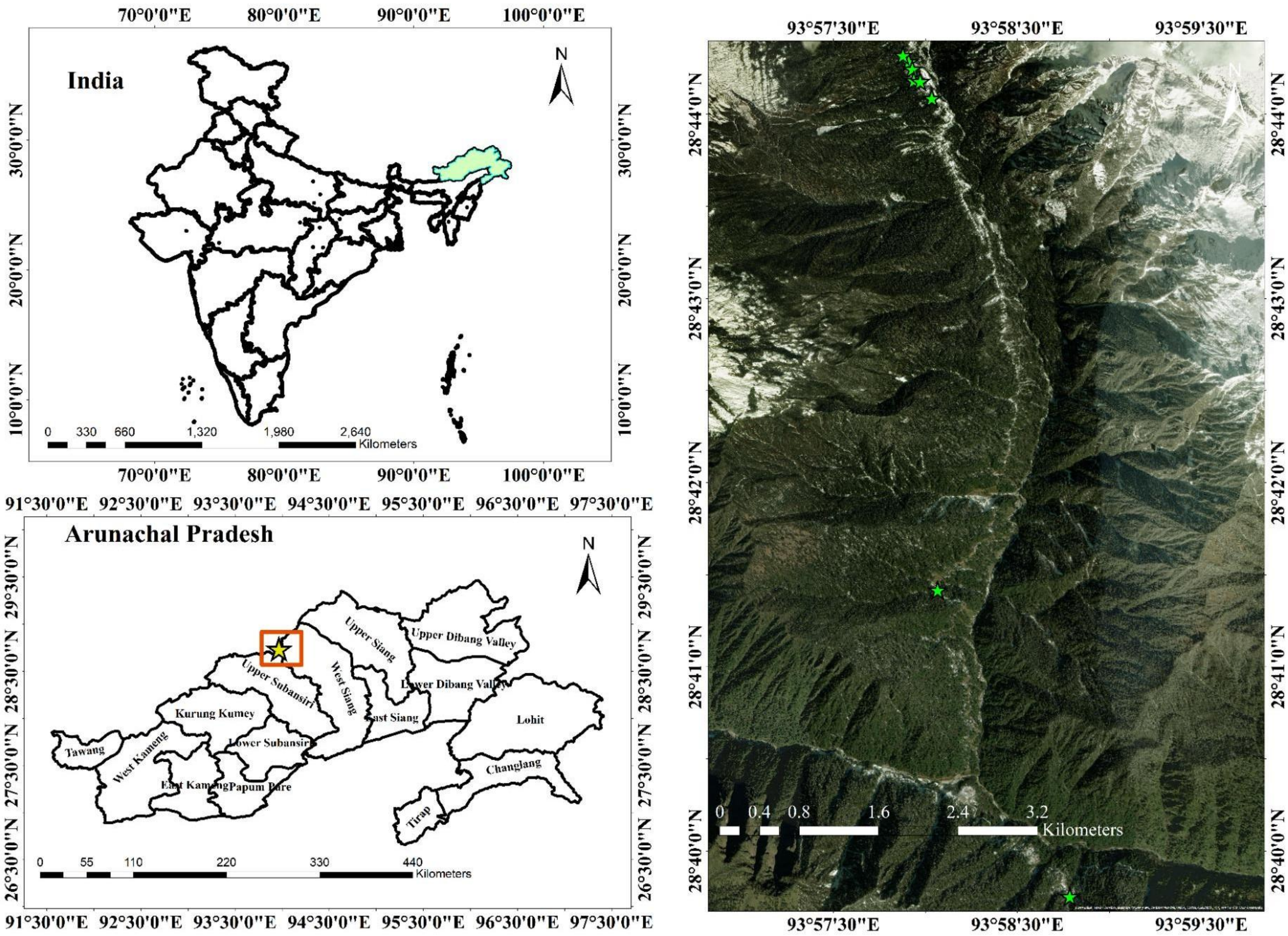

Figure 5.1. Map indicating the study area and the locations of in-situ measurements.

Figure 5.2. Snow Cover in the study area on 14th March 2022

5.3. Dataset

5.3.1. In-situ Data

On March 14, 2022, a field expedition was carried out in the Mechuka Valley in the West Siang district of Arunachal Pradesh, India. Within this research endeavor, we assessed snow depth across elevation intervals spanning from 2380 meters to 3550 meters. A total of 8 measurement sites were established to gauge snow depth, with observed values ranging from 3 to 50 cm (Table 5.1).

Table 5.1: In-situ information of snow depth corresponding to the geographic locations

SL No.	Latitude	Longitude	Snow Depth (cm)
01	28°41'25.03"N	93°58'3.97"E	20
02	28°39'45.12"N	93°58'47.07"E	3
03	28°44'17.15"N	93°57'54.55"E	31
04	28°44'19.23"N	93°57'52.67"E	25
05	28°44'14.81"N	93°57'55.69"E	33
06	28°44'11.07"N	93°57'56.19"E	40
07	28°44'10.72"N	93°57'58.26"E	50
08	28°44'5.28"N	93°58'2.07"E	50

5.3.2. Optical Data (Multispectral)

On September 27, 2021, the U.S. Geological Survey (USGS) and the National Aeronautics and Space Administration (NASA) successfully launched Landsat-9 (L-9) as part of the Landsat program. Onboard this satellite are two key scientific instruments: The Thermal Infrared Sensor 2 (TIRS-2) and the Operational Land Imager 2 (OLI-2). Except for the panchromatic band, which boasts a spatial resolution of 15 meters, OLI-2 captures data across nine spectral bands at a spatial resolution of 30 meters. Meanwhile, TIRS-2 records data across two spectral bands at a spatial resolution of 100 meters. This study utilized an L-9 level 2 product, offering bottom-of-the-atmosphere (BOA) reflectance. To ensure optimal integration of SAR and optical data, images from both sensors must be acquired as closely as possible regarding date and time. Therefore, images captured on March 14, 2022, were selected for this study, coinciding with the field investigation.

5.3.3. Synthetic Aperture Radar (SAR)

Sentinel-1, part of the European Copernicus Program, comprises two satellites launched by the European Space Agency (ESA). April 2014 marked the launch of Sentinel-1A and April 2016 of Sentinel-1B, respectively. On March 14, 2022, Sentinel-1A acquired data with a descending pass, aligning with the date of field measurements. A reference image with little to no snow cover in the research location was chosen on September 3, 2021, to match the pathway and aspect of the scene covered in snow. The level-1 SLC product of the dual-polarimetric (VV/VH) Interferometric Wide (IW) swath mode C-band SAR dataset from Sentinel-1A was used in this investigation.

Table 5.2. This study's Sentinel-1 dual polarimetric IW mode pairings and their temporal baseline

S. No.	Snow Covered Scene	Snow Free Scene	Temporal Baseline
01.	S1A_IW_SLC _1SDV_20220314T234622_20220314T234649_042324_050B9B_C585	S1A_IW_SLC_ 1SDV_20210903T234625_20210903T234652_039524_04ABBB_D87D	192 days

5.4. Methodology

The pre-processing and temporal alignment of Sentinel-1 and Landsat-9 datasets acquired on 14 March 2022 are essential for their effective and synergistic utilization, facilitating accurate and reliable analyses. In other words, proper pre-processing and co-acquired datasets enable the synergistic integration of Sentinel-1 and Landsat-9, ensuring precise pixel alignment, minimizing interpolation errors during collocation, and improving the reliability of integrated datasets for geospatial and environmental analyses.

So, the pre-processing required for the radar dataset is shown in Fig.5.3 and explained in the subsequent subsection 5.4.1 DInSAR processing, while pre-processing of L-9, Level-1 (top-of-the-atmosphere reflectance: TOA) data to obtain Level-2 (bottom-of-the-atmosphere: BOA) data is obtained using an atmospheric correction module called Sensor Independent Atmospheric Correction (SIAC) developed for Landsat-8. This step is important because BOA data is required to estimate intrinsic parameters such as soil moisture/ snow wetness. Subsection 5.4.2. should explain the necessary pre-processing and snow parameters estimation methodology in detail. After the collocation of processed S-1 SLC product and L-9, Level-2 data, the snow depth inversion formulation will be explained in subsection 5.4.3

5.4.1. DInSAR Processing

The DInSAR is a technique used to generate an interferogram with the topographic contribution removed. The two-pass DInSAR method requires two Synthetic Aperture Radar (SAR) images captured at different times over the same area (Table 5.2). In this study, differential phase information in the VV and VH polarimetric channels is obtained by applying DInSAR processing to bi-temporal dual-polarimetric Sentinel-1 Single Look Complex (SLC) images, using the SNAP software. The master and slave images correspond to periods without snow or snow cover, respectively. A reference image with minimal or no snow cover is selected, and the MODIS 8-day composite monthly average snow cover product is used to determine the month with the least snow cover in the study area. The snow hydrological year, defined as October to September from 2000 to 2023, shows the lowest snow cover in September. Consequently, a temporal baseline of 192 days was selected, ensuring the snow-free image corresponds to minimal snow cover in the region. For the Coregistration of both the master and slave datasets, the SRTM DEM 1 arcsec is employed. Cubic convolution resampling is applied to the DEM. Followed by the formation of an Interferogram, further deburst command and, the Enhanced Spectral Diversity (ESD) is applied to improve the accuracy of phase unwrapping. The interferogram is generated by subtracting the flat-earth phase, a process known as interferogram flattening. The interferometric phase consists of two components: one due to altitude variation and the other due to slant range displacement between scatterers within a pixel. Interferogram flattening eliminates the phase contribution from slant range displacement, leaving the residual phase proportional to the relative terrain altitude. Further, an SRTM DEM 1 arcsec has been taken as an external DEM to simulate and remove phase changes due to topography using the SNAP toolbox (Topographic Phase Removal). A new phase image is formed, which consists of surface change phase contribution, which is assumed due to snow accumulation. The unwrapping of the filtered interferometric phase was performed using the SNAPHU module in a Windows environment. SNAPHU, developed by Chen and Zebker (2002), utilizes a statistical-cost, network-flow algorithm for phase unwrapping. Following unwrapping, the phase data were geometrically corrected using range Doppler terrain correction, as described by Hellwich and Ebner (2000). The necessary steps taken for DInSAR processing are mentioned in Fig.5.3.

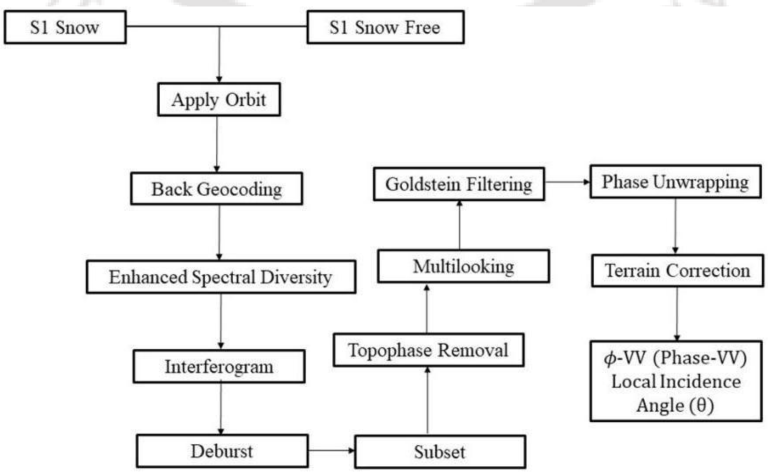

Figure 5.3: DInSAR processing in SNAP. Similar steps followed for VH-Channel steps.

5.4.2. Optical Data processing (multispectral)

The L-9 data obtained from USGS Earth Explorer from March 14, 2022, is at level 1, providing top-of-the-atmosphere reflectance (TOA). However, a level-2 product offering bottom-of-the-atmosphere (BOA) data is required to estimate intrinsic parameters such as soil moisture/ snow wetness. Hence, the Sensor Independent Atmospheric Correction (SIAC) technique developed for Landsat-8 was applied to the L-9 level-1 data in the Google Earth Engine to derive L-9 level-2 data. The assessment of soil moisture has frequently employed trapezoidal or triangular feature spaces based on land surface temperature (LST), near-infrared (NIR) reflectance, and the normalized difference vegetation index (NDVI) (Sadeghi et al., 2017). Similarly, the near-surface snowpack response can be analyzed using spectral data from the visible and infrared bands within an integrated framework for monitoring the liquid water content (LWC) in snowpacks. This approach leverages the physical interaction between light and snow, where snow properties such as grain size and liquid water content influence spectral reflectance in the electromagnetic spectrum's visible and near-infrared (NIR) regions. Wet snow exhibits significantly lower spectral reflectance in these regions than dry snow due to increased absorption of incident light caused by higher liquid water content. In this study, the NDSI-Near Infrared (NIR- band 5) feature space was generated in MATLAB using the L-9 Level-2 dataset, from which snow wetness was estimated based on the empirical relationship (Eq. 5.2) outlined by Varade and Dikshit (2020). Pixels with lower LWC are located near the dry edge of the scatter distribution in the NIR-NDSI feature space, while pixels with higher LWC are closer to the wet edge. Within this feature space, dry snow pixels are concentrated in the upper right corner, whereas wet snow pixels are positioned in the lower right corner. Subsequently, snow dielectric properties were derived using established empirical relations with snow wetness as described by Tiuri et al. (1984), Denoth (1994), and Kendra et al. (1994), as shown in Equations 5.3-5.6. Thus, the parameters such as snow wetness and dielectric in this investigation were obtained using the approaches described in Chapter 4 (section 4.5), adapted for the L-9 Level-2 dataset.

$$\mathrm{NDSI} = \frac{\mathrm{Green}-\mathrm{SWIR}}{\mathrm{Green}+\mathrm{SWIR}} \ldots\ldots (5.1)$$

$$w = \frac{i_d+(s_d*\mathrm{NDSI})-\mathrm{NIR}}{(i_d-i_w)+(s_d-s_w)*\mathrm{NDSI}} \ldots\ldots (5.2)$$

Where, i_d, i_w, s_d, s_w are the intercept and slope of the dry and wet edges.

$$\varepsilon_s = \varepsilon_{ds} + \Delta\varepsilon_{ws} \ldots\ldots (5.3)$$

$$\varepsilon_{ds} = 1 + 1.7\rho_{ds} + 0.7\rho_{ds}^2 \ldots\ldots (5.4)$$

$$\Delta\varepsilon_{ws} = 0.187w + 0.0045w^2,\ \Delta\varepsilon_{ws} = 0.089w + 0.72w^2,\ \Delta\varepsilon_{ws} = 0.206w + 0.0046w^2 (5.5)$$

$$w = 5.35[\varepsilon_s - (1 + 1.92\rho_{ds})] \ldots\ldots (5.6)$$

5.4.3. Snow Depth Inversion Model

The processed SAR, level-2, and multispectral L-9, level-2 data were merged using the bilinear interpolation resampling method within the collocation toolbox of the Sentinel Applications Platform (SNAP) to utilize radar and optical data synergistically. The collocated dataset is then imported into MATLAB for the snow wetness and dielectric depth inversion modeling. As outlined in the introduction and supported by the literature review, the snow depth inversion model is influenced by the snow dielectric constant, radar wavelength, and incidence angle or local incidence angle. The detailed methodology for snow dielectric estimation is mentioned in the previous subsection. The snow depth inversion model is shown in Eq. 5.7 (Rott, Nagler, and Scheiber, 2003; Varade et al., 2020). From Eq. 5.7 it can be seen that the core inputs for the proposed inversion model include phase information from VV and VH channels, local incidence angle, and snow dielectric. The overall methodology corresponding to Eq.5.7 is shown in Fig.5.4

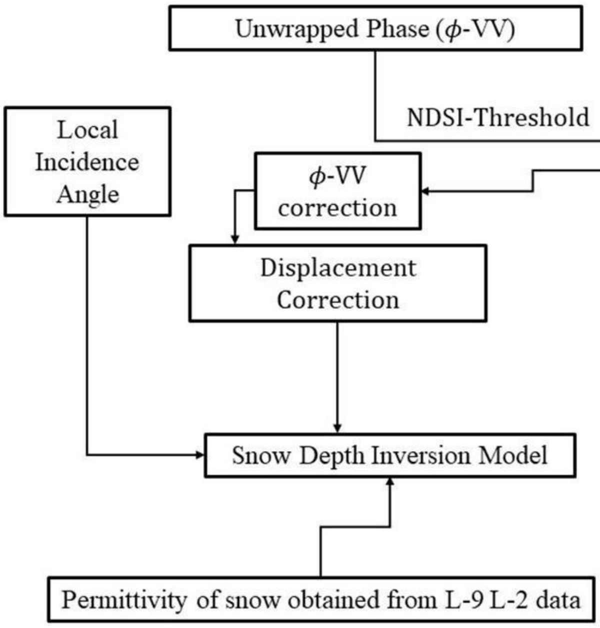

Figure 5.4: Snow Depth Inversion Model Overall Methodology. Similar steps were followed for the VH-Channel.

Previous investigations have shown a stronger connection between polarimetric phase changes in the co-polarized bands and snow depth. Further, the snow depth inversion model has been modified with an extra snow phase correction for both the VV and VH (Varade et al., 2020) and a common scaling factor for both channels has been implemented. This approach is particularly significant in addressing snowpack heterogeneity and the varying snow properties—such as snow dielectric, liquid water content, and roughness—that influence radar backscatter in each channel (Chapter 6). Although not a universally standard practice, separate scaling factors represent a valid and innovative methodology that enhances model accuracy. It serves as a refined technique to improve the physical realism and sensitivity of the inversion model. Accordingly, this study introduces separate scaling factors for VV and VH channels

(Eq.5.8), enabling a more precise representation of their contributions and thereby enhancing the accuracy and robustness of the snow depth inversion model.

$$\boldsymbol{\phi} = \frac{4\pi}{\lambda} d_s \left(\cos(\theta) - \sqrt{\varepsilon - (\sin(\theta))^2}\right) \ldots\ldots\ldots\ldots\ldots (5.7)$$

$$d_{\mathrm{corrected}} = (\mathrm{Weight} * \alpha_{vv} * d_{vv_{\boldsymbol{w}orre\boldsymbol{w}ted}} + (1 - \mathrm{Weight}) * \alpha_{vh} * d_{vh_{\boldsymbol{w}orre\boldsymbol{w}ted}}) \ldots (5.8)$$

$$\mathrm{Weight} = \frac{(\max(\theta) - (\theta))}{\max(\theta) - \min(\theta)} \ldots\ldots\ldots\ldots\ldots\ldots (5.9)$$

Where θ is the local incidence angle, ε is snow permittivity, d_s is the snow depth and $\boldsymbol{\phi}$ is terrain corrected for the unwrapped phase in the VV/VH channel.

Several studies have shown that complex terrain can lead to reduced radar coherence and weakened backscatter, which in turn hampers accurate snow depth retrieval (Liu et al., 2017; Guneriussen et al., 2001). The weight function plays a crucial role in quantifying the contributions of various scattering mechanisms to the overall backscatter signal, and adapting it to local topographic and snow conditions can improve model accuracy. Refining the weight function in snow depth inversion models, especially in regions with complex topography like the Indian Himalayas. The rationale behind this refinement lies in the observed sensitivity of radar backscattering to local topographic variations and changes in snow properties (Chapter 6), which can significantly affect the accuracy of snow depth estimation. The need for refining the weight function is further justified by the variation in radar coherence, which is more stable in snow-free regions than snow-covered ones (Deeb, Forster, and Kane, 2011). This suggests that the weight function should be adjusted for higher scattering variability in snow-covered regions (Eq.5.9)

5.5. Results and Discussion

5.5.1. Snow Cover Threshold

The generation of the snow cover map commonly utilizes NDSI methods (Wang et al., 2018), where a threshold NDSI value of 0.4 is employed to categorize between cloud cover and snow cover. In this investigation, the NDSI method is obtained using L-9 level-2 data. Eight in-situ assessments were conducted in the study area to assess snow depth, ranging from 3cm to 50 cm, predominantly within the Alpine forests of the study area. Typically, NDSI values ranging from 0 to 0.4 indicate contaminated or mixed-state snow, while values greater than 0.4 denote pure snow (0.7-1) or snow with minimal contamination. NDSI values may be overestimated or underestimated in forested regions (Dietz et al., 2012). Field investigations revealed the presence of Alpine forests in certain parts of the study area (Fig. 5.2). Under such conditions, the NDSI threshold must be reduced to mitigate underestimation, provided the scene subset is free of cloud cover. Snow-covered areas are identified as pixels with NDSI values below 0.4, provided the Normalized Difference Vegetation Index (NDVI) is approximately 0.1 (Hall et al., 2002). Furthermore, factors such as illumination angle and the degree of contamination can also influence the threshold (Varade and Dikshit, 2018). As the in-situ measurements are within vegetated areas and the image pixel size is 10m (resampled from 30m to 10m), the average NDSI values within such pixels may degrade, as depicted in Figure 5.5. Notably, locations with snow depths of 3cm and 20 cm exhibit NDSI values below 0, while NDVI values (higher values indicating vegetation presence) surpass 0.7. Consequently, the Normalised Difference Forest Index (NDFSI) is utilized to identify snow presence in forested regions, although its value remains below 0.4. According to Saptarshi et al. (2022), NDFSI values exceeding 0.4 indicate snow. The degradation of NDSI and NDFSI values in such locations is attributed to elevated NDVI values. NDSI values span from 0.17 to 0.48 for the rest of the six in-situ snow depth locations, and NDVI values range from 0.19 to 0.37, indicating the presence of short herbs and shrubs. Corresponding NDFSI values for these snow depth locations range from 0.25 to 0.54. Thus, based on field observations and the scene free from cloud, NDSI values greater than 0 are treated as snow-covered pixels.

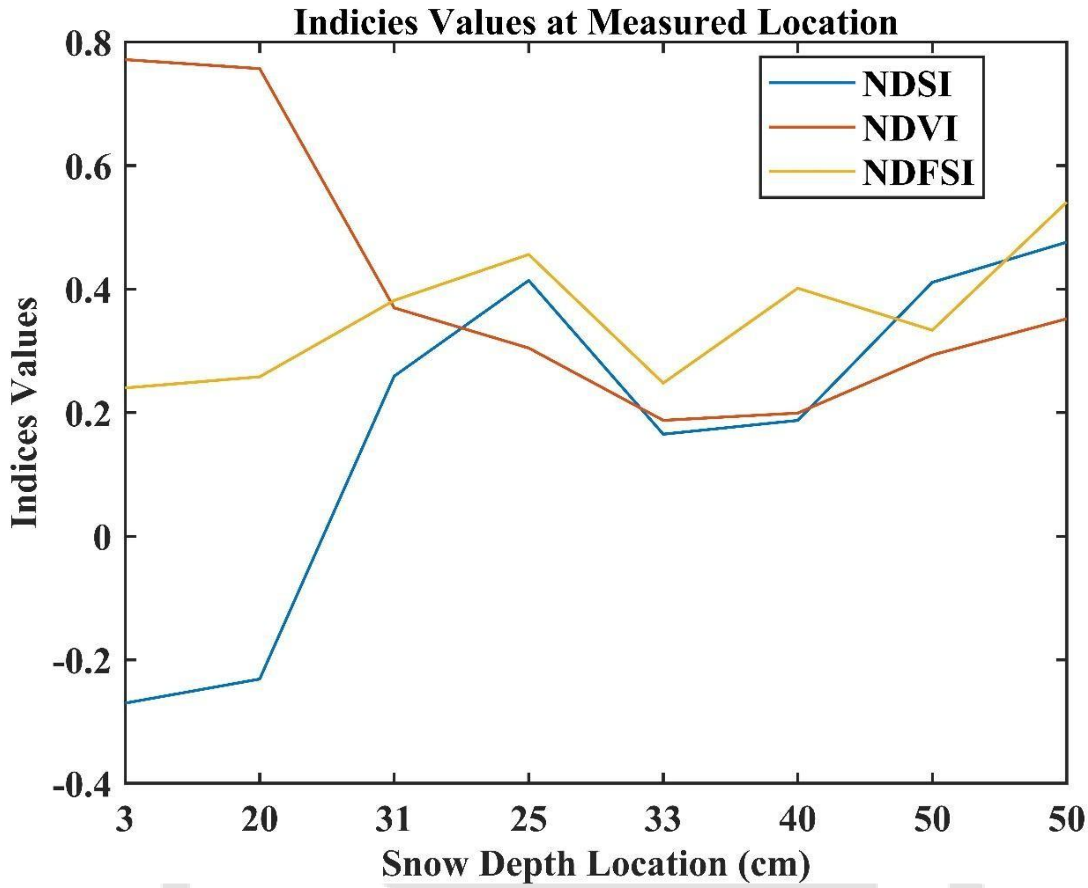

Figure 5.5: In-situ points for snow depth measurement. The y-axis shows the index values of NDSI, NDVI, and NDFSI.

5.5.2. Important Consideration for Snow Depth Inversion Model

The DInSAR technique, typically utilized to image ground surface changes due to various causes, is presumed in this study to indicate snow accumulation-induced alterations primarily. The consistency of the scattering qualities between the master and slave images (snow-covered and snow-free) is assessed using coherence products produced using InSAR techniques. Coherence scores indicate whether there is any association at all between the images, with values ranging from 0 to 1. Notably, observed coherence values for snow-covered and snow-free areas are relatively similar, with low coherence values suggesting limited similarity between the selected image pairs. Coherence is heavily influenced by temporal baselines, deteriorating as the span between master and slave images escalation (Varade et al., 2020). The low coherence can be attributed to temporal decorrelation arising from the extended temporal baseline of 192 days. Factors such as snow metamorphism, changes in surface roughness, or environmental influences, including vegetation growth, may further contribute to the degradation of coherence over time. It is acknowledged that coherence degradation is unavoidable with extended temporal baselines, particularly in regions characterized by dynamic environmental changes. Based on prior studies (Varade et al., 2020), correction factors have been incorporated into the snow depth inversion model, attributed to adjustments in the weight function and scaling factors, as discussed in the methodology section.

The weight function depends on the local incidence angle (LIA) (Eq. 5.9), a crucial attribute in snow depth estimation using the DInSAR technique. Selecting incidence angles that are less susceptible to geometric errors is recommended to enhance snow depth estimation accuracy. Studies by Nagler et al. (2016) indicate that geometric error effects are more pronounced at lower incidence angles down 15° and higher angles above 75°. However, the preferred range of local incidence angles is determined based on those following a distribution resembling the normal distribution (Nagler et al., 2016; Varade et al., 2020). Figure 5.6 shows the normal probability plot and histogram of the local incidence angle used in this investigation.

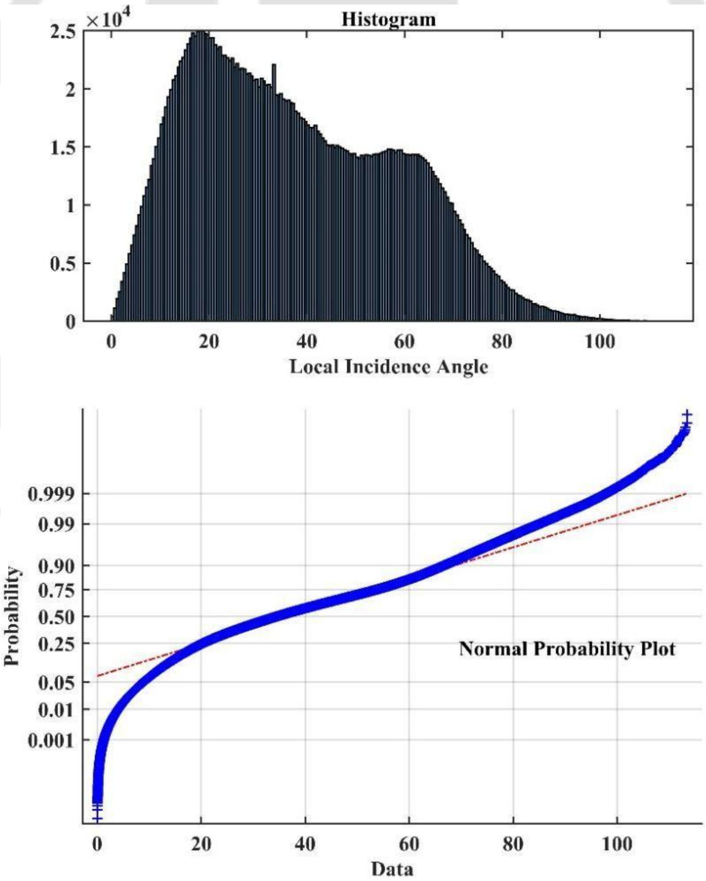

Figure 5.6: Histogram and normal probability plot of local incidence angle.

With a standard deviation of 20.60°, the local incidence angle's overall average and median values are determined to be 37.45° and 34.45°, respectively. The normal probability plot depicted in Figure 5.6 indicates that local incidence angles in the space of 20° to 60° follow a distribution analogous to the normal distribution, whilst significant deviation is observed below 20° and above 60°. Varade et al. (2020) have selected a weight function explicitly controlled by thresholds, as shown in the normal probability plot of LIA in Figure 5.6. Their method explicitly targets a specific range of incidence angles, which might be optimal for particular study regions. However, the proposed weight function (Eq.5.9) has more straightforward assumptions and general applicability. It provides linearly decreasing weights as the local incidence angle increases, prioritizing signals from smaller angles with better strength and reduced distortions. In other words, a smaller Local Incidence Angle (LIA), closer to the nadir or perpendicular to the surface, will be assigned a higher weight. In contrast, a larger LIA, approaching grazing incidence, will receive a lower weight. The proposed weight function accounts for SAR signals at smaller incidence angles having better signal strength and reduced geometric distortions, leading to more reliable snow depth retrieval. Following the suitable weight function for the snow depth inversion model, the next step is to acquire snow permittivity, which is mentioned in the methodology section.

The mean, median, and standard deviation of snow wetness obtained in the study area are 5.30 %, 5.86 %, and 2.63 %, respectively. Based on the average snow wetness values, it can be inferred that the snow is in wet conditions (wetness > 1% indicates wet snow). The corresponding snow permittivity is determined using the methods outlined in the methodology section, illustrated in Figure 5.7. Since in-situ measurements of snow physical properties (snow wetness, dielectric constant, and wetness) were not conducted during the field investigation, the snow permittivity derived from the multispectral data is utilized as input for the snow depth inversion model.

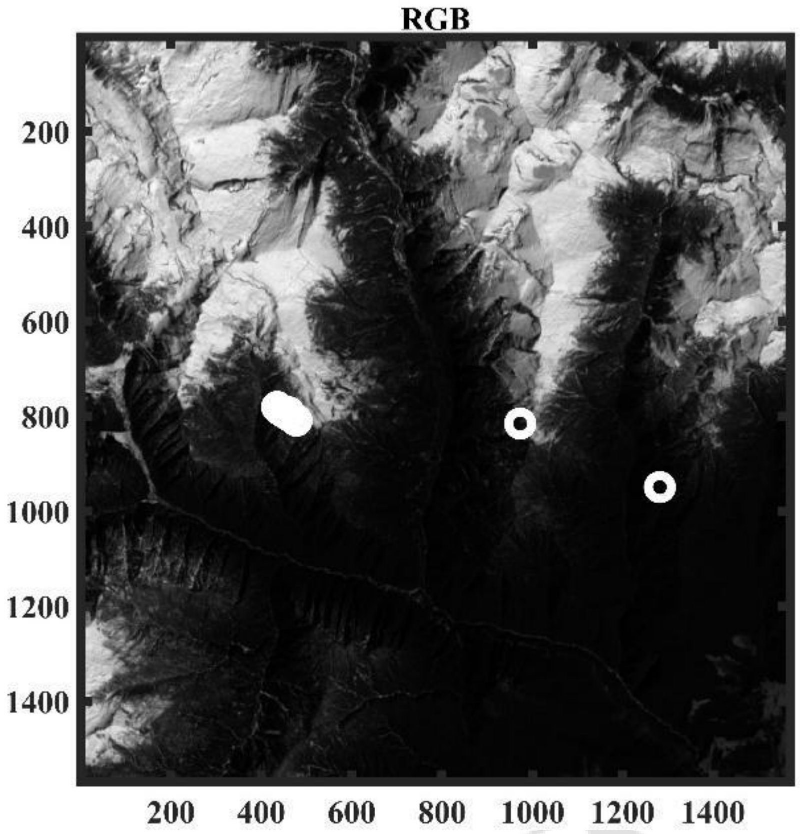

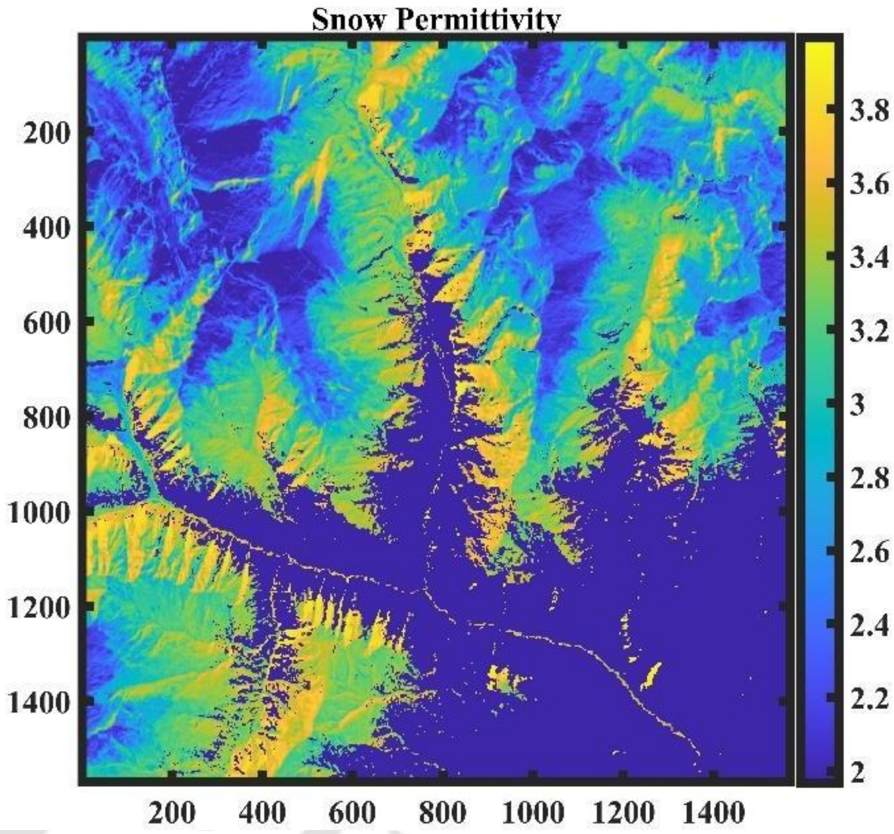

Figure 5.7: Left: - False color composite of Landsat-9 Level-2 data. Right: The snow permittivity model uses the same optical data. X and Y axes are the pixel locations in the image matrix.

5.5.3. *Snow Depth Accuracy Assessment*

The average snow depth estimated without incorporating scaling factors and weight factors for each channel (VV and VH) at the measured locations reveals 29.44 cm for the VV channel and 52.56 cm for the VH channel. This suggests an underestimation in the VV channel and an overestimation in the VH channel. The VV polarization channel tends to underestimate snow depth due to its sensitivity to surface scattering, which limits penetration into the snowpack, particularly in wet conditions where surface roughness dominates the scattering process (Nagler, 1996; Singh and Venkataraman, 2010). Conversely, the VH polarization channel overestimates snow depth as volume scattering disproportionately increases with larger snow grain sizes, enhanced wetness, and heterogeneities within the snowpack. This effect is further intensified in partially wet snow (~5% wetness), where thin liquid water films surrounding snow grains amplify the dielectric contrast and scattering intensity. Moreover, the prolonged temporal baseline of 192 days can amplify these discrepancies, as snow metamorphism processes, such as grain growth and variations in wetness over this duration, can lead to decorrelation and modify the scattering characteristics in the VV and VH channels.

Further, this study also employed a correction based on the Varade et al. (2020) snow depth model. Their methodology for this study region yielded the root mean squared error (RMSE) and mean absolute error (MAE) relative to the in-situ measurements of 12.39 cm and 11.11 cm, respectively. The expected snow depth derived from their model (R2 = 0.73) is 34.87 cm, while the mean in-situ snow depth is 38.17 cm. The notable corrections suggested by Varade et al. (2020) show that directly applying the snow depth model without adjustments is impractical for our study area. Such behavior can be attributed to the calibration of model parameters such as weight and separate scaling factors for both VV and VH channels to account for regional variability and systematic biases. The scaling factor used to adjust the scale of snow depth is determined by calculating the ratio of the mean corrected displacement to a reference snow depth. The in-situ snow depth boxplot suggests the reference snow depth estimate (Fig. 5.8, left panel). In this context, the median in-situ snow depth (36.5 cm) is employed as the optimal reference value, as it is less sensitive to outliers and provides a more representative measure of central tendency, especially considering the considerable variability observed in the in-situ data. Thus, separate scaling factors for VV and VH channels are obtained as 0.89 and 1.62, respectively.

The RMSE and MAE obtained from the proposed inversion model are 9.58 cm and 7.90 cm, respectively. This signifies an improvement of 2.81 cm in RMSE values compared to the Varade et al. (2020) snow depth inversion model. The evaluation and comparison of the suggested inversion method for snow depth relative to different existing methods are presented in Table 5.3.

Additionally, the estimation errors for snow depth appear to be considerable. It is worth noting that these errors are comparable to those of other established approaches. For instance, Awasthi et al. (2020) conducted snow depth estimation in the North-Western Himalayan region on January 21st and 22nd, 2015, using the TanDEM-X dataset and ground datasets by AWS of Snow and Avalanche Study Establishment (SASE), DRDO. Their study, which utilized polarimetric synthetic aperture radar interferometry (PolInSAR) based inversion modeling, resulted in RMSE values of 10.6 cm and 28 cm for snow depth on both dates. Similarly, Harder et al. (2016), in their study of Canadian agricultural lands using UAV-generated DEM with an accuracy of ±2.5 cm, reported RMSE values for snow depth modeling ranging from 4.1 cm to 13.7 cm. Given that the region of interest for the current study shares similarities in vegetation types with these areas, such high error values are expected.

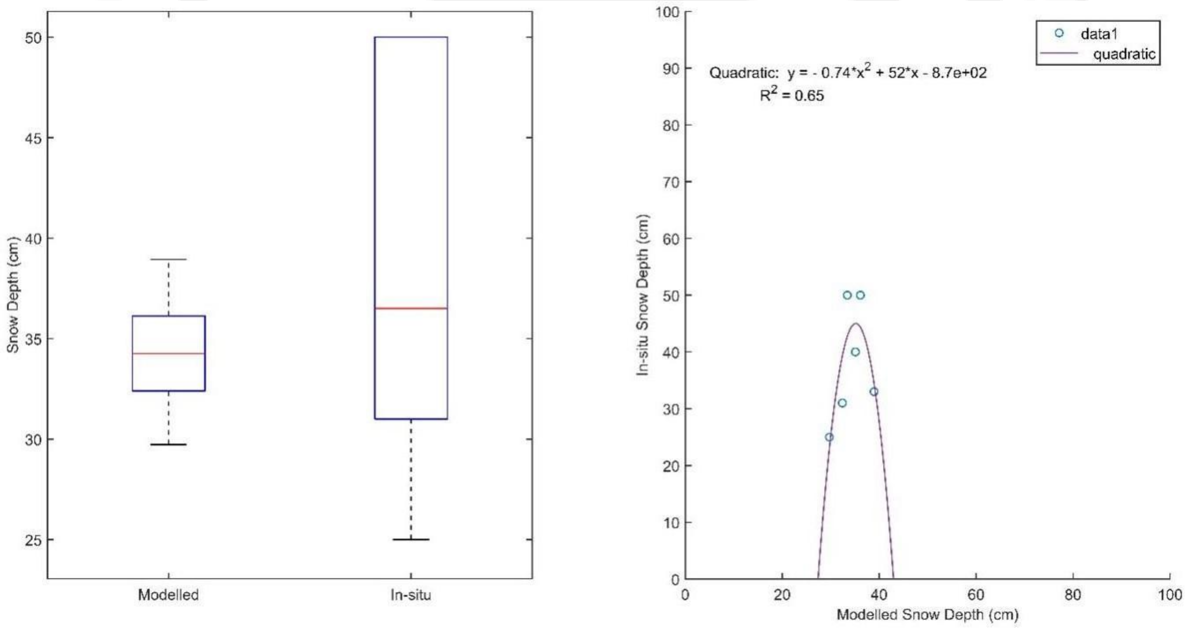

Figure 5.8: Left: Boxplot of modeled and estimated snow depth. Right: Correlation between the estimated snow depth and in-situ snow depth measurements collected during the field campaign in the study area.

It is evident from the boxplot in Fig.5.8 (boxplot) that the proposed model underestimates the snow depth in the study area. The two-tailed T-test suggests insufficient evidence to reject the null hypothesis (sample means are equal) at a significance level of 0.05. The coefficients of determination (R^2) and the root mean square error (RMSE) between the in-situ snow depth and estimated snow depth from the proposed inversion model are shown in Fig.5.8 (Right). It shows a quadratic fit (R^2=0.65) at 95% confidence interval boundaries for the predicted snow depth compared to the in-situ data. Previous research has revealed a linear relationship between snow's physical properties (snow dielectric constant, density, and wetness) (Chapter 4). The increase in the R2 value from 0.14 for the linear model to 0.65 for the quadratic model indicates the potential presence of nonlinear processes or dependencies in snow depth dynamics. This may be attributed to the nonlinear relationship between snow wetness and dielectric (Eq. 5.5). However, smaller data samples (6 in-situ points) could imply that, in this smaller sample, the physical process governing the relationship (such as snow wetness and dielectric properties) exhibits non-linear behavior that is captured well by the quadratic model. However, future studies should be focused on an increased sample size to analyze whether a broader range of conditions or variability, averaging any non-linearity, or capturing a more general trend that a linear model can approximate. The proposed model's robustness and performance are assessed using metrics such as RMSE and MAE, shown in Table 5.3. The statistical result from the quadratic fit is shown in Table 5.4. It is worth noting that the quadratic correlation fit can predict the average snow depth (36.70 cm) of the study area with an absolute error of 1.47cm. The model snow depth map for the region of interest is also shown in Fig. 5.9.

Table 5.3: Evaluation and comparison of snow depth inversion model

S. No.	Snow Depth Inversion Model	Mean In-situ Snow Depth (cm)	Mean Modeled Snow Depth (cm)	RMSE (cm)	MAE (cm)
01.	Proposed Inversion Model	38.17	34.28	9.58	7.90
02.	Varade et al., 2020	38.17	34.87	12.39	11.11

*Table 5.4: Statistical results from the correlation plot between Modelled and In-situ snow depth. F(x) = P1*x2 + P2*x +P3. Coefficients and 95% confidence bound.*

Coefficients of Fit	Value	Lower	Upper	RMSE	R^2	Adjusted R^2
P1	-0.74	-1.86	0.38	7.85	0.65	0.42
P2	52	-24.93	129.36			
P3	870	-2190	446.02			

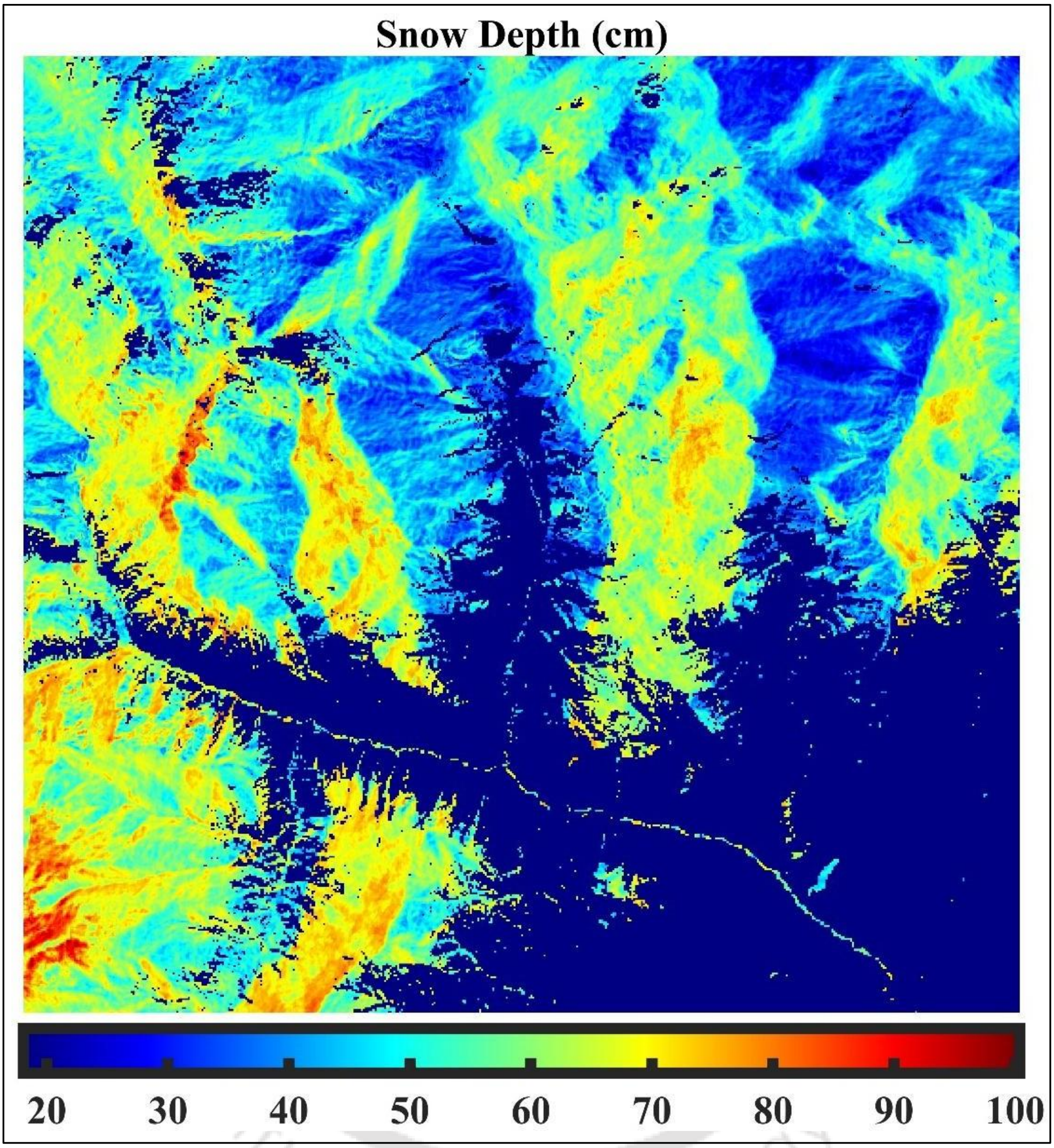

Figure 5.9: Snow depth map obtained from the proposed snow depth inversion model

5.6. The advantages and future recommendations

However, SAR Polarimetry provides an advanced framework for estimating snow dielectric properties; it is inherently complex and computationally intensive. In contrast, our proposed methodology simplifies this process by leveraging optical datasets, making it more efficient without compromising scientific rigor. Specifically, L-9 level-1 data pre-processing to obtain surface reflectance is instrumental in estimating key intrinsic parameters, such as snow wetness. The technical advantages of our approach are grounded in the theoretical framework of the collocation toolbox developed for SNAP. The methodology ensures geolocation accuracy, consistent pixel spacing/spatial resolution (S-1 and L-9 datasets are resampled to a common resolution due to their comparable spatial characteristics), and temporal synchronization. Both datasets were acquired on 14th March 2022, ensuring minimal temporal disparity and consistency in environmental conditions. Additionally, pre-processing steps, including atmospheric correction, further enhance the reliability of the data inputs for the snow depth inversion model. In summary, the methodology depicted in Figure 5.4 offers a technologically advanced yet less complex solution for snow depth inversion. Integrating optical datasets provides a scientifically robust alternative to conventional methods reliant on SAR Polarimetry, which are often time-intensive and computationally demanding. This approach enhances efficiency while maintaining the precision necessary for snow dielectric estimation, highlighting its significance in advancing snow depth inversion modeling techniques. Since the weight function has no boundary condition, the snow depth inversion model is not site-specific. Future recommendations are required to check the performance of the proposed model, which has a large set of datasets, and assess its broad range capability.

5.7. Conclusion

In this study, we introduced an adapted snow depth inversion model based on the methodology suggested by Varade et al. (2020), utilizing DInSAR techniques. Our modified model incorporates snow permittivity for each pixel value obtained from the Landsat-9 Level-2 dataset. We set the NDSI threshold for the snow cover map to be greater than 0, guided by in-situ measurements. The degradation of NDSI values at the measured locations is attributed to the presence of vegetation, as evidenced by field photographs from the study area.

Based on the outcomes and discussions presented here, it can be assured that our proposed methodology led to a compelling enhancement in snow depth estimation. The average modeled snow depth at the measured locations was determined to be 36.70 cm, whereas the expected snow depth observed in the field was 38.17 cm. The improvement in RMSE and MAE for our proposed snow depth inversion model can be attributed to alterations in the scaling factors (for each channel, VV and VH) and the weight function.

Nevertheless, there is room for further enhancement of the efficiency of our proposed model. This could be achieved through in-situ analysis of snow physical variables (snow dielectric, density, and wetness), utilization of high-resolution DEM instead of SRTM 30 arcsec, refinement of weight and scaling factors, and additional pre-processing improvements in DInSAR techniques.

6

STUDY OF CONTAMINATED SNOW COVER

Snow is considered contaminated when foreign materials are deposited/mixed with it, accelerating melting and significantly impacting the snow cover's radiative balance. Such an enhanced melting rate results in a reduction in freshwater sources at the catchment level. In optical remote sensing, snow contamination is widely studied using a normalizing difference index called the snow contamination index. This is based on the finding that the impact of snow contamination diminishes with wavelength and is most noticeable in the visible spectrum (0.3 - 0.7 μm). However, the study of snow contamination using optical remote sensing is hindered in the Himalayan terrain due to enduring cloud cover in the region. SAR data, such as Sentinel-1 can be used to ensure all-weather monitoring of such areas. This study focuses on the SAR backscattering behavior at the C-band of clear and contaminated snow for March 2022 in a part of the Eastern Himalayas of Arunachal Pradesh, India. An attempt has been made to utilize Landsat-9 and Sentinel-1 to study the snow contamination.

6.1. Introduction

Clear snow comprises ice, water, and air and has no inclusions/impurities. Snow is considered contaminated when foreign objects (ash, coal, wood, etc.) are deposited/mixed with it. Several studies (e.g., Nazarenko et al., 2016; Xu et al., 2009; Ramanathan and Carmichael, 2008; Barnett et al., 2005; Hansen and Nazarenko, 2004) have examined the impacts of snow contamination on the climate and humans. Snow contamination can accelerate melting and majorly impact the radiative balance of snow cover (Xu et al., 2009; Ramanathan and Carmichael, 2008; Hansen and Nazarenko, 2004). According to Hansen and Nazarenko (2004), understanding the connection between the cryosphere, the atmosphere, and climate depends on how a snow impurity affects snow albedo reduction. Further, the deposition of black carbon accelerates the melting of snow, resulting in a decrease in freshwater sources at the catchment level (Xu et al., 2009; Barnett et al., 2005). In addition to lowering snow albedo (Wiscombe and Warren, 1980,1981) and raising snow surface temperatures, snow contamination can have an impact on the water quality of rivers (Kirchner et al., 1993) that receive runoff during snowmelt (Balla and Garg, 2023).

The Himalayan areas present challenges for in-situ measurement due to their complex terrain and harsh weather. In such conditions, satellite remote sensing with synoptic coverage and repeated monitoring capabilities has proven to be a promising tool for studying such a dynamically changing ecosystem (Dozier et al., 1981; Donahue and Kevin, 2021; Di et al., 2022). Snow contamination is widely studied through optical remote sensing using a normalizing difference index called the snow contamination index (SCI). This relies on the observation that the effect of snow contamination is most evident in the visible region (0.3 - 0.7 μm) and decreases with increasing wavelength (Warren and Wiscombe, 1980; Negi et al., 2006, 2010). In the visible region of the electromagnetic spectrum, the contaminated snow has lower reflectance than clear snow (Staenz and Haefner, 1981; Warren, 1982; Takeuchi, 2009; Casacchia et al., 2001). Based on spectroradiometer (Di Franco et al., 2022) readings, Negi et al. (2010) introduced the snow contamination index (henceforth SCI), which uses blue and green wavelengths. They claimed that the SCI index decreases and stays negative for contaminated snow. Snow contamination can be easily identified with hyperspectral or multi-spectral datasets. However, the study area in the eastern Himalayas mostly has cloud cover and precipitation conditions, which are the significant limitations of the optical datasets (Marshall et al., 1994; Tsai et al., 2019; Awasthi and Varade, 2021). Due to this, Synthetic Aperture Radar (SAR) data proved to be an alternate solution (Notarnicola et al., 2013) in snow contamination studies. Very few studies mention that SAR backscattering is affected by snow contamination. (Tsai et al., 2019; Liu et al., 2006; Chuvieco, 2008). Also, Chýlek and Srivastava (1983) have studied the impact of contamination on the dielectric constant of the snow with varying snow surface and atmospheric conditions.

To obtain snow properties, microwave remote sensing has been widely used (Landes et al., 2007; Du et al., 2010; Chen et al., 2020; Langlois et al., 2020). Currently, available bands for SAR data are X-band (TerraSAR-X, COSMO-SkyMe), L-band (ALOS-2), and C-band (Sentinel-1) (Baghdadi et al., 2016). There are a few critical snow physical parameters that are estimated using C-band SAR data, namely snow depth (Varade et al., 2020; Lievens et al., 2022), liquid water content (Patil et al., 2020; Ma et al., 2020; Awasthi et al., 2022), dielectric constant (Frolov and Ya, 1999; Hajnsek et al., 2003; Singh et al., 2017; Varade et al., 2020), and density (Singh et al., 2017; Varade et al., 2019; Awasthi et al., 2020). The present study shows the application of C-band SAR data in snow contamination studies. Backscatter observations over snow-covered terrain are affected by various factors, including the physical properties of the snowpack, such as its dielectric constant, snow grain size (Colbeck, 1982), snow liquid water content, snow density, and snow depth, and sensor characteristics, including frequency, polarization, and viewing geometry (Ulaby et al., 1986; Bishop et al., 2011).

However, the amount of liquid water in the snow is important. Backscatter from wet snow is reduced as a result of absorption due to increased water content, but backscatter from dry snow is usually dominated by scattering off the ground surface (Baghdadi and Bernier, 1997; Luojus et al., 2007; Nagler et al., 2016). Due to noticeably different dielectric characteristics within the snowpack, the backscatter for dry and wet snow is different. Studies report that the snow cover is typically wet for clear and contaminated snow in the Sikkim Himalayas in October and April. The wetness of snow can affect the dielectric contrast (West, 2000) between air and snow, which further influences the surface roughness that can significantly affect the backscattering values (Mätzler and Schanda,1984). In SAR imagery, the surface appears smooth at a larger incidence angle, while at a smaller angle, the surface appears rough. Thus, the local incidence angle's contribution to backscattering values cannot be ignored, and the influence of this parameter should be considered.

To benefit from both datasets (SAR and multispectral), their combination (Tsai et al., 2019) will have more potential to explore. A snow mask derived from Landsat images was frequently used to extract the Sentinel-1 backscattering (Thakur et al., 2017; Nagler et al., 2016; Crawford, 2015). However, there is a limited selection of appropriate Landsat images for comparison with Sentinel-1 snow maps due to the extensive cloudiness in a mountainous area (Nagler et al., 2016). This study focuses on the backscattering properties of clear and contaminated snow for March 2022 in a part of the Eastern Himalayas of Arunachal Pradesh, India. A state-of-the-art attempt has been made to study the contaminated snow using the Sentinel-1 (S-1) backscattering characteristics in conjunction with Landsat-9 (L-9). With the advancement in the techniques, this approach will provide better insights to enhance understanding of snow dynamics. The findings underscore the potential of microwave remote sensing technologies in capturing critical snow conditions, which are vital for effective water resource management and climate impact assessments.

6.2. Study Area

Arunachal Pradesh is the 14th largest Indian state, having an elongated shape, which shares a 1080 km border with China, 440 km with Myanmar, and 160 km with Bhutan. The investigating area is Mechuka, located in the Siang basin of Arunachal Pradesh (Fig.6.1). The study area exhibits a low temperate climate and experiences distinct seasonal variations, with cold winters, mild summers, and considerable monsoonal rainfall.

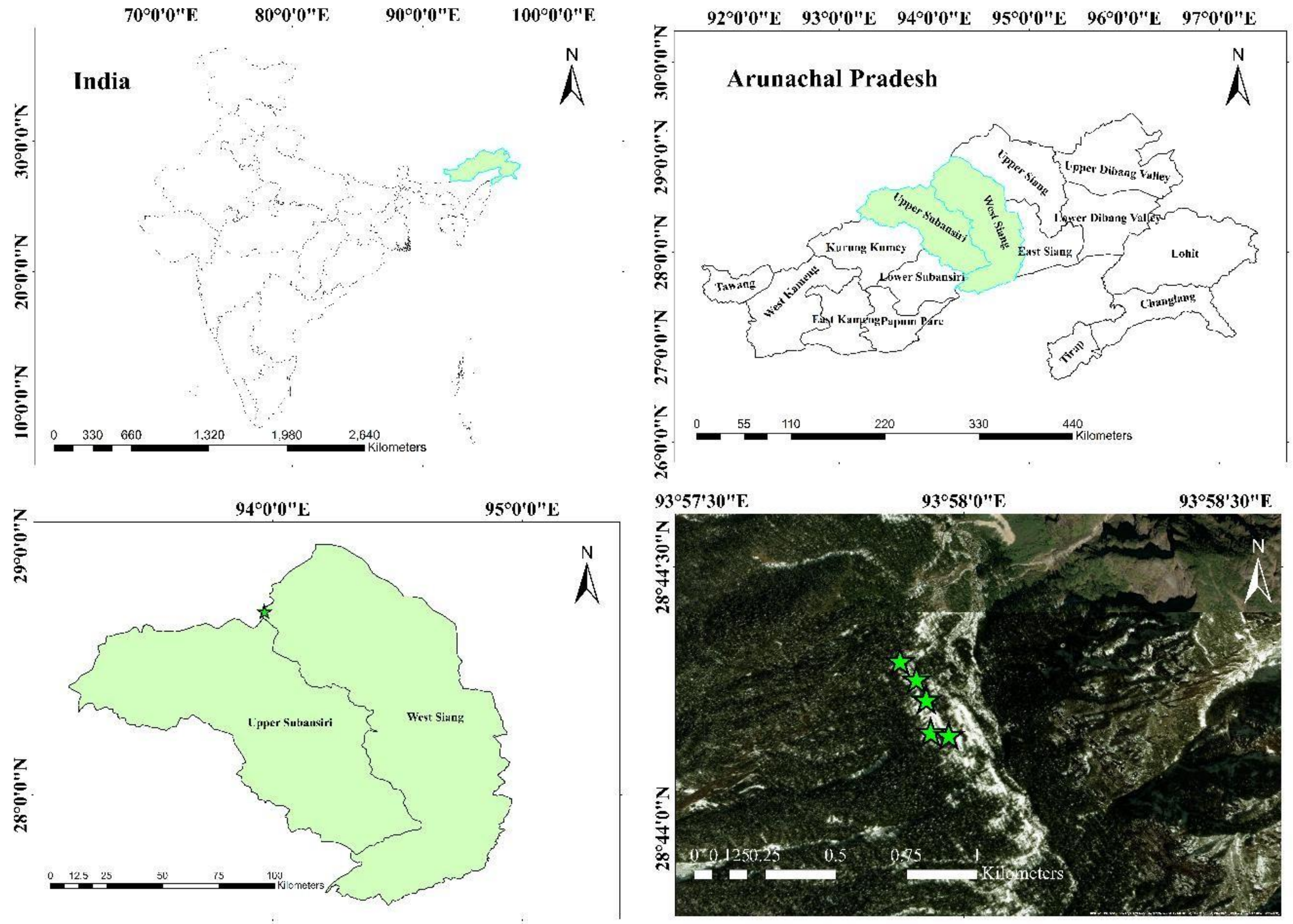

Figure 6.1: Map indicating the study area and the locations visited during the field investigation

Figure 6.2: Snow cover and snow condition in the study area on 14th March 2022.

This region demonstrates considerable topographical diversity, with elevations ranging from approximately 1,829 meters at the district capital to a maximum height of 5,248 meters. Due to its elevated location, winters in Mechukha are particularly cold, with temperatures frequently falling below freezing. The study area's geographical center is around 93°58'26.4"E longitude and 28°43'8.4"N latitude.

Based on EAR5 reanalysis data (https://apdrc.soest.hawaii.edu/las/v6/constrain?var=16467), the climatological 2 m air temperature from 1990 to 2022 ranges from approximately -11˚C to 12˚C, with an increasing trend. Snow coverage in this region reaches its maximum during March and April before the onset of ablation. These climatic conditions are influenced by the area's high altitude, contributing to its unique seasonal characteristics. The landscape in the field site (Fig. 6.2) encompasses a variety of ecosystems, including subtropical pine forests and subalpine and alpine forests.

6.3. Dataset

6.3.1. Optical Data (Multispectral)

On September 27, 2021, the National Aeronautics and Space Administration (NASA) and the U.S. Geological Survey (USGS) launched Landsat-9 as part of the Landsat program. Two scientific instruments carried by the satellite are the Operational Land Imager 2 (OLI-2) and the Thermal Infrared Sensor 2 (TIRS-2). OLI-2 offers data for nine spectral bands with a spatial resolution of 30 meters (m), except the panchromatic band, which has a spatial resolution of 15 meters. The Level 2 (L-2) product of L-9, which is a bottom-of-the-atmosphere (BOA) reflectance, has been used in this study. The Landsat-9 Level-1 dataset of the study area has 12.77% cloud cover, and the subset that contains the study area is devoid of cloud cover (Fig.6.4).

6.3.2. Synthetic Aperture Radar (SAR)

The European Space Agency (ESA) built the Sentinal-1 constellation of two satellites as a component of the European Copernicus Program. Based on the data availability and to better collocate the L-9 and S-1 datasets, images of 14th March 2022 were identified. Accordingly, the field investigation was planned and conducted on March 14, 2022. This study utilizes the level-1 Single Look Complex (SLC) product of the S-1A, which is a dual polarimetric (VV/VH) and Interferometric Wide (IW) swath mode dataset. This dataset has been pre-processed for noise (both GRD boarder noise and thermal noise), radiometric and terrain-related errors (ESA, 2024).

6.3.3. *Field Investigation*

According to the optical and SAR data acquisition date, the field investigation was conducted on March 14, 2022, in the West Siang district of Arunachal Pradesh, India, particularly in the Mechuka Valley (Fig. 6.1). During the field investigation, snow cover was spotted above the 2380m MSL and foreign particles such as soil, ash, and organic materials were observed (Fig. 6.2). The contaminated snow appears exhibiting different texture and discoloration.

6.4. Methodology

Integrating information at the pixel level, captured by different sensors, is widely practiced (Ghassemian, 2016; Pandit and Bhiwani, 2015). In an ideal situation, both sensors' images should be captured simultaneously to ensure the captured information pertains to the same state of the earth's surface. In this study, S-1 and L-9 datasets have been combined using the collocation toolbox of SNAP. The S-1 data was used as a reference, optical data was added as a secondary product, and datasets were resampled to 10m spatial resolution using bilinear interpolation. To estimate the Bottom of the Atmosphere (BOA) from level-1 data of L-9, the Sensor Independent Atmospheric Correction (SIAC) (Yin et al., 2019) technique was used with the help of Google Earth Engine.

The Normalized Difference Snow Index (NDSI) (Xiao et al., 2001; Negi et al., 2015), Normalized Difference Forest Snow Index (NDFSI), and S3 Index were used to develop the resultant snow cover map (RSM). The thresholds for NDSI and NDFSI are 0.4, whereas 0 to 0.18 for the S3 Index (Panda et al., 2022).

$$NDSI = \frac{Green-SWIR}{Green_{SWIR}} \ldots\ldots\ldots\ldots\ldots\ldots\ldots\ldots \text{(6.1)}$$

$$NDFSI = \frac{NIR-SWIR}{NIR+SWIR} \ldots\ldots\ldots\ldots\ldots\ldots\ldots\ldots \text{(6.2)}$$

$$S3 = \frac{NIR(Red-SWIR)}{(NIR+SWIR)(NIR+Red)} \ldots\ldots\ldots\ldots\ldots\ldots\ldots\ldots \text{(6.3)}$$

The SAR backscattering for the snow regions (sigma0_s) and non-snow regions (sigma0_ns) was derived using RSM. Further, an SCI mask is used to derive SAR backscattering over contaminated and clear snow.

$$SCI = \frac{Blue-Green}{Blue+Green} \ldots\ldots\ldots\ldots\ldots\ldots\ldots\ldots \text{(6.4)}$$

The snow wetness is derived using the NDSI-Near Infrared (NIR- band 5) feature space of the L-9 L-2 dataset, using the methods of Varade and Dikshit (2020). It is well known that snow wetness, dielectric, and density are interrelated (Tiuri et al., 1984; Denoth, 1994; Kendra et al., 1994). Snow wetness is used to derive dielectric and density using the methods discussed in Method-II of Chapter 4.

Due to weather conditions in high-altitude regions, the S-1 datasets have been widely used to estimate the physical properties of snow (Varade and Dikshit, 2020; Mascolo et al., 2021). The dominant scattering mechanism over contaminated and non-contaminated snow is explained using a generalized Stokes vector decomposition of the S-1 dataset (Mascolo et al., 2021). Chapter 4 has provided the pre-processing steps for estimating the Stokes parameters.

$$s = m_v[1; -0.5; 0; 0] + m_s[1; \cos(2\alpha); \sin(2\alpha)\cos(\delta); \sin(2\alpha)\sin(\delta)] \quad (6.5)$$

where s = [s1; s2; s3; s4] is the Stokes vector, m_v is volume scattering power, and m_s is surface scattering power.

6.5. Results

6.5.1. Snow Cover Mapping

NDSI techniques are extensively used to map the snow cover (Crane and Anderson, 1984; Hall et al., 2002; Dietz et al., 2012), where a 0.4 threshold can differentiate snow from clouds (Dozier, 1989; Klein and Barnett, 2003). It is also possible that NDSI may be overestimated or underestimated in the forest region (Dietz et al., 2012). During the field investigation, the Alpine forests were observed in parts of the study area (Fig. 6.2). In such situations, the NDSI threshold needs to be decreased to prevent underestimation, provided the subset of the scene is cloud-free. The pixels with NDSI values less than 0.4 are identified as snow-covered areas, provided the Normalized Difference Vegetation Index (NDVI) is around 0.1 (Hall et al., 2002). However, the illumination angle and the level of contamination can also affect the threshold (Varade and Dikshit, 2018). As the in-situ locations are surrounded by vegetation and the spatial resolution of data is 10m, the NDSI values within those pixels have deteriorated (Fig. 6.3).

In the locations where snow depth is between 3 and 20 cm, the NDSI values are less than 0, while the NDVI values (higher values indicate the presence of vegetation) are more significant than 0.7. Therefore, the NDFSI and S3 indices are used to identify the presence of snow in the forest area, but their value is also less than the suggested thresholds. The NDFSI value greater than 0.4 is identified as snow, while for S3, it is between 0 to 0.18 (Panda et al., 2022). The degradation of NDSI and NDFSI values for such locations is attributed to the higher value of NDVI. The NDSI, NDFSI, and NDVI values for the remaining in-situ locations range from

0.17 to 0.48, 0.25 to 0.54, and 0.19 to 0.37, respectively. Consequently, to prevent overestimating snow cover amounts, the thresholds for NDSI and NDFSI are set at 0.4, and for S3, they are between 0 and 0.18 (Panda et al., 2022).

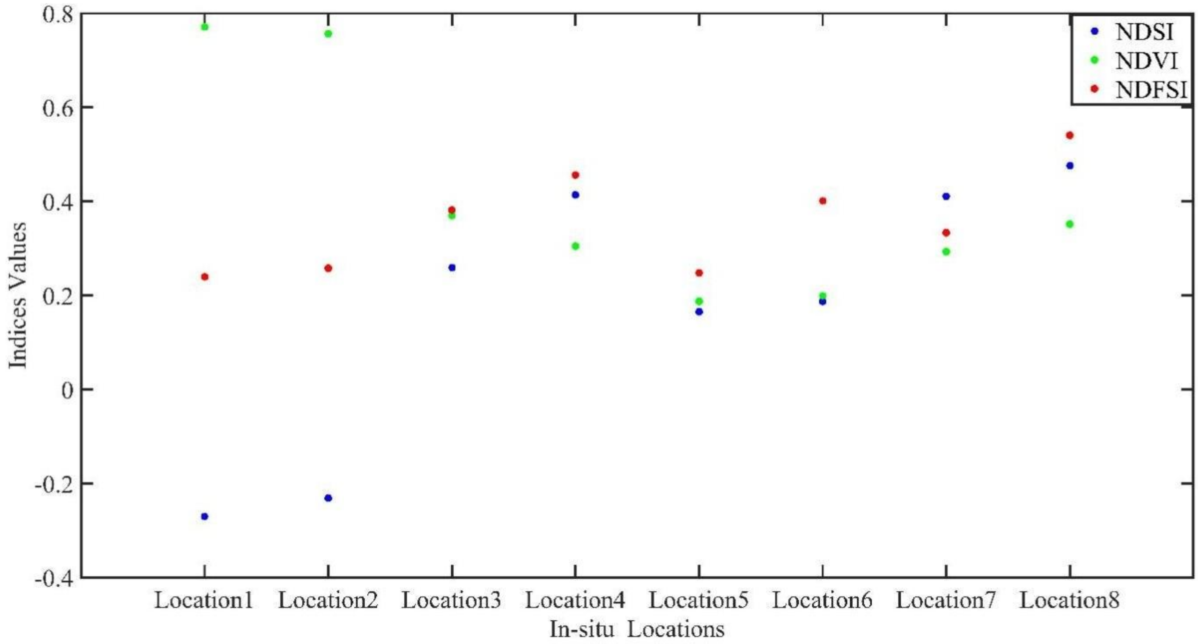

Figure 6.3. In-situ snow-covered locations estimated the Indices values (NDSI/NDVI/NDFSI).

6.5.2. Snow cover and non-snow cover backscattering

The RSM and the snow condition map in terms of clearness and contamination are shown in Fig. 6.4. At the same time, SAR backscattering ranges for the study area and snow cover are shown in Fig. 6.5. Contaminated snow is evident at the periphery of clear snow cover (Fig. 6.4). It is also observed that the presence of clear snow is comparatively higher than contaminated snow (Fig.6.4).

It is observed from the boxplot (Fig. 6.5) that the sigma0_s is comparatively lower than sigma0_ns, which may include different vegetation, soil, etc. The soil and canopy moisture in the non-snow regions (snow-free ground) influence the SAR backscattering strength (Pulliainen et al., 1994, 1996). Flora is abundant in the study area, and as the ablation period is just starting, the snowmelt has left the soil damp. According to a study by Koskinen (2001), backscattering from forest canopy is higher than from wet snow.

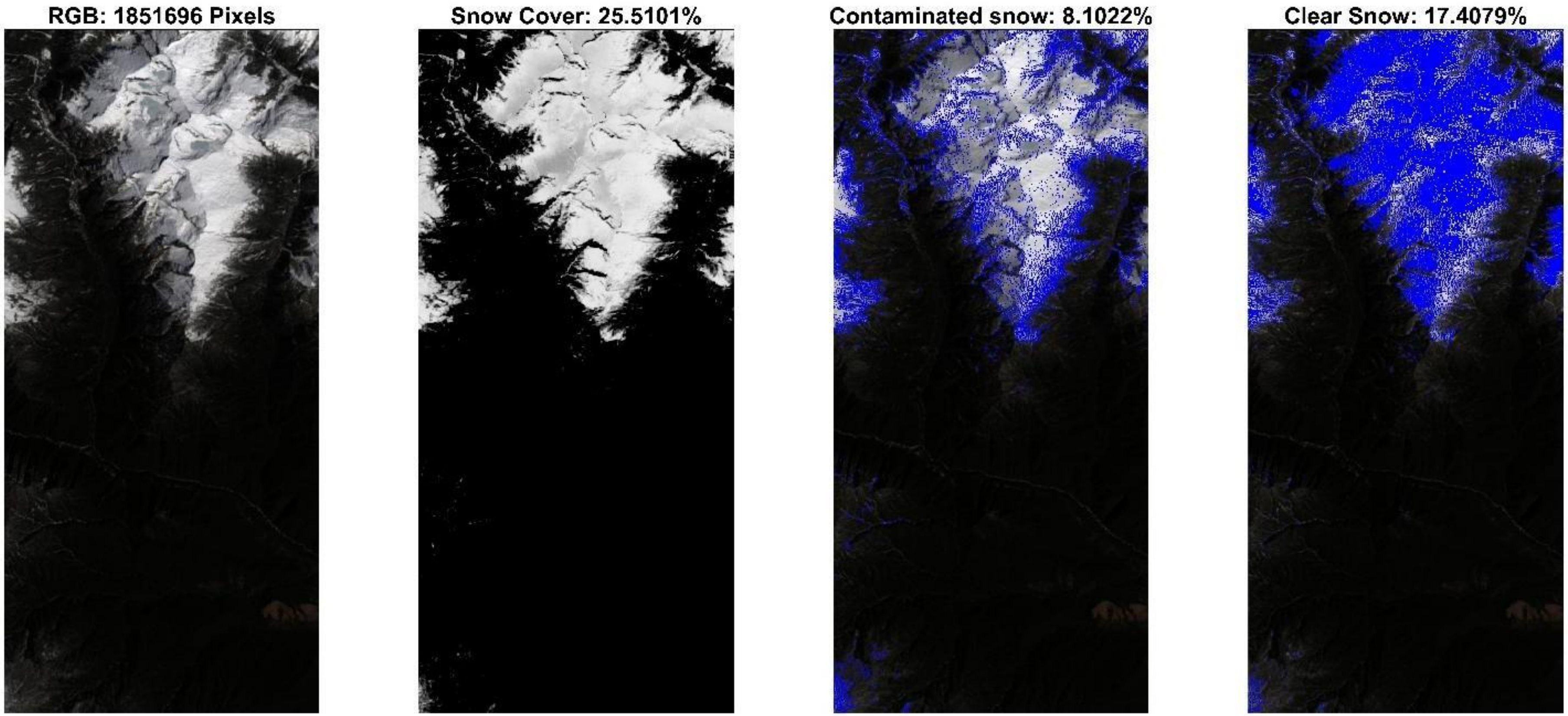

Figure 6.4. RGB, Snow cover, contaminated snow, clear.

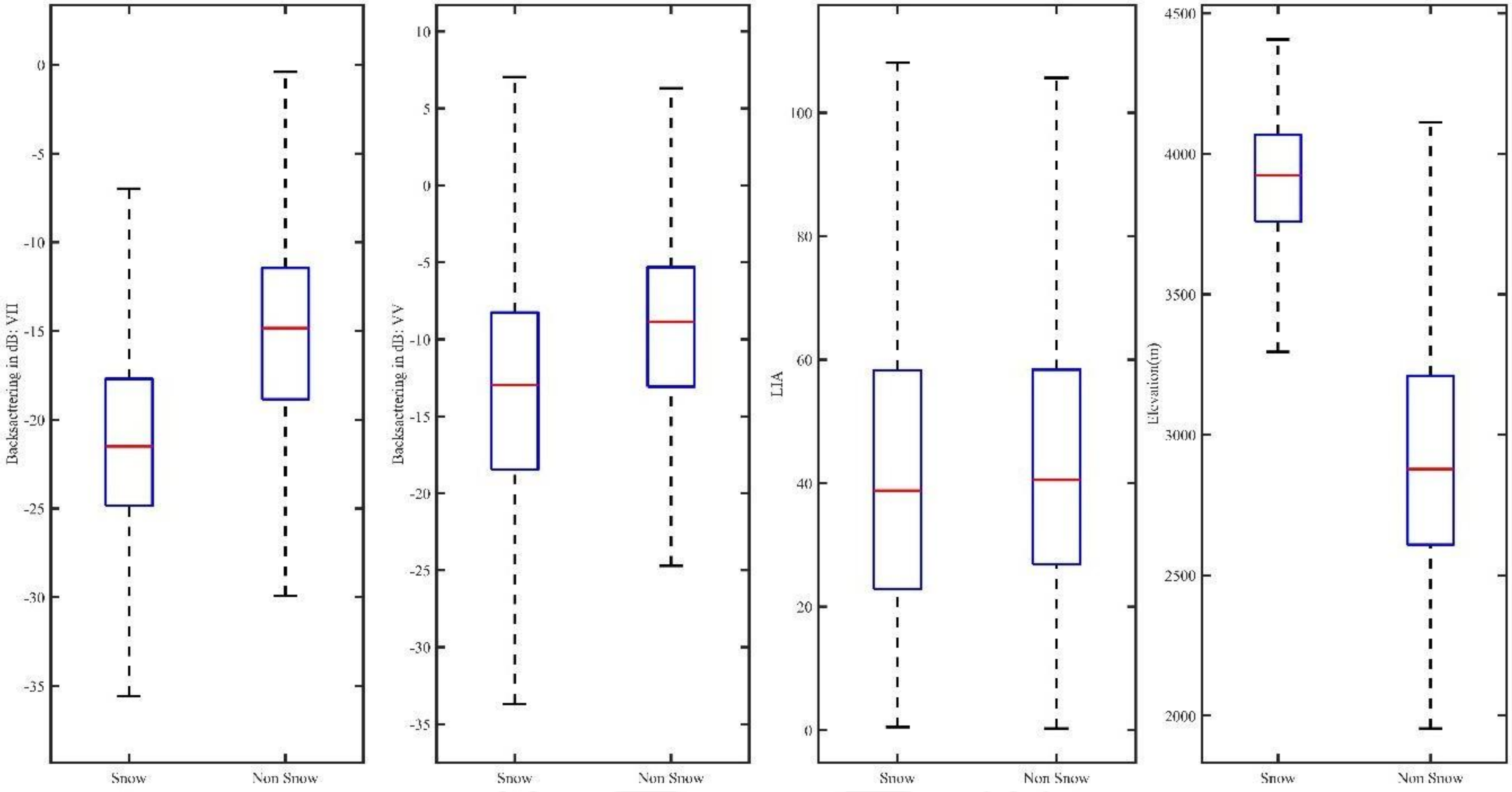

Figure 6.5: Box plot for snow and non-snow regions.

In addition to the ground's surface features, the local incidence angle (LIA) affects the SAR backscattering values (Nagler et al., 2016). Backscatter dramatically reduces with increasing incidence angle on bare or sparsely vegetated terrain with smooth soil surfaces (Ulaby et al., 1982). Snow-covered surfaces at a relatively higher elevation (Fig. 6.5: Elevation boxplot) are regarded as having poor vegetation. Fig. 6.6 illustrates the link between LIA and SAR backscattering (VH and VV) for snow-covered areas.

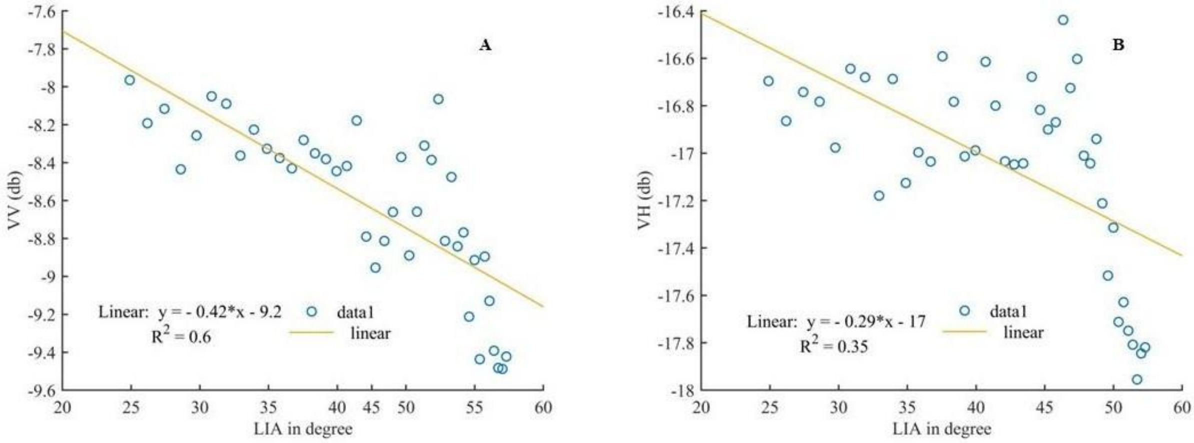

Figure 6.6: Scatter plot between SAR backscattering (VH-left and VV-right) on the y-axis and LIA on the x-axis.

If LIA is limited to a small range, researchers (Pathe et al., 2009) have assumed a near-linear relationship between SAR backscattering (sigma0) and LIA. According to Nagler et al. (2016), geometric errors significantly impact incidence angles higher than 75° and lower than 15°. On the other hand, those that exhibit a normal distribution are used to determine the appropriate range of local incidence angles (Nagler et al., 2016; Varade et al., 2020). The LIA's normal probability plot (not displayed here) reveals that while there is a notable deviation below 20° and above 60°, the LIA follows a distribution that is comparable to the normal distribution between 20° and 60°. Unique local incidence angles (total 41 points) that follow the normal distribution are considered. Fig. 6.6 represents the SAR backscattering as a function of the local incidence angle over the snow surface. The mean angular dependence of each polarization (VH and VV) over the snow surface is 1.29 and 1.42, respectively. Based on coefficients of regression R^2 and mean angular dependence values, the VH polarization channel is less angular dependent than the VV channel, which corroborates with the previous study (Nagler et al., 2016). $Mean\ Anglular\ dependence = 1 - slope\ of\ \sigma_0$ dB vs $\log[\cos(\theta)]$ ... (Baghdadi et al., 2001; O'Grady et al., 2013)

6.5.3. SAR Backscattering over contaminated and non-contaminated snow

This work uses a snow contamination mask based on SCI obtained from the L-9 Level-2 dataset. However, a snow mask derived from Landsat images is frequently used to extract the S-1 backscattering (Nagler et al., 2016; Crawford, 2015). Thus, this study employed an SCI-based snow contamination map to explain SAR backscattering behavior in clear and contaminated snow. In Fig. 6.7, the effect of snow contamination on SAR backscattering is shown. Thus, this study employed an SCI-based snow contamination map for SAR backscattering behavior in clear and contaminated snow. Here, we show the average backscattering behavior of VV and VH channels over non-contaminated and contaminated snow, considering a few pixels with unique SCI values. The SCI values less than 0 are contaminated, while positive values are for clear snow. This plot shows that both average backscattering (VH and VV channels) values for the contaminated snow are comparatively higher than non-contaminated. The average values of VH backscattering for clear and contaminated snow are -24.54 dB and -19.36 dB, respectively. Such behavior of SAR backscattering channels over clear and contaminated snow is followed by studying the scattering mechanism over both surfaces.

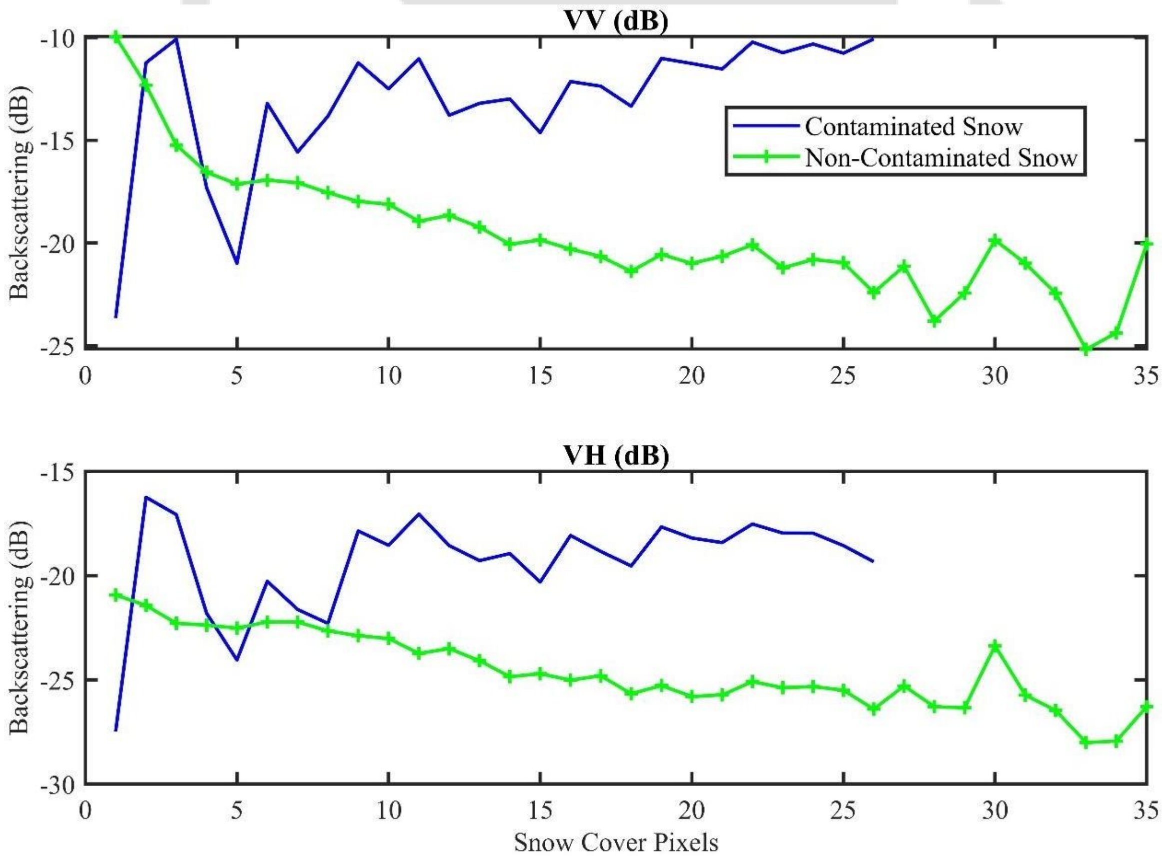

Figure 6.7: The snow backscatter variation in contaminated and non-contaminated snow cover.

6.5.4. *Dominant Scattering Mechanism Over Contaminated and Non-Contaminated Snow*

Many features of the snow layer influence the backscatter from the snowpack. Stratigraphy has minimal effect on backscattering from wet snow because of the limited penetration depth. (Nagler 1996; Singh and Venkataraman 2010). The air-snow interface, the snowpack volume, and the snow-ground interface all contribute to the overall backscattering of the snowpack (Shi et al., 2016; Singh et al., 2017). Contributions from the volume scattering of the snowpack and the scattering elements from the snow/ground interface make up the majority of the backscattered power in dry snow. As the dry snow ages, the top layer of the snowpack melts and refreezes, increasing the size of the snow grains and raising the surface component from the air-snow interface (Shi and Dozier, 1995; Yueh et al., 2009; Varade et al., 2020a). According to Thakur et al. (2012), there is usually no component from the snow-ground interface. However, the backscatter from the wet snowpack has a more substantial surface component and a lower volume component.

Using Stokes parameters-based scattering decomposition (Eq. 6.5), this study shows that non-contaminated and contaminated snow show prominent surface scattering (Fig.6.8) and are wet snow in certain conditions. Fig. 6.9 (wetness boxplot) illustrates the wet condition of the snowpack. Light scattering in contaminated snow exhibits more significant variability than in non-contaminated snow, influenced by multiple factors. Contaminated snow is characterized by increased surface roughness and unevenness, diverse impurities contributing to inconsistencies, and potentially altered melting rates. Collectively, these factors result in a more variable and unpredictable scattering behavior in contaminated snow relative to its non-contaminated counterpart.

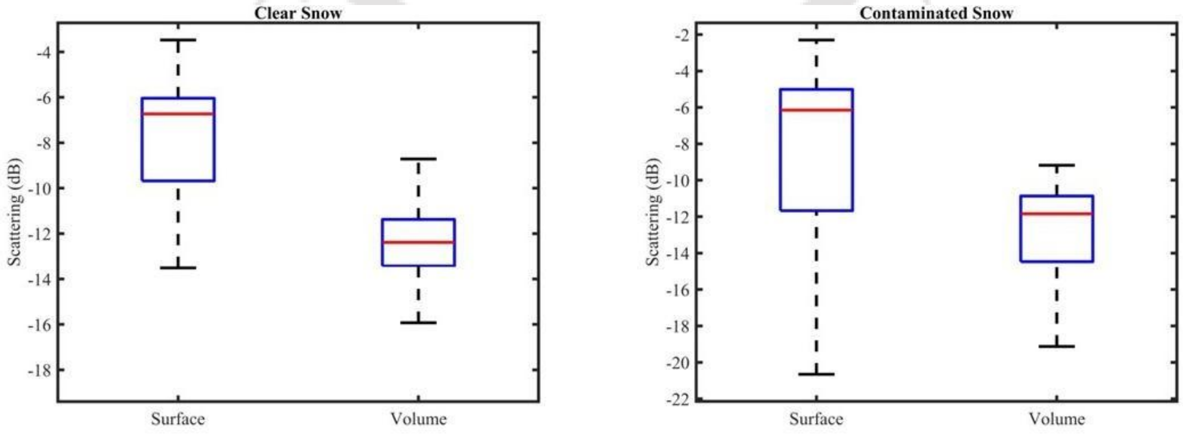

Figure 6.8: Surface and Volume scattering power of clear (left) and contaminated (right) snow.

6.5.5. *Effect of snow contamination over snowpack physical parameters*

According to studies, backscattering values decrease with increasing wetness because of increased signal absorption by water (Stiles and Ulaby, 1980; Ulaby et al., 1986; Fung et al., 1994; Karamvasis and Karathanassi, 2023). The box plot (Fig. 6.9) makes this quite evident, showing low average wetness values for sigma0_con, which has comparatively more backscattering strength than sigma0_cl. Contaminated snow has a significantly different snow wetness and dielectric constant than clear snow. The median value of snow wetness for contaminated snow is lower than clear snow's wetness. The dielectric constant of the wet snowpack directly depends on the liquid water content (Ambach and Denoth, 1980; Hallikainen et al., 1982; Tiuri et al., 1984; Denoth, 1989, 1994; Kendra et al., 1994; Awasthi and Varade, 2021). It has been observed from the results that both clear and contaminated snowpacks are in wet conditions (Fig. 6.9).

We found organic matters such as plant debris, vegetation cover, soil, and vehicular exhaust to be the source of contamination during the field investigation. These sources of pollutants affect the microstructure and thermal characteristics of the snow, and the chemical interactions within the snowpack all affect how much water may be retained in snow mixed with organic matter. The snowpack, water retention changes, and isolated melting will result from such contamination (Larose et al., 2013; Kozioł et al., 2017). Thus, snow contamination reduces the snowpack's total liquid water content and the dielectric constant of snow.

The physical process of how contamination affects the snow geophysical parameters, including snow wetness, is altering the structure of the snowpack (dielectric constant and surface roughness), increasing radiation absorption (albedo change), and modifying capillary action. It is observed from Fig.6.9 that the average volumetric liquid water content for both contaminated and non-contaminated snow ranges around 3-5% by volume. Liquid water in the snowpack functions as a lubricant, helping the snow grains bond. This physical process is called wet snow metamorphism. This phenomenon can occur in contaminated and clear snow as long as liquid water is present. The presence of contaminants such as organic matter, soil particles, or pollutants alters the dynamics of the process and impacts the snow's geophysical properties. In contaminated snow, due to the changes in the physical structure and increased impurity levels, water may pool more in certain regions, disrupting uniform capillary action and leading to uneven snowmelt patterns.

The contaminated snow with lower SCI values has higher SAR backscattering values than clear snow with higher SCI values. The box plot (Fig. 6.9) displays the backscattering, LIA, elevation, snow wetness, and dielectric values for contaminated and clear snow. In comparison to sigma0_cl (VH: -22.40db; VV: -16.46db), sigma0_con has comparatively higher median value (VH: -20.58db; VV of -10.49db).

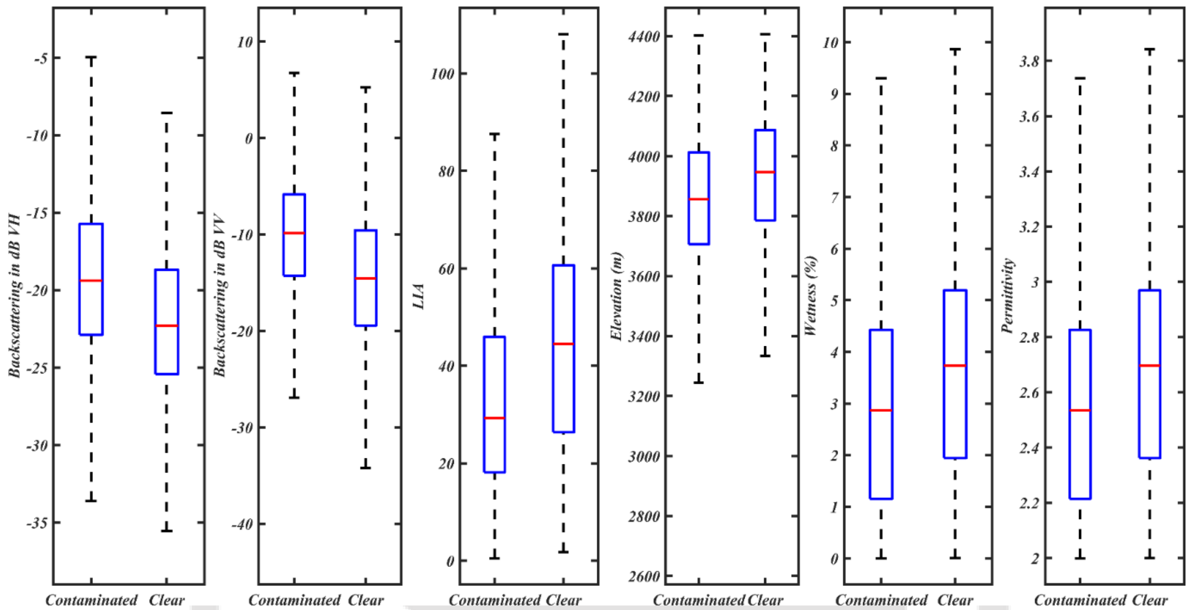

Figure 6.9: Box plot for clear and contaminated snow

Backscattering is insensitive to surface roughness at low moisture levels because volume scattering predominates, and the dielectric difference between the air and snow is minimal. Backscattering is susceptible to surface roughness as snow wetness increases. This is because an increasing surface scattering component and a decreasing volume scattering component led to the surface scattering component becoming dominant, which is evident from Fig.6.8. Both contaminated and clear snow have been found to fall into the wet snow category (Fig.6.9). The backscattering coefficient of wet snow is primarily influenced by the roughness and wetness of the snow cover, rather than the snow water equivalent (snow density and depth), as the air-snow interface is the primary source of backscatter (Ulaby et al., 1986; Fung et al., 1994; Shi and Dozier, 1995). Fig. 6.10 shows the box plot of the non-contaminated snowpack's root mean square (RMS) height. According to Marpaung et al., 2019 the RMS height is a function of the ratio between backscattering values in VH and VV polarization.

It is evident from Fig. 6.10 that the non-contaminated snow surface is comparatively smoother than contaminated snow. Thus, contaminated snow having higher surface roughness contributes to strengthening backscattering signals. The LIA for contaminated snow in the box plot (Fig.6.9) shows comparatively lower angles than the LIA for clear snow.

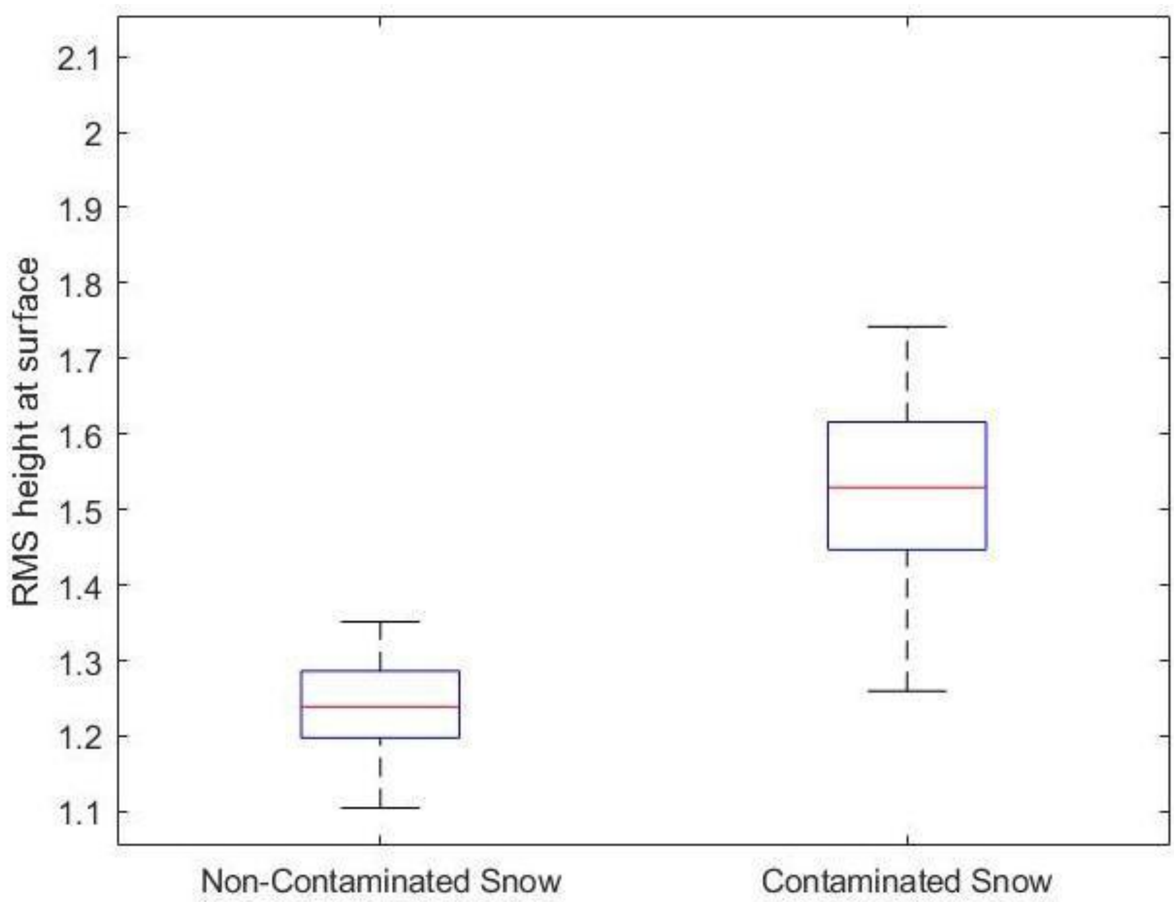

Figure 6.10: Box plot of RMS height at the surface of clear and contaminated snow.

6.5.6. SAR backscattering and the Snow Contamination Index (SCI)

Based on snow contamination masks, the VV-polarized and VH-polarized backscatter of S-1 is extracted for the two classes (contaminated and non-contaminated snow). Thus, the relation between SAR backscattering and SCI has been studied using a scatter plot for selected pixels with unique SCI values. The red dots in Fig. 6.11 are contaminated snow with negative SCI values, while the blue dots are non-contaminated snow with positive SCI values. It is evident from Fig. 6.11 that positive SCI values (non-contaminated snow) correspond to lower SAR backscattering, while negative SCI values (contaminated snow) have comparatively higher SAR backscattering values. The coefficients of regression R^2 for the VH channel ($R^2 = 0.8$) are comparatively higher than the VV channel (R^2 =0.69), possibly due to less angular dependency of the VH channel. To access the physical correlation between SAR backscattering at the C-band and SCI derived from multispectral data. It is important to clarify the distinct physical implications of SAR backscattering values and SCI

SAR backscattering depends on target geometry, orientation, surface roughness, look angle, dielectric, liquid water content, and contamination (Colbeck, 1982; Tsai et al., 2019; Liu et al., 2006; Chuvieco, 2008). On the other hand, the SCI is the normalized difference between blue and green wavelength bands that decreases and remains negative for contaminated snow (Negi et al., 2010). However, it does not provide information about the degree of contamination. Fig. 6.11 represents a significant physical relationship between SAR backscattering and SCI values, and it also differentiates between the non-contaminated and contaminated snowpacks.

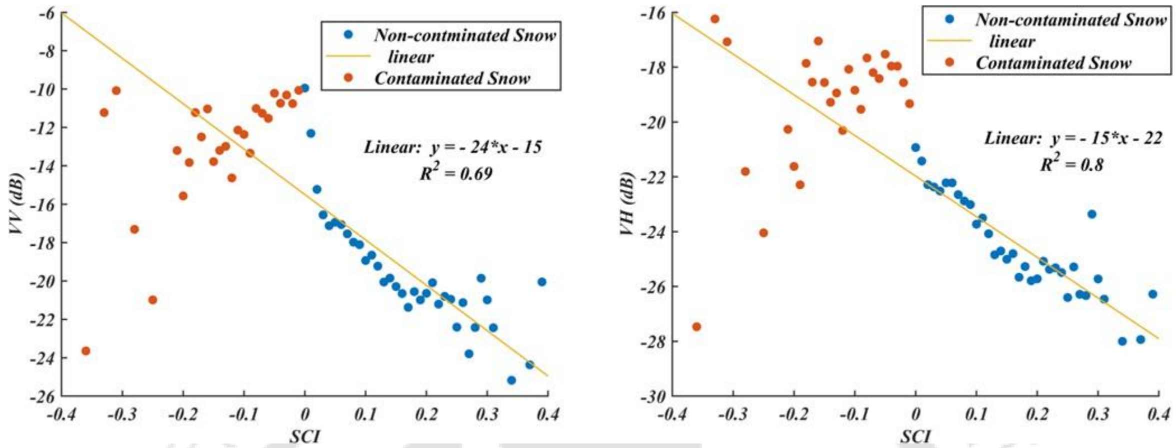

Figure 6.11: Scatter plot between SAR backscattering (VV-left and VH-right) and SCI

6.5.7. *Multivariate Linear Regression*

It is clear from the above result and discussion that SAR backscattering over snowpack will be affected by snow physical parameters (dielectric/wetness), SAR illumination angle (LIA), and snow contamination. Since the wetness and dielectric of the snowpack are directly related, one of the parameters will be redundant. The multivariate linear regression analysis (Mandal et al., 2021) is performed to quantify the contribution of each independent parameter towards SAR backscattering of snowpack at the C-band. The analysis is carried out on three different combinations (i) SAR backscattering of snowpack with LIA, dielectric, and SCI (Model A), (ii) SAR backscattering with LIA, wetness, and SCI (Model B), and (iii) SAR backscattering with LIA and SCI (Model C) (Table.6.1). In all three cases, it is observed that snow dielectric/wetness are the dominant factor influencing the SAR backscattering over the snowpack, while SCI have a weak contribution. It was observed in the previous section that as wetness increases, the backscattering becomes susceptible to surface roughness. Here, snow contamination has been observed to affect the snowpack wetness and surface roughness. Due to the increasing surface roughness of contaminated snow, the backscattering values have enhanced over that snowpack.

Table 6.1. Multiple linear regression analysis of the SAR backscattering of snowpack concerning snowpack physical parameters (snow dielectric/wetness), LIA, and SCI for 14 March 2022 over the study area.

Model	LIA	Dielectric	Wetness	SCI	RMSE	R-Squared	Intercept
A	-0.20	5.33	NA	-21.69	4.33	0.34	-27.83
B	-0.20	NA	0.996	-21.69	4.33	0.34	-17.17
C	-0.15	NA	NA	-33.08	4.79	0.19	-15.29

6.5.8. Future research direction

The study utilizes the SCI, traditionally derived from optical remote sensing data, and C-band SAR data to analyze snow contamination (Fig.6.11). Fig.6.11 shows a significant correlation between SAR backscatter and SCI values, distinguishing between contaminated and non-contaminated snowpacks. However, the application of the NDSI has demonstrated the relevance and acceptance of thresholds developed for optical datasets in SAR backscattering analyses over snow-covered areas, as supported by past researchers (Thakur et al., 2017; Nagler et al., 2016; Crawford, 2015; Bhawana et al., 2024). While this validates the usage of SCI for SAR-based analyses, the study also acknowledges the need to develop an index specifically for radar observations. While the current findings provide a foundational understanding, future research should focus on temporal or multi-seasonal analyses to capture the dynamics of snow contamination.

6.6. Conclusion

The snow condition in terms of snow contamination is studied using the multispectral (L-9) and SAR(S-1) datasets for the Mechuka region in Arunachal Pradesh, India. The range of SAR backscattering for snow and non-snow regions is obtained using the resultant snow cover map. The snow-cover regions have comparatively lower backscattering than non-snow areas. The contaminated snow has a comparatively higher backscattering value than clear snow. The average wetness for both snow classes ranges from 3-5% by volume. In contrast to the visible electromagnetic wavelength region, where contaminated snow exhibits a lower reflectance value than clear snow, the SAR backscattering for contaminated and clear snow exhibits opposite features in the microwave region of the C-band. It is observed from the analysis that the key parameters influencing SAR backscattering over contaminated snowpacks are (i) local incidence angle, (ii) snow wetness, and (iii) surface roughness.

7

CONCLUDING REMARKS

7.1. Conclusions

In high-altitude cold regions, sustainable eco-hydrology is intrinsically linked to understanding and managing the dynamics of snow and glaciers, which serve as critical freshwater reserves and indicators of climate variability. Locally, snow cover influences soil parameters such as hydraulic conductivity, moisture, and temperature, impacting carbon sequestration and microbial activity, thereby sustaining ecosystem health and biodiversity. At the regional scale, snow properties directly regulate water availability, groundwater recharge, and river discharge, supporting agriculture and hydropower generation. Essential snow characteristics, including albedo, depth, density, and thermal insulation, are pivotal in governing geological and biochemical cycles critical to eco-hydrological resilience.

The Indian Himalayas face escalating challenges due to natural and anthropogenic pressures, amplifying climate change impacts and intensifying hazards such as landslides, floods, and forest fires. Disasters like the Chamoli landslide underscore the urgent need for robust predictive and mitigation strategies. Key snow geophysical properties (SGPs), such as dielectric constant, density, depth, impurities, and liquid water content, are vital for assessing avalanche risk, hydrological processes, and flood potential. Effective climate engineering strategies for disaster risk reduction and adaptation to changing hydrological cycles depend on precise, high-resolution data on these SGPs. However, the complex terrain of the Himalayas presents significant challenges for acquiring such data through conventional in-situ methods, emphasizing the need for advanced remote sensing and geospatial technologies to enhance data acquisition and analysis in these regions.

The primary contribution of this study is developing and implementing the advanced use of multispectral, synthetic aperture radar (SAR), and hyperspectral datasets for estimating key snow geophysical parameters (SGPs), such as dielectric properties, density, wetness, grain size, impurities, and snow depth within the complex terrain of the Northeastern Indian Himalaya.

The first objective concludes with a detailed case study highlighting the development of an inversion model for snow grain size estimation over the South Lhonak glacier region following the flash flood event on October 4, 2023. Utilizing PRISMA hyperspectral data acquired on October 8, 2023, the study successfully mapped snow grain size through the spectral information divergence method, integrating the JHU spectral library as the reference endmember. The major conclusions that could be drawn from this analysis are

1. The snow grain size mapping in the South Lhonak Glacier region using PRISMA hyperspectral data acquired after the Glacial Lake Outburst Flood (GLOF) event on October 4, 2023. The mapping employs the Spectral Information Divergence (SID) method, with results validated through the absorption band area technique.
2. PRISMA hyperspectral data estimates snow grain sizes comprising 240 spectral bands and a spatial resolution of 30m. The analysis incorporates the JHU snow spectral library to categorize snow into frost, fine, medium, and coarse granular types.
3. The validation process uses the absorption band area at 1.03 µm to measure energy absorption by snow grains, revealing an inverse relationship between grain size and reflectance. This approach provides reliable grain size estimations, even without field measurements.
4. The post-GLOF surface snow layer predominantly exhibits coarse grain size, aligning with the expected ablation phase characteristics observed in the Himalayan region during October.
5. The research underscores the significance of hyperspectral remote sensing for detailed snowpack analysis, facilitating insights into melt areas, snowpack energy balance, and surface properties. It also emphasizes the importance of field-based validation to enhance the accuracy and robustness of the developed model.

The second objective integrates field measurements with Sentinel-1 to formulate a novel inversion model for snow dielectric based on Sentinel-1-derived Stokes parameters. The work focuses on developing an inversion model for Rathong Glacier in West Sikkim, India, within the Eastern Himalayas, which can be applied to all land surface forms. This model has shown significant accuracy in predicting snow dielectric, density, and wetness compared to existing models. The significant outcomes of this objective are

1. A state-of-the-art inversion model was developed using Sentinel-1-derived Stokes parameters to estimate snow dielectric, density, and wetness. The model leverages dual-polarized Sentinel-1 data (VV and VH) and applies Looyenga's and Denoth's equations for density and wetness estimation.
2. In-situ measurements were conducted using the Snow Fork instrument in April 2022 along a 45 km trek path to the Rathong Glacier, measuring snow dielectric, density, and wetness.

3. Sentinel-1A C-band data from a descending pass on April 6, 2022, was used. The study employed the Sentinel Application Platform (SNAP) for pre-processing steps such as radiometric calibration, terrain correction, and Stokes parameters estimation.
4. The inversion model uses dual-pol Stokes vectors and a combination of semi-empirical and linear mixing equations for parameter estimation.
5. The dielectric constant, density, and wetness values obtained from the model showed good agreement with in-situ measurements (correlation coefficient > 0.7). The dielectric constant ranged from 1.28 to 2.53, density from 0.145 to 0.511 g/cm^3, and wetness from 0.11% to 4.83%.
6. The modeled results were overestimated in comparison to in-situ values, particularly in areas with shallow snow depths.
7. A two-tailed t-test confirmed that the modeled and measured parameters were statistically similar, supporting the model's validity. Linear fits between modeled and measured values showed RMSEs of 0.26 for dielectric, 0.078 for density, and 0.847 for wetness.
8. The proposed model outperformed existing models regarding correlation coefficients (R^2), RMSE, and Mean Absolute Error (MAE).
9. Limited in-situ measurements restricted the analysis of intermediate data. The model's dependence on the scatterer orientation angle and shallow snow depths during the ablation period was identified as a limitation. While results are promising for the test region, broader validation with diverse datasets is required for wider applicability.

The third objective presents an enhanced snow depth inversion model that integrates the Differential Interferometric Synthetic Aperture Radar (DInSAR) technique with data from Landsat-9. By leveraging the complementary capabilities of these platforms, the proposed model aims to improve the accuracy and reliability of snow depth estimation in remote and complex terrains. The noteworthy outcomes from this objective are as follows:

1. It highlights the advantages of spaceborne remote sensing techniques, particularly Synthetic Aperture Radar (SAR), in overcoming the limitations of traditional snow measurement methods.
2. The study introduces an improved snow depth inversion model by integrating Differential Interferometric SAR (DInSAR) data from Sentinel-1 with Landsat-9

datasets for accurate snow wetness, dielectric, and density estimation.

3. The research focuses on the Mechukha region in Arunachal Pradesh, a challenging high-altitude terrain in the Eastern Himalayas.
4. The model incorporates snow dielectric and phase corrections using empirical equations, achieving improved accuracy compared to traditional InSAR techniques.
5. The performance of the proposed snow depth inversion model shows improvement after implementing the modified weight function and scaling values to the existing model. The final snow depth inversion model achieves a Root Mean Squared Error (RMSE) of 5.74 cm and a Mean Absolute Error (MAE) of 4.94 cm, demonstrating significant accuracy in estimating snow depth over the alpine regions of the Eastern Himalayas.
6. The research offers advancements in applying SAR and multispectral data for snow geophysical parameter estimation, providing a methodological framework for future studies in similar terrains.

The fourth objective of this study investigates the SAR backscattering characteristics at the C-band for both clear and contaminated snow in March 2022 within a region of the Eastern Himalayas in Arunachal Pradesh, India. This analysis integrates data from Sentinel-1 and Landsat-9 to examine and characterize snow contamination, leveraging the synergistic potential of optical and SAR remote sensing techniques. The key outputs from this objective are as follows:

1. Due to persistent cloud cover, Optical remote sensing faces limitations in the Himalayas. Synthetic Aperture Radar (SAR) offers an all-weather alternative to study snow contamination. The study integrated Landsat-9 (multispectral) and Sentinel-1 (C-band SAR) datasets to analyze snow contamination, highlighting the complementary potential of these technologies.
2. SAR backscatter is influenced by snowpack properties (wetness, dielectric constant), contamination, and local incidence angle (LIA). Contaminated snow exhibits higher backscatter compared to clear snow.
3. Clear and contaminated snow in the study region was categorized as wet snow. Contaminated snow showed lower wetness and dielectric constant due to impurities altering snow structure and melting behavior.
4. Contaminated snow has higher surface roughness, increasing SAR backscattering. This is contrasted with the smoother surfaces of clear snow.

5. The Snow Contamination Index (SCI) derived from optical data correlates with SAR backscatter. Positive SCI values indicate non-contaminated snow with a lower backscatter, while negative SCI values denote contaminated snow with a higher backscatter.
6. Surface scattering is dominant for both snow types, with minimal volume scattering due to the wet conditions. Contaminated snow exhibits more scattering variability due to impurities.
7. Multivariate regression revealed that snow wetness/ dielectric properties, LIA, and SCI are key predictors of SAR backscattering. Among these, snow wetness/dielectric constant are the most influential.
8. The study emphasizes developing radar-specific indices for snow contamination and conducting multi-seasonal analyses to understand temporal dynamics better. This would enhance snow monitoring for water resource and climate impact assessments.

Thus, integrating advanced remote sensing technologies highlights significant advancements in estimating snow geophysical parameters (SGPs) such as grain size, dielectric, density, wetness properties, depth, and contamination, addressing challenges posed by complex Northeastern Himalayan terrains. The findings would provide a robust foundation for enhancing disaster risk mitigation, hydrological modeling, and climate engineering strategies, contributing to the sustainable management of snow-fed water resources and ecosystem resilience in climate change.

7.2. Limitations and Future Scope

Key limitations identified in this study that warrant attention in future research include:

1. The lack of comprehensive field measurements hinders detailed validation and limits the model's applicability across diverse terrains and conditions. Thus, testing the models with diverse in-situ datasets from varying geographic and climatic conditions is recommended to ensure broader applicability.
2. The Himalayan terrain presents challenges due to difficult access, extreme weather conditions, and persistent cloud cover, which affect data collection and continuous monitoring. So, the applicability of snow cover monitoring using active microwave datasets should be developed for their continuous monitoring. Deploy automated sensors and drones to overcome challenges in manual data collection in remote and high-altitude regions.
3. Efficiency is affected by the satellite's ascending and descending pass modes, as they

influence scatterer orientation and SAR backscatter analysis.

4. Using medium-resolution DEMs like SRTM (30 arcsec) instead of high-resolution DEMs can limit the precision of topographic corrections and snow depth estimations. Incorporate high-resolution DEMs and finer spatial datasets to improve the precision of topographic corrections and snow depth estimations.
5. SCI correlates with SAR backscatter, but it is derived from optical datasets and lacks the specificity needed, such as contamination concentrations for radar observations, limiting its efficacy. Develop indices tailored for radar observations to enhance the analysis of snow contamination and physical properties. Conduct multi-seasonal and temporal analyses to capture dynamic changes in snow contamination and its impacts over time.
6. Vegetation significantly influences indices such as the Normalized Difference Snow Index (NDSI), leading to inaccuracies in snow cover mapping and requiring terrain-specific threshold adjustments. Additionally, vegetation, soil moisture, and regional climate variables constrain model predictive capabilities, highlighting the need to incorporate these local factors into model development. An open-access database integrating field measurements and satellite data is recommended to enhance predictive accuracy and facilitate collaborative research.
7. The study is confined to a specific time frame, limiting the understanding of snow dynamics across seasons and varying climatic conditions.
8. Combine data from multiple sensors (e.g., L-band SAR, hyperspectral) to leverage complementary strengths for snow property analysis.

References

Abreu, L. W., & Anderson, G. P. (1996). The MODTRAN 2/3 report and LOWTRAN 7 model. Contract, 19628(91-C), 0132.

Achammer, TH., & Denoth, A. (1994). Snow dielectric properties: from DC to microwave X-band. *Annals of Glaciology*, 19, 92–96. doi:10.3189/S0260305500011034

Ambach, W., & Denoth, A. (1980). The dielectric behaviour of snow: a study versus liquid water content. NASA. Goddard Space Flight Center Microwave Remote Sensing of Snowpack Properties.

Anderson, G. P., Berk, A., Chetwynd, J. H., Harder, J., Fontenla, J. M., Shettle, E. P., ... & Acharya, P. K. (2007, May). Using the MODTRAN5 radiative transfer algorithm with NASA satellite data: AIRS and SORCE. In Algorithms and Technologies for Multispectral, Hyperspectral, and Ultraspectral Imagery XIII (Vol. 6565, pp. 590-600). SPIE.

Anilkumar, R., Bharti, R., & Chutia, D. (2022). Point Mass Balance Regression using Deep Neural Networks: A Transfer Learning Approach (No. EGU22-5317). Copernicus Meetings. https://doi.org/10.5194/egusphere-egu22-5317

Armstrong, R. L., & Brun, E. (Eds.). (2008). Snow and climate: physical processes, surface energy exchange and modeling. Cambridge University Press.

Armstrong, R. L., Chang, A., Rango, A., & Josberger, E. (1993). Snow depths and grain- size relationships with relevance for passive microwave studies. *Annals of Glaciology*, *17*, 171-176.

Arslan, A. N., Praks, J., Koskinen, J., & Hallikainen, M. (1999, June). An empirical model for retrieving water equivalent of dry snow from C-band SAR data. In IEEE 1999 International Geoscience and Remote Sensing Symposium. IGARSS'99 (Cat. No. 99CH36293) (Vol. 3, pp. 1789-1791). IEEE.

Avanzi, F., Caruso, M., Jommi, C., De Michele, C., & Ghezzi, A. (2014). Continuous- time monitoring of liquid water content in snowpacks using capacitance probes: A preliminary feasibility study. *Advances in Water Resources*, 68, 32-41.

Awasthi, S., Thakur, P. K., Kumar, S., Kumar, A., Jain, K., & Mani, S. (2020). Snow Density retrieval using Hybrid polarimetric RISAT-1 datasets. IEEE Journal of Selected Topics in Applied Earth Observations and Remote Sensing, 13, 3058-3065.

Awasthi, S., Varade, D., Thakur, P. K., Kumar, A., Singh, H., & Jain, K. (2022). Development of a novel approach for snow wetness estimation using hybrid polarimetric RISAT-1 SAR datasets in North-Western Himalayan region. *Journal of Hydrology*, 612, 128252.

Awasthi, S., & Varade, D. (2021). Recent advances in the remote sensing of alpine snow: A review. GIScience & Remote Sensing, 58(6), 852-888.

Awasthi, S., Kumar, S., Thakur, P. K., Jain, K., Kumar, A., & Snehmani. (2021). Snow depth retrieval in North-Western Himalayan region using pursuit-monostatic TanDEM- X datasets applying polarimetric synthetic aperture radar interferometrybased inversion Modelling. *International Journal of Remote Sensing*, 42(8), 2872-2897.

Awasthi, S., Thakur, P. K., Kumar, S., Kumar, A., Jain, K., & Mani, S. (2020). Snow Density retrieval using Hybrid polarimetric RISAT-1 datasets. IEEE Journal of Selected Topics in Applied Earth Observations and Remote Sensing, 13, 3058-3065. https//doi.org//10.1109/JSTARS.2020.2991156.

Baghdadi, N., Choker, M., Zribi, M., Hajj, M. E., Paloscia, S., Verhoest, Hans, L., Frederic, B., and Francesco, M. (2016). A new empirical model for radar scattering from bare soil surfaces. Remote Sensing, 8(11), 920.

Baghdadi, N., & Zribi, M. (2006). Evaluation of radar backscatter models IEM, OH and Dubois using experimental observations. International Journal of Remote Sensing, 27(18), 3831-3852.

Baghdadi, N., Bernier, M., Gauthier, R., & Neeson, I. (2001). Evaluation of C-band SAR data for wetlands mapping. International Journal of Remote Sensing, 22(1), 71-88.

Baghdadi, N., Gauthier, Y., & Bernier, M. (1997). Capability of multitemporal ERS-1 SAR data for wet-snow mapping. Remote sensing of environment, 60(2), 174-186.

Baldridge, A. M., Hook, S. J., Grove, C. I., & Rivera, G. (2009). The ASTER spectral library version 2.0. Remote sensing of environment, 113(4), 711-715.

Balla, V., & Garg, P. K. (2023, October). Development of spectral characteristics of contaminated snow in Himalayan region. In Earth Resources and Environmental Remote Sensing/GIS Applications XIV (Vol. 12734, pp. 178-185). SPIE.

Ban-Weiss, G. A., McLaughlin, J. P., Harley, R. A., Lunden, M. M., Kirchstetter, T. W., Kean, A. J., ... & Kendall, G. R. (2008). Long-term changes in emissions of nitrogen oxides and particulate matter from on-road gasoline and diesel vehicles. Atmospheric Environment, 42(2), 220-232.

Barnett, T. P., Adam, J. C., & Lettenmaier, D. P. (2005). Potential impacts of a warming climate on water availability in snow-dominated regions. Nature, 438(7066), 303-309.

Basnett, S., Kulkarni, A. V., & Bolch, T. (2013). The influence of debris cover and glacial lakes on the recession of glaciers in Sikkim Himalaya, India. Journal of Glaciology, 59(218), 1035-1046. https://doi.org/10.3189/2013JoG12J184

Basnett, S., Kulkarni, A. V., & Tambe, S. (2012). Monitoring of seasonal snow cover in Sikkim Himalaya using remote sensing techniques. Climate change in Sikkim: patterns, impacts and initiatives. Information and Public Relations Department, Government of Sikkim, Gangtok, 69-80.

Benn, D. I., Bolch, T., Hands, K., Gulley, J., Luckman, A., Nicholson, D. Q., Sarah, T. R., Toumi, and Wiseman, S. (2012). Response of debris-covered glaciers in the Mount Everest region to recent warming, and implications for outburst flood hazards. Earth- Science Reviews, 114(1-2), 156-174.

Bernier, P. Y. (1987). Microwave remote sensing of snowpack properties: potential and limitations. Hydrology Research, 18(1), 1-20.

Bian, J., Li, A., Liu, Q., & Huang, C. (2016). Cloud and snow discrimination for CCD images of HJ-1A/B constellation based on spectral signature and spatio-temporal context. Remote Sensing, 8(1), 31.

Bishop, M. P., Björnsson, H., Haeberli, W., Oerlemans, J., Shroder, J. F., & Tranter, M. (2011). Encyclopedia of snow, ice and glaciers. Springer Science & Business Media.

Blöschl, G. (1999). Scaling issues in snow hydrology. Hydrological processes, 13(14- 15), 2149-2175.

Bohren, C. F. (1987). Multiple scattering of light and some of its observable consequences. Am. J. Phys, 55(6), 524-533.

Bolch, T., Kulkarni, A., Kääb, A., Huggel, C., Paul, F., Cogley, Frey, H., Kargel, J.S., Fujita, K., Scheel, M., Bajracharya, S., Stoffel, M. (2012). The state and fate of Himalayan glaciers. Science, 336(6079), 310-314.

Bousbaa, M., Htitiou, A., Boudhar, A., Eljabiri, Y., Elyoussfi, H., Bouamri, H., Ouatiki, H., and Chehbouni, A. (2022). High-resolution monitoring of the snow cover on the Moroccan Atlas through the spatio-temporal fusion of Landsat and Sentinel-2 images. *Remote Sensing*, 14(22), 5814.

Bradford, J. H., Harper, J. T., & Brown, J. (2009). Complex dielectric permittivity measurements from ground-penetrating radar data to estimate snow liquid water content in the pendular regime. Water resources research, 45(8).

Brangers, I., Marshall, H. P., De Lannoy, G., Dunmire, D., Mätzler, C., & Lievens, H. (2024). Tower-based C-band radar measurements of an alpine snowpack. *The Cryosphere*, 18(7), 3177-3193.

Brucker, L., Picard, G., Arnaud, L., Barnola, J. M., Schneebeli, M., Brunjail, H., Lefebvre, E., and Fily, M., (2011). Modeling time series of microwave brightness temperature at Dome C, Antarctica, using vertically resolved snow temperature and microstructure measurements. Journal of Glaciology, 57(201), 171-182.

Carrivick, J. L., & Tweed, F. S. (2016). A global assessment of the societal impacts of glacier outburst floods. Global and Planetary Change, 144, 1-16.

Casacchia, R., Lauta, F., Salvatori, R., Cagnati, A., Valt, M., & Ørbæk, J. B. (2001). Radiometric investigation of different snow covers in Svalbard. Polar Research, 20(1), 13-22.

Chang, C. I. (1999, June). Spectral information divergence for hyperspectral image analysis. In *IEEE 1999 International Geoscience and Remote Sensing Symposium. IGARSS'99 (Cat. No. 99CH36293)* (Vol. 1, pp. 509-511). IEEE.

Chang, P. S., Mead, J. B., Knapp, E. J., Sadowy, G. A., Davis, R. E., & McIntosh, R. E. (1996). Polarimetric backscatter from fresh and metamorphic snowcover at millimeter wavelengths. IEEE Transactions on Antennas and Propagation, 44(1), 58-73.

Chang, T. C., Gloersen, P., Schmugge, T., Wilheit, T. T., & Zwally, H. J. (1976). Microwave emission from snow and glacier ice. *Journal of Glaciology*, 16(74), 23-39.

Chang, Y., Zhao, L., Shi, L., Nie, Y., Hui, Z., Xiong, Q., & Li, P. (2021). Polarimetric calibration of SAR images using reflection symmetric targets with low helix scattering. *International Journal of Applied Earth Observation and Geoinformation*, 104, 102559.

Chen, C. W., and Zebker, H. A. (2002). “Phase Unwrapping for Large SAR Interferograms: Statistical Segmentation and Generalized Network Models.” IEEE Transactions on Geoscience and Remote Sensing 40 (8): 1709–1719. doi:10.1109/TGRS.2002.802453.

Chen, T., Pan, J., Chang, S., Xiong, C., Shi, J., Liu, M., ... & Liu, H. (2020). Validation of the SNTHERM model applied for snow depth, grain size, and brightness temperature simulation at meteorological stations in China. *Remote Sensing*, 12(3), 507.

Chuvieco, E. (2008). Environmental remote sensing: Earth observation from space. Ariel, Barcelona.

Chýlek, P., Ramaswamy, V., & Srivastava, V. (1983). Albedo of soot-contaminated snow. Journal of Geophysical Research: Oceans, 88(C15), 10837-10843.

Cloude, S. (2009). Polarisation: applications in remote sensing. OUP Oxford.

Cloude, S. R., Fortuny, J., Lopez-Sanchez, J. M., & Sieber, A. J. (1999). Wide-band polarimetric radar inversion studies for vegetation layers. IEEE Transactions on Geoscience and Remote Sensing, 37(5), 2430-2441.

Clough, S. A., Kneizys, F. X., Rothman, L. S., & Gallery, W. O. (1981, July). Atmospheric spectral transmittance and radiance: FASCOD1 B. In Atmospheric transmission (Vol. 277, pp. 152-167). SPIE.
Colbeck, S. C. (1982). An overview of seasonal snow metamorphism. Reviews of Geophysics, 20(1), 45-61.
Colbeck, S. C. (1991). The layered character of snow covers. Reviews of Geophysics, 29(1), 81-96.
Colbeck, S. C. (Ed.). (1985). The international classification for seasonal snow on the ground. Internat. Commission on Snow and Ice of the International Association of Scientific Hydrology.
Crane, R.G., & Anderson, M.R. (1984). Satellite discrimination of snow/cloud surfaces. International Journal of Remote Sensing, 5, pp. 213–223.
Crawford, C. J. (2015). MODIS Terra Collection 6 fractional snow cover validation in mountainous terrain during spring snowmelt using Landsat TM and ETM+. Hydrological Processes, 29(1), 128-138.
Cuffey, K. M., & Paterson, W. S. B. (2010). The physics of glaciers. Academic Press.
Dai, L., & Che, T. (2022). Estimating snow depth or snow water equivalent from space. Sciences in Cold and Arid Regions, 14(2), 79-90.
Dallmann, T. R., Harley, R. A., & Kirchstetter, T. W. (2011). Effects of diesel particle filter retrofits and accelerated fleet turnover on drayage truck emissions at the Port of Oakland. Environmental science & technology, 45(24), 10773-10779.
Danklmayer, A., Doring, B. J., Schwerdt, M., & Chandra, M. (2009). Assessment of atmospheric propagation effects in SAR images. IEEE Transactions on Geoscience and Remote Sensing, 47(10), 3507-3518.
Deems, J. S., Painter, T. H., & Finnegan, D. C. (2013). Lidar measurement of snow depth: a review. Journal of Glaciology, 59(215), 467–479. doi:10.3189/2013JoG12J154
Denoth, A. (1980). The pendular-funicular liquid transition in snow. Journal of Glaciology, 25(91), 93-98.
Denoth, A. (1989). Snow dielectric measurements. Advances in Space Research, 9(1), 233-243.
Denoth, A. (1994). An electronic device for long-term snow wetness recording. Annals of Glaciology, 19, 104–106. doi:10.3189/S0260305500011058
Denoth, A. (2003). Structural phase changes of the liquid water component in Alpine snow. Cold regions science and technology, 37(3), 227-232.
Denoth, A. (1994). "An Electronic Device for Long-term Snow Wetness Recording." Annals of Glaciology 19: 104–106. doi:10.3189/S0260305500011058.
Derksen, C., Walker, A., & Goodison, B. (2003). A comparison of 18 winter seasons of in situ and passive microwave-derived snow water equivalent estimates in Western Canada. Remote Sensing of Environment, 88(3), 271-282.
Di Franco, S., Salzano, R., Boldrini, E., & Salvatori, R. (2022). Increasing the interoperability of snow/ice hyperspectral observations. Computers & Geosciences, 162, 105076.
Dietz, A. J., Kuenzer, C., Gessner, U., & Dech, S. (2012). Remote sensing of snow–a review of available methods. International Journal of Remote Sensing, 33(13), 4094- 4134.

Donahue, C. P., Menounos, B., Viner, N., Skiles, S. M., Beffort, S., Denouden, T.,Gonzalez A. S., White, R., and Heathfield, D., (2023). Bridging the gap between airborne and spaceborne imaging spectroscopy for mountain glacier surface property retrievals. Remote Sensing of Environment, 299, 113849.

Donahue, C., Skiles, S. M., & Hammonds, K. (2021). In situ effective snow grain size mapping using a compact hyperspectral imager. Journal of Glaciology, 67(261), 49-57.

Donahue, C., Skiles, S. M., & Hammonds, K. (2022). Mapping liquid water content in snow at the millimeter scale: an intercomparison of mixed-phase optical property models using hyperspectral imaging and in situ measurements. The Cryosphere, 16(1), 43-59.

Dozier, J. (1989). Spectral signature of alpine snow cover from the Landsat Thematic Mapper. Remote sensing of environment, 28, 9-22.

Dozier, J., & Marks, D. (1987). Snow mapping and classification from Landsat Thematic Mapper data. Annals of Glaciology, 9, 97-103.

Dozier, J., & Painter, T. H. (2004). Multispectral and hyperspectral remote sensing of alpine snow properties. Annu. Rev. Earth Planet. Sci., 32, 465-494. https://doi.org/10.1146/annurev.earth.32.101802.120404

Dozier, J., Green, R. O., Nolin, A. W., & Painter, T. H. (2009). Interpretation of snow properties from imaging spectrometry. Remote Sensing of Environment, 113, S25-S37.

Dozier, J., Schneider, S. R., & McGinnis Jr, D. F. (1981). Effect of grain size and snowpack water equivalence on visible and near-infrared satellite observations of snow. Water Resources Research, 17(4), 1213-1221.

Du, J., Shi, J., & Rott, H., (2010). Comparison between a multi-scattering and multi-layer snow scattering model and its parameterized snow backscattering model. Remote Sensing of Environment, 114(5), 1089-1098. https://doi.org/10.1016/j.rse.2009.12.020.

Dubey, S., & Goyal, M. K. (2020). Glacial lake outburst flood hazard, downstream impact, and risk over the Indian Himalayas. Water Resources Research, 56(4), e2019WR026533.

Dumont, M., & Gascoin, S. (2016). Optical remote sensing of snow cover. In Land surface remote sensing in continental hydrology (pp. 115-137). Elsevier.

Durand, Y., Brun, E., Merindol, L., Guyomarc'h, G., Lesaffre, B., & Martin, E. (1993). A meteorological estimation of relevant parameters for snow models. Annals of glaciology, 18, 65-71.

Dutra, E., Balsamo, G., Viterbo, P., Miranda, P. M., Beljaars, A., Schär, C., & Elder, K. (2010). An improved snow scheme for the ECMWF land surface model: Description and offline validation. Journal of Hydrometeorology, 11(4), 899-916.

Elder, K., Dozier, J., & Michaelsen, J. (1991). Snow accumulation and distribution in an alpine watershed. Water Resources Research, 27(7), 1541-1552.

Elkharrouba, E., Sekertekin, A., Fathi, J., Tounsi, Y., Bioud, H., & Nassim, A. (2022). Surface soil moisture estimation using dual-Polarimetric Stokes parameters and backscattering coefficient. Remote Sensing Applications: Society and Environment, 26, 100737.

Emmer, A., Vilímek, V., Huggel, C., Klimeš, J., & Schaub, Y. (2016). Limits and challenges to compiling and developing a database of glacial lake outburst floods. Landslides, 13(6), 1579-1584.

ESA., (2024). https://sentiwiki.copernicus.eu/web/sentinels-toolboxes#SentinelsToolboxes-Sentinel-1ToolboxGI-S1-Toolbox (accessed October 10, 2020).

Essery, R., Rutter, N., Pomeroy, J., Baxter, R., Stähli, M., Gustafsson, D., Barr, A., Bartlett, P., and Elder, K. (2009). SNOWMIP2: An evaluation of forest snow process simulations. Bulletin of the American Meteorological Society, 90(8), 1120-1136.

Evans, J. R., & Kruse, F. A. (2014). Determination of snow depth using elevation differences determined by interferometric SAR (InSAR). In 2014 IEEE Geoscience and Remote Sensing Symposium (pp. 962-965). IEEE. https//doi.org// 10.1109/IGARSS.2014.6946586.

Evans, S. (1965). Dielectric Properties of Ice and Snow–a Review. Journal of Glaciology, 5(42), 773–792. doi:10.3189/S0022143000018840

F. T. Ulaby, B. Moore, and A. K. Fung, (1982). Microwave Remote Sensing—Active and Passive, Vol. II: Radar Remote Sensing and Surface Scattering and Emission Theory. Norwood, MA: Artech House.

Fair, Z. (2021). Application of Lidar Altimetry and Hyperspectral Imaging to Ice Sheet and Snow Monitoring (Doctoral dissertation).

Fair, Z., Flanner, M., Schneider, A., & Skiles, S. M. (2022). Sensitivity of modeled snow grain size retrievals to solar geometry, snow particle asphericity, and snowpack impurities. The Cryosphere, 16(9), 3801-3814.

Feng, T., Huang, C., Huang, G., Shao, D., & Hao, X. (2024). Estimating snow depth based on dual polarimetric radar index from Sentinel-1 GRD data: A case study in the Scandinavian Mountains. International Journal of Applied Earth Observation and Geoinformation, 130, 103873.

Fierz, C. R. L. A., Armstrong, R. L., Durand, Y., Etchevers, P., Greene, E., McClung, D. M., Nishimura K., Satyawali, P. K., and Sokratov, S.A. (2009). The international classification for seasonal snow on the ground.

Foster, J. L., Hall, D. K., Chang, A. T. C., & Rango, A. (1984). An overview of passive microwave snow research and results. Reviews of Geophysics, 22(2), 195-208.

Frei, A., Tedesco, M., Lee, S., Foster, J., Hall, D. K., Kelly, R., & Robinson, D. A. (2012). A review of global satellite-derived snow products. Advances in Space Research, 50(8), 1007-1029.

Frey, H., Haeberli, W., Linsbauer, A., Huggel, C., & Paul, F. (2010). A multi-level strategy for anticipating future glacier lake formation and associated hazard potentials. Natural Hazards and Earth System Sciences, 10(2), 339-352.

Frolov, A. D., & Ya. Macheret, Y. (1999). On dielectric properties of dry and wet snow. Hydrological processes, 13(12-13), 1755-1760.

Fung, A. K., Tjuatja, S., Beaven, S., Gogineni, S. P., Jezek, K., Gow, A. J., & Perovich, D. K. (1994, August). Modeling interpretation of scattering from snow-covered sea ice. In Proceedings of IGARSS'94-1994 IEEE International Geoscience and Remote Sensing Symposium (Vol. 1, pp. 617-619). IEEE.

Fung, A. K., & Chen, K. S. (2010). Microwave scattering and emission models for users. Artech house.

Gallet, J. C., Domine, F., Zender, C. S., & Picard, G. (2009). Measurement of the specific surface area of snow using infrared reflectance in an integrating sphere at 1310 and 1550 nm. The Cryosphere, 3(2), 167-182.

Gelman, J.C., Ruiz, L., Villarosa, G., Outes, V., Bajano, F. N., He, C., Bajano, H., and Dawidowski, L. (2020). Measurements and modeling of snow albedo at Alerce Glacier, Argentina: effects of volcanic ash, snow grain size, and cloudiness. The Cryosphere, 14(12), 4581-4601.
Gergely, M., Wolfsperger, F., & Schneebeli, M. (2013). Simulation and validation of the InfraSnow: An instrument to measure snow optically equivalent grain size. IEEE transactions on geoscience and remote sensing, 52(7), 4236-4247.
Ghassemian, H. (2016). A review of remote sensing image fusion methods. Information Fusion, 32, 75-89.
Glen, J. W., & Paren, J. G. (1975). The Electrical Properties of Snow and Ice. Journal of Glaciology, 15(73), 15–38. doi:10.3189/S0022143000034249
Graham, L. C. (1974). Synthetic interferometer radar for topographic mapping. Proceedings of the IEEE, 62(6), 763-768.
Green, P. E. (1968). Radar measurements of target scattering properties. Radar astronomy, 1-78.
Grenfell, T. C., & Warren, S. G. (1999). Representation of a nonspherical ice particle by a collection of independent spheres for scattering and absorption of radiation. Journal of Geophysical Research: Atmospheres, 104(D24), 31697-31709.
Grody, N. (2008). Relationship between snow parameters and microwave satellite measurements: Theory compared with Advanced Microwave Sounding Unit observations from 23 to 150 GHz. Journal of Geophysical Research: Atmospheres, 113(D22).
Guneriussen, T., Hogda, K. A., Johnsen, H., & Lauknes, I., 2001. InSAR for estimation of changes in snow water equivalent of dry snow. IEEE Transactions on Geoscience and Remote Sensing, 39(10), 2101-2108. https//doi.org// 10.1109/36.957273.
Gutmann, E. D., Larson, K. M., Williams, M. W., Nievinski, F. G., & Zavorotny, V. (2012). Snow measurement by GPS interferometric reflectometry: an evaluation at Niwot Ridge, Colorado. Hydrological Processes, 26(19), 2951-2961.
Hajnsek I, Pottier E, Cloude SR (2003) Inversion of surface parameters from polarimetric SAR. IEEE Trans Geosci Remote Sens 41(4):727–744.
Hajnsek, I., & Desnos, Y. L. (Eds.). (2021). Polarimetric Synthetic Aperture Radar: Principles and Application (Vol. 25). Springer Nature.
Hall, D. K., Riggs, G. A., Salomonson, V. V., DiGirolamo, N. E., & Bayr, K. J. (2002). MODIS snow-cover products. Remote sensing of Environment, 83(1-2), 181-194.
Hall, D. K., Riggs, G. A., & Salomonson, V. V. (1995). Development of methods for mapping global snow cover using moderate resolution imaging spectroradiometer data. Remote sensing of Environment, 54(2), 127-140.
Hallikainen, M. (1992, May). Review of the microwave dielectric and extinction properties of sea ice and snow. In Proc. IEEE IGARSS (Vol. 2, pp. 961-965).
Hallikainen, M., Ulaby, F., & Abdel-Razik, M. (1982, September). Measurements of the dielectric properties of snow in the 4-18 GHz frequency range. In 1982 12th European Microwave Conference (pp. 151-156). IEEE.
Hallikainen, M., Ulaby, F., & Abdelrazik, M. (1986). Dielectric properties of snow in the 3 to 37 GHz range. IEEE transactions on Antennas and Propagation, 34(11), 1329- 1340.

Hammonds, K., Lieb-Lappen, R., Baker, I., & Wang, X. (2015). Investigating the thermophysical properties of the ice–snow interface under a controlled temperature gradient: Part I: Experiments & Observations. Cold Regions Science and Technology, 120, 157-167.

Hansen, J., & Nazarenko, L. (2004). Soot climate forcing via snow and ice albedos. Proceedings of the national academy of sciences, 101(2), 423-428.

Harder, P., Schirmer, M., Pomeroy, J., & Helgason, W. (2016). Accuracy of snow depth estimation in mountain and prairie environments by an unmanned aerial vehicle. The Cryosphere, 10(6), 2559-2571.

Hazra, P., & Krishna, A. P. (2022). Assessment of Proglacial Lakes in Sikkim Himalaya, India for Glacial Lake Outburst Flood (GLOF) Risk Analysis using HEC-RAS and Geospatial Techniques. Journal of the Geological Society of India, 98(3), 344-352.

He, H., Aogu, K., Li, M., Xu, J., Sheng, W., Jones, S. B., ... & Lv, J. (2021). A review of time domain reflectometry (TDR) applications in porous media. Advances in agronomy, 168, 83-155.

Hellwich, O., and H. Ebner. (2000). "Geocoding SAR Interferograms by Least Squares Adjustment." ISPRS Journal of Photogrammetry and Remote Sensing 55 (4): 277–288. doi:10.1016/S0924- 2716(00)00025-3.

Hernandez-Baquero, E. (2000). Characterization of the Earth's surface and atmosphere for multispectral and hyperspectral thermal imagery.

Hiemstra, C. A., Liston, G. E., & Reiners, W. A. (2006). Observing, modelling, and validating snow redistribution by wind in a Wyoming upper treeline landscape. Ecological Modelling, 197(1-2), 35-51.

Hong, J., Talalay, P., Man, T., Li, Y., Fan, X., Li, C., & Zhang, N. (2022). Effect of high- pressure sintering on snow density evolution: experiments and results. Journal of Glaciology, 68(272), 1107-1115.

Hoppinen, Z., Palomaki, R. T., Brencher, G., Dunmire, D., Gagliano, E., Marziliano, A., Tarricone, J., and Marshall, H. P. (2024). Evaluating snow depth retrievals from Sentinel-1 volume scattering over NASA SnowEx sites. The Cryosphere, 18(11), 5407- 5430.

Huber, S., Younis, M., & Krieger, G. (2010). The TanDEM-X mission: overview and interferometric performance. International Journal of Microwave and Wireless Technologies, 2(3-4), 379-389.

Ignatov, A., & Stowe, L. (2002). Aerosol retrievals from individual AVHRR channels. Part I: Retrieval algorithm and transition from Dave to 6S radiative transfer model. Journal of the Atmospheric Sciences, 59(3), 313-334.

Ismail-Zadeh, A., Castelli, F., Jones, D., & Sanchez, S. (2023). Inverse Problems and Data Assimilation in Earth Sciences. In Application of Data Assimilation and Inverse Problems in Earth Sciences (pp. 3-8). Cambridge University Press.

Jin, Z., Charlock, T. P., Yang, P., Xie, Y., & Miller, W. (2008). Snow optical properties for different particle shapes with application to snow grain size retrieval and MODIS/CERES radiance comparison over Antarctica. Remote Sensing of Environment, 112(9), 3563-3581.

Karamvasis, K., & Karathanassi, V. (2023). Soil moisture estimation from Sentinel-1 interferometric observations over arid regions. Computers & Geosciences, 178, 105410.

Karbou, F., Veyssière, G., Coleou, C., Dufour, A., Gouttevin, I., Durand, P., ... & Grizonnet, M. (2021). Monitoring wet snow over an alpine region using sentinel-1 observations. Remote Sensing, 13(3), 381.

Kendra, J. R., F. T. Ulaby, and K. Sarabandi. (1994). "Snow Probe for in Situ Determination of Wetness and Density." IEEE Transactions on Geoscience and Remote Sensing 32 (6): 1152–1159. doi:10.1109/36.338363.

Keshari, A. K., Satapathy, D. P., & Kumar, A. (2010). The influence of vertical density and velocity distributions on snow avalanche runout. Annals of glaciology, 51(54), 200- 206.

Kinar, N. J., & Pomeroy, J. W. (2015). Measurement of the physical properties of the snowpack. Reviews of Geophysics, 53(2), 481-544.

Kirchner, J. W., Dillon, P. J., & Lazerte, B. D. (1993). Predictability of geochemical buffering and runoff acidification in spatially heterogeneous catchments. Water Resources Research, 29(12), 3891-3901.

Klein, A. And Barnett, A.C., (2003). Validation of daily MODIS snow cover maps of the Upper Rio Grande River Basin for the 2000–2001 snow year. Remote Sensing of Environment, 86, pp. 162–176.

Koike, T., & Suhama, T. (1993). Passive-microwave remote sensing of snow. Annals of Glaciology, 18, 305–308. doi:10.3189/S0260305500011691

Kokhanovsky, A. A., & Zege, E. P. (2004). Scattering optics of snow. Applied optics, 43(7), 1589-1602.

Koskinen, J. T., Palliainen, J. T., Hyyppa, J. M., Engdahl, M. E., & Hallikainen, M. T. (2001). The seasonal behavior of interferometric coherence in boreal forest. IEEE Transactions on Geoscience and Remote Sensing, 39(4), 820-829.

Kozioł, K., Kozak, K., & Polkowska, Ż. (2017). Hydrophobic and hydrophilic properties of pollutants as a factor influencing their redistribution during snowpack melt. Science of the total environment, 596, 158-168.

Krinner, G., Derksen, C., Essery, R., Flanner, M., Hagemann, S., Clark, M., ... & Zhu, D. (2018). ESM-SnowMIP: assessing snow models and quantifying snow-related climate feedbacks. Geoscientific Model Development, 11(12), 5027-5049.

Kumar, S., Narayan, A., & Mehta, D. (2022). Snow cover characterization using C- band polarimetric SAR in parts of the Himalaya. Advances in Space Research, 70(12), 3959-3974.

Landes, T., Gay, M., Trouvé, E., Nicolas, J. M., Bombrun, L., Vasile, G., & Hajnsek, I. (2007, July). Monitoring temperate glaciers by high resolution Pol-InSAR data: First analysis of Argentière E-SAR acquisitions and in-situ measurements. In 2007 IEEE International Geoscience and Remote Sensing Symposium (pp. 184-187). IEEE.

Langlois, A., Royer, A., Montpetit, B., Roy, A., & Durocher, M. (2020). Presenting snow grain size and shape distributions in northern Canada using a new photographic device allowing 2D and 3D representation of snow grains. Frontiers in Earth Science, 7, 347.

Larose, C., Dommergue, A., & Vogel, T. M. (2013). The dynamic arctic snow pack: an unexplored environment for microbial diversity and activity. Biology, 2(1), 317-330.

Lee, J. S., & Pottier, E. (2017). Polarimetric radar imaging: from basics to applications. CRC press.

Lee, J. S., Schuler, D. L., Ainsworth, T. L., Krogager, E., Kasilingam, D., & Boerner, W. M. (2002). On the estimation of radar polarization orientation shifts induced by terrain slopes. IEEE Transactions on Geoscience and Remote Sensing, 40(1), 30-41.

Lehning, M., Fierz, C., Brown, B., & Jamieson, B. (2004). Modeling snow instability with the snow-cover model SNOWPACK. Annals of Glaciology, 38, 331-338.

Lei, Y., Pan, J., Xiong, C., Jiang, L., & Shi, J. (2023). Snow depth and snow cover over the Tibetan Plateau observed from space in against ERA5: matters of scale. Climate Dynamics, 60(5), 1523-1541.

Lei, Y., & Siqueira, P. (2015). An automatic mosaicking algorithm for the generation of a large-scale forest height map using spaceborne repeat-pass InSAR correlation magnitude. Remote Sensing, 7(5), 5639-5659.

Lei, Y., & Siqueira, P. (2015, July). A dense-medium InSAR correlation model with its application to the problem of snow characteristics retrieval. In 2015 IEEE International Geoscience and Remote Sensing Symposium (IGARSS) (pp. 263-266). IEEE.

Lei, Y., & Siqueira, P., (2015). A dense-medium InSAR correlation model with its application to the problem of snow characteristics retrieval. In 2015 IEEE International Geoscience and Remote Sensing Symposium (IGARSS) (pp. 263-266). IEEE. https//doi.org// 10.1109/IGARSS.2015.7325750.

Leinss, S., & Hajnsek, I. (2012, July). Opportunities of snow property extraction based on single and multi pass SAR interferometry: TanDEM-X. In 2012 IEEE International Geoscience and Remote Sensing Symposium (pp. 146-149). IEEE.

Leinss, S., Löwe, H., Proksch, M., Lemmetyinen, J., Wiesmann, A., & Hajnsek, I. (2016). Anisotropy of seasonal snow measured by polarimetric phase differences in radar time series. The Cryosphere, 10(4), 1771-1797.

Leinss, S., Parrella, G., & Hajnsek, I., (2014). Snow height determination by polarimetric phase differences in X-band SAR data. IEEE Journal of Selected Topics in Applied Earth Observations and Remote Sensing, 7(9), 3794-3810. https//doi.org// 10.1109/JSTARS.2014.2323199.

Leinss, S., Wiesmann, A., Lemmetyinen, J., & Hajnsek, I., (2015). Snow water equivalent of dry snow measured by differential interferometry. IEEE Journal of Selected Topics in Applied Earth Observations and Remote Sensing, 8(8), 3773-3790. https//doi.org// 10.1109/JSTARS.2015.2432031.

Lenormand, F., Duguay, C. R., & Gauthier, R., (2002). Development of a historical ice database for the study of climate change in Canada. Hydrological Processes, 16(18), 3707-3722. https//doi.org// https://doi.org/10.1002/hyp.1235.

Leroux, C., & Fily, M. (1998). Modeling the effect of sastrugi on snow reflectance. Journal of Geophysical Research: Planets, 103(E11), 25779-25788.

Li, H., Wang, Z., He, G., & Man, W. (2017). Estimating Snow Depth and Snow Water Equivalence Using Repeat-Pass Interferometric SAR in the Northern Piedmont Region of the Tianshan Mountains. Journal of Sensors, 2017(1), 8739598.

Li, D., Wrzesien, M. L., Durand, M., Adam, J., & Lettenmaier, D. P., (2017). How much runoff originates as snow in the western United States, and how will that change in the future?. Geophysical Research Letters, 44(12), 6163-6172. https://doi.org/10.1002/2017GL073551.

Li, M., Xiao, P., Zhang, X., Feng, X., & Zhu, L. (2022). An improved approach of dry snow density estimation using C-band synthetic aperture radar data. ISPRS Journal of Photogrammetry and Remote Sensing, 191, 49-67.

Lievens, H., Brangers, I., Marshall, H. P., Jonas, T., Olefs, M., & De Lannoy, G. (2022). Sentinel-1 snow depth retrieval at sub-kilometer resolution over the European Alps. The Cryosphere, 16(1), 159-177.

Lievens, H., Demuzere, M., Marshall, H. P., Reichle, R. H., Brucker, L., Brangers, I., ... & De Lannoy, G. J., 2019. Snow depth variability in the Northern Hemisphere mountains observed from space. Nature communications, 10(1), 4629. https://doi.org/10.1038/s41467-019-12566-y.

Liu, H., Wang, L., & Jezek, K. C. (2006). Automated delineation of dry and melt snow zones in Antarctica using active and passive microwave observations from space. IEEE transactions on geoscience and remote sensing, 44(8), 2152-2163.

Liu, J., Wu, Y., & Gao, X. (2021). Increase in occurrence of large glacier-related landslides in the high mountains of Asia. Scientific Reports, 11(1), 1-12.

Liu, W., Wang, H., Xi, Z., Zhang, R., & Huang, X. (2022). Physics-driven deep learning inversion with application to magnetotelluric. Remote Sensing, 14(13), 3218.

Liu, Y., Li, L., Yang, J., Chen, X., & Hao, J., (2017). Estimating snow depth using multi- source data fusion based on the D-InSAR method and 3DVAR fusion algorithm. Remote Sensing, 9(11), 1195. https://doi.org/10.3390/rs9111195.

Long, D., & Ulaby, F. (2015). Microwave radar and radiometric remote sensing. Artech.

Looyenga, H. (1965). Dielectric constants of homogeneous mixture. molecular Physics, 9(6), 501-511.

Luojus, K. P., Pulliainen, J. T., Metsamaki, S. J., & Hallikainen, M. T. (2007). Snow- covered area estimation using satellite radar wide-swath images. IEEE transactions on geoscience and remote sensing, 45(4), 978-989.

Ma, W., Xiao, P., Zhang, X., Song, Y., Ma, T., & Ye, L. (2020). Retrieving snow wetness based on surface and volume scattering simulation. ISPRS Journal of Photogrammetry and Remote Sensing, 169, 17-28.

Madore, J. B., Fierz, C., & Langlois, A. (2022). Investigation into percolation and liquid water content in a multi-layered snow model for wet snow instabilities in Glacier National Park, Canada. Frontiers in Earth Science, 10, 898980.

Mahmoodzada, A. B., Varade, D., & Shimada, S., (2020). Estimation of snow depth in the Hindu Kush Himalayas of Afghanistan during peak winter and early melt season. Remote Sensing, 12(17), 2788. https://doi.org/10.3390/rs12172788.

Main-Knorn, M., Pflug, B., Louis, J., Debaecker, V., Müller-Wilm, U., & Gascon, F. (2017, October). Sen2Cor for sentinel-2. In Image and signal processing for remote sensing XXIII (Vol. 10427, pp. 37-48). SPIE.

Mandal, S., Behera, N., Gangopadhyay, A., Susanto, R. D., & Pandey, P. C. (2021). Evidence of a chlorophyll "tongue" in the Malacca Strait from satellite observations. Journal of Marine Systems, 223, 103610.

Manickam, S., Bhattacharya, A., Singh, G., & Yamaguchi, Y. (2016). Estimation of snow surface dielectric constant from polarimetric SAR data. IEEE Journal of Selected Topics in Applied Earth Observations and Remote Sensing, 10(1), 211-218.

Mantsis, D. F., Bakratsas, M., Andreadis, S., Karsisto, P., Moumtzidou, A., Gialampoukidis, I., ... & Kompatsiaris, I. (2020). Multimodal fusion of sentinel 1 images

and social media data for snow depth estimation. IEEE Geoscience and Remote Sensing Letters, 19, 1-5.
Marks, D., & Dozier, J. (1992). Climate and energy exchange at the snow surface in the alpine region of the Sierra Nevada: 2. Snow cover energy balance. Water Resources Research, 28(11), 3043-3054.
Marks, D., Kimball, J., Tingey, D., & Link, T. (1998). The sensitivity of snowmelt processes to climate conditions and forest cover during rain-on-snow: A case study of the 1996 Pacific Northwest flood. Hydrological Processes, 12(10-11), 1569-1587.
Marpaung, F., Putiamini, S., Fernando, D., Dinanta, G. P., & Nugroho, D. (2019, June). Estimation of Dielectric Constant Using A Dual-pol Sentinel-1A in Tropical Peatland. In IOP Conference Series: Earth and Environmental Science (Vol. 280, No. 1, p. 012030). IOP Publishing.
Marshall, G. J., Dowdeswell, J. A., & Rees, W. G. (1994). The spatial and temporal effect of cloud cover on the acquisition of high-quality Landsat imagery in the European Arctic sector. Remote Sensing of Environment, 50(2), 149-160.
Marshall, S., & Oglesby, R. J. (1994). An improved snow hydrology for GCMs. Part 1: Snow cover fraction, albedo, grain size, and age. Climate Dynamics, 10, 21-37.
Martinec, J., & Rango, A. (1986). Parameter values for snowmelt runoff modelling. Journal of hydrology, 84(3-4), 197-219.
Mascolo, L., Cloude, S. R., & Lopez-Sanchez, J. M. (2021). Model-based decomposition of dual-pol SAR data: Application to Sentinel-1.
Maslanka, W., Sandells, M., Gurney, R., Lemmetyinen, J., Leppänen, L., Kontu, A., ... & Kelly, R. (2019). Derivation and evaluation of a new extinction coefficient for use with the n-HUT snow emission model. IEEE Transactions on Geoscience and Remote Sensing, 57(10), 7406-7417.
Matzl, M., & Schneebeli, M. (2006). Measuring specific surface area of snow by near- infrared photography. Journal of Glaciology, 52(179), 558-564.
Mätzler, C., & Schanda, E. (1984). Snow mapping with active microwave sensors. Remote Sensing, 5(2), 409-422.
Matzler, C., Strozzi, T., Weise, T., Floricioiu, D. M., & Rott, H. (1997). Microwave snowpack studies made in the Austrian Alps during the SIR-C/X-SAR experiment. International Journal of Remote Sensing, 18(12), 2505-2530.
Mccreight, J. L., & Small, E. E. (2013). Modeling bulk density and snow water equivalent using daily snow depth observations. The Cryosphere Discussions, 7(5), 5007-5049.
Meehan, T. G., Hojatimalekshah, A., Marshall, H. P., Deeb, E. J., O'Neel, S., McGrath, D., ... & Elder, K. (2023). Spatially distributed snow depth, bulk density, and snow water equivalent from ground-based and airborne sensor integration at Grand Mesa, Colorado, USA. The Cryosphere Discussions, 2023, 1-45.
Meier, M. F. (1975). Application of remote-sensing techniques to the study of seasonal snow cover. *Journal of Glaciology*, *15*(73), 251–265. doi:10.3189/S0022143000034419
Mellor, M. (1977). Engineering properties of snow. Journal of Glaciology, 19(81), 15-66.
Meløysund, V., Leira, B., Høiseth, K. V., & Lisø, K. R. (2007). Predicting snow density using meteorological data. Meteorological Applications: A journal of forecasting, practical applications, training techniques and modelling, 14(4), 413-423.

Mitterer, C., & Schweizer, J. (2013). Analysis of the snow-atmosphere energy balance during wet-snow instabilities and implications for avalanche prediction. The Cryosphere, 7(1), 205-216.
Montpetit, B., Royer, A., Roy, A., Langlois, A., & Derksen, C. (2013). Snow microwave emission modeling of ice lenses within a snowpack using the microwave emission model for layered snowpacks. IEEE Transactions on Geoscience and Remote Sensing, 51(9), 4705-4717.
Moskolaï, W. R., Abdou, W., Dipanda, A., & Kolyang. (2022). A workflow for collecting and preprocessing Sentinel-1 images for time series prediction suitable for deep learning algorithms. Geomatics, 2(4), 435-456.
Nagler, T., Rott, H., Ripper, E., Bippus, G., & Hetzenecker, M. (2016). Advancements for snowmelt monitoring by means of Sentinel-1 SAR. Remote Sensing, 8(4), 348.
Nagler, T. (1996). Methods and analysis of synthetic aperture radar data from ERS-1 and X-SAR for snow and glacier applications (Doctoral dissertation, Leopold-Franzens- Universität Innsbruck).
Nagler, T., & Rott, H. (2000). Retrieval of wet snow by means of multitemporal SAR data. IEEE Transactions on Geoscience and Remote Sensing, 38(2), 754-765.
Nagler, T., Rott, H., & Glendinning, G. (1998). SAR-based snow cover retrievals for runoff modelling. EUROPEAN SPACE AGENCY-PUBLICATIONS-ESA SP, 441, 511- 518.
Nagler, T., Rott, H., Ripper, E., Bippus, G., & Hetzenecker, M. (2016). Advancements for snowmelt monitoring by means of Sentinel-1 SAR. Remote Sensing, 8(4), 348.
Nandan, V., Geldsetzer, T., Mahmud, M., Yackel, J., & Ramjan, S. (2017). Ku-, X-and C-Band Microwave Backscatter Indices from Saline Snow Covers on Arctic First-Year Sea Ice. Remote Sensing, 9(7), 757.
Nasim, S., Oussalah, M., Klöve, B., & Haghighi, A. T. (2022). Machine learning model for snow depth estimation using a multisensory ubiquitous platform. *Journal of Mountain Science, 19*(9), 2506-2527.
Nazarenko, Y., Kurien, U., Nepotchatykh, O., Rangel-Alvarado, R. B., & Ariya, P. A. (2016). Role of snow and cold environment in the fate and effects of nanoparticles and select organic pollutants from gasoline engine exhaust. Environmental Science: Processes & Impacts, 18(2), 190-199.
Negi, H. S., & Kokhanovsky, A. (2011). Retrieval of snow albedo and grain size using reflectance measurements in Himalayan basin. The Cryosphere, 5(1), 203-217.
Negi, H. S., Kulkarni, A. V., & Singh, S. K. (2006, December). Effect of contamination and mixed objects on snow reflectance using spectroradiometer in Beas Basin, India. In Agriculture and Hydrology Applications of Remote Sensing (Vol. 6411, pp. 228-239). SPIE.
Negi, H. S., Shekhar, C., & Singh, S. K. (2015). Snow and glacier investigations using hyperspectral data in the Himalaya. Current Science, 892-902.
Negi, H. S., Singh, S. K., Kulkarni, A. V., & Semwal, B. S. (2010). Field-based spectral reflectance measurements of seasonal snow cover in the Indian Himalaya. International Journal of Remote Sensing, 31(9), 2393-2417.
Nghiem, S. V., Yueh, S. H., Kwok, R., & Li, F. K. (1992). Symmetry properties in polarimetric remote sensing. Radio Science, 27(05), 693-711.

Nolin, A. W. (2010). Recent advances in remote sensing of seasonal snow. Journal of Glaciology, 56(200), 1141–1150. doi:10.3189/002214311796406077

Nolin, A. W., & Dozier, J. (1993). Estimating snow grain size using AVIRIS data. Remote sensing of environment, 44(2-3), 231-238.

Nolin, A. W., & Dozier, J. (2000). A hyperspectral method for remotely sensing the grain size of snow. Remote sensing of Environment, 74(2), 207-216.

Notarnicola, C., Ratti, R., Maddalena, V., Schellenberger, T., Ventura, B., & Zebisch, M. (2012). Seasonal snow cover mapping in alpine areas through time series of COSMO-skymed images. IEEE Geoscience and Remote Sensing Letters, 10(4), 716-720.

O'Grady, D., Leblanc, M., & Gillieson, D. (2013). Relationship of local incidence angle with satellite radar backscatter for different surface conditions. International journal of applied earth observation and geoinformation, 24, 42-53.

Painter, T. H., Molotch, N. P., Cassidy, M., Flanner, M., & Steffen, K. (2007). Contact spectroscopy for determination of stratigraphy of snow optical grain size. Journal of Glaciology, 53(180), 121-127.

Painter, T. H., Seidel, F. C., Bryant, A. C., McKenzie Skiles, S., & Rittger, K. (2013). Imaging spectroscopy of albedo and radiative forcing by light-absorbing impurities in mountain snow. Journal of Geophysical Research: Atmospheres, 118(17), 9511-9523.

Panda, S., Anilkumar, R., Balabantaray, B. K., Chutia, D., & Bharti, R., (2022). Machine Learning-Driven Snow Cover Mapping Techniques using Google Earth Engine. In 2022 IEEE 19th India Council International Conference (INDICON) (pp. 1-6). IEEE. https//doi.org// 10.1109/INDICON56171.2022.10040153.

Pandit, V. R., & Bhiwani, R. J. (2015). Image fusion in remote sensing applications: A review. International journal of computer applications, 120(10).

Parmentier, T. R. (2024). An investigation on the development of liquid water content in different snow types during slushflow-inducing weather conditions (Master's thesis, The University of Bergen).

Patel, P., Mondal, S. K., & Bharti, R. (2019, July). Snow Area Mapping using Feature- oriented Principal Component Analysis. In IGARSS 2019-2019 IEEE International Geoscience and Remote Sensing Symposium (pp. 4088-4090). IEEE.

Patel, V. D., & Bharti, R. (2022, July). Mass Balance Assessment of Zemu Glacier: An ELA-AAR Based Approach. In IGARSS 2022-2022 IEEE International Geoscience and Remote Sensing Symposium (pp. 3963-3966). IEEE.

Pathe, C., Wagner, W., Sabel, D., Doubkova, M., & Basara, J. B. (2009). Using ENVISAT ASAR global mode data for surface soil moisture retrieval over Oklahoma, USA. IEEE Transactions on Geoscience and Remote Sensing, 47(2), 468-480.

Patil A, Singh G, Rüdiger C, Mohanty S, Kumar S (2020) A novel approach for the snow water equivalent retrieval using X-band polarimetric synthetic aperture radar data. IEEE Trans Geosci Remote Sens 59(5):3753–3763.

Patil, A., Singh, G., & Rüdiger, C., (2020). Retrieval of snow depth and snow water equivalent using dual polarization SAR data. Remote Sensing, 12(7), 1183. https://doi.org/10.3390/rs12071183.

Petzold, A., & Schönlinner, M. (2004). Multi-angle absorption photometry—a new method for the measurement of aerosol light absorption and atmospheric black carbon. Journal of Aerosol Science, 35(4), 421-441.

Pielmeier, C., & Schneebeli, M. (2003). Developments in the stratigraphy of snow. Surveys in geophysics, 24, 389-416.

Ponnurangam, G. G., Jagdhuber, T., Hajnsek, I., & Rao, Y. S. (2015). Soil moisture estimation using hybrid polarimetric SAR data of RISAT-1. IEEE Transactions on Geoscience and Remote Sensing, 54(4), 2033-2049.

Principles, I. (2007). Guidelines for SAR Interferometry Processing and Interpretation. Ferretti, A. Monti-Guarnieri, C. Rrati C., F. Rossa. ESA Publication.

Pulliainen, J. T., Heiska, K., Hyyppa, J., & Hallikainen, M. T. (1994). Backscattering properties of boreal forests at the C-and X-bands. IEEE Transactions on Geoscience and Remote Sensing, 32(5), 1041-1050.

Pulliainen, J. T., Mikhela, P. J., Hallikainen, M. T., & Ikonen, J. P. (1996). Seasonal dynamics of C-band backscatter of boreal forests with applications to biomass and soil moisture estimation. IEEE Transactions on Geoscience and Remote Sensing, 34(3), 758- 770.

Quéno, L., Mott, R., Morin, P., Cluzet, B., Mazzotti, G., & Jonas, T. (2023). Snow redistribution in an intermediate-complexity snow hydrology modelling framework. EGUsphere, 2023, 1-32.

Quincey, D. J., Richardson, S. D., Luckman, A., Lucas, R. M., Reynolds, J. M., Hambrey, M. J., & Glasser, N. F. (2007). Early recognition of glacial lake hazards in the Himalaya using remote sensing datasets. Global and Planetary Change, 56(1-2), 137-152.

Ramanathan, V., & Carmichael, G. (2008). Global and regional climate changes due to black carbon. Nature geoscience, 1(4), 221-227.

Raney, R. K. (2006). Dual-polarized SAR and stokes parameters. IEEE Geoscience and Remote Sensing Letters, 3(3), 317-319.

Raney, R. K. (2019). Hybrid dual-polarization synthetic aperture radar. Remote Sensing, 11(13), 1521.

Ranganathan, M., & Minchew, B. (2024). A modified viscous flow law for natural glacier ice: Scaling from laboratories to ice sheets. Proceedings of the National Academy of Sciences, 121(23), e2309788121.

Ravasio, C., Garzonio, R., Di Mauro, B., Matta, E., Giardino, C., Pepe, M., Cremonese, E., Pogliotti, P., Marin, C. and Colombo, R. (2024). Retrieval of snow liquid water content from radiative transfer model, field data and PRISMA satellite data. Remote Sensing of Environment, 311, 114268.

Rawat, D. (2023). Current Scenario of Sikkim Glacial Lake Outburst Flood (GLOF).

Rees, W. G. (2005). Remote sensing of snow and ice. CRC press.

Reistad, J. (2018). A compact portable resonance probe system for in situ measurements of snow conditions (Master's thesis, UiT Norges arktiske universitet).

Richardson, S. D., & Reynolds, J. M. (2000). An overview of glacial hazards in the Himalayas. Quaternary International, 65, 31-47.

Riche, F., Montagnat, M., & Schneebeli, M. (2013). Evolution of crystal orientation in snow during temperature gradient metamorphism. Journal of Glaciology, 59(213), 47- 55.

Rott, H., Nagler, T., & Scheiber, R. (2003, December). Snow mass retrieval by means of SAR interferometry. In 3rd FRINGE Workshop, European Space Agency, Earth Observation (pp. 1-6).

Rücker, A., Boss, S., Kirchner, J. W., & von Freyberg, J. (2019). Monitoring snowpack outflow volumes and their isotopic composition to better understand streamflow generation during rain-on-snow events. Hydrology and Earth System Sciences, 23(7), 2983-3005.

Saberi, N., Kelly, R., Flemming, M., & Li, Q. (2020). Review of snow water equivalent retrieval methods using spaceborne passive microwave radiometry. International Journal of Remote Sensing, 41(3), 996-1018.

Sadeghi, M., Babaeian, E., Tuller, M., & Jones, S. B. (2017). The optical trapezoid model: A novel approach to remote sensing of soil moisture applied to Sentinel-2 and Landsat-8 observations. Remote sensing of environment, 198, 52-68.

Sánchez-Gámez, P., & Navarro, F. J., 2017. Glacier surface velocity retrieval using D- InSAR and offset tracking techniques applied to ascending and descending passes of Sentinel-1 data for southern Ellesmere ice caps, Canadian Arctic. Remote Sensing, 9(5), 442. https://doi.org/10.3390/rs9050442.

Schneebeli, M., Coléou, C., Touvier, F., & Lesaffre, B. (1998). Measurement of density and wetness in snow using time-domain reflectometry. Annals of Glaciology, 26, 69–72. doi:10.3189/1998AoG26-1-69-72

Schuler, D. L., Lee, J. S., Kasilingam, D., & Nesti, G. (2002). Surface roughness and slope measurements using polarimetric SAR data. IEEE Transactions on Geoscience and Remote Sensing, 40(3), 687-698.

Schweizer, J., Bruce Jamieson, J., & Schneebeli, M. (2003). Snow avalanche formation. *Reviews of Geophysics*, *41*(4).

Sharma, R. K., Pradhan, P., Sharma, N. P., & Shrestha, D. G. (2018). Remote sensing and in situ-based assessment of rapidly growing South Lhonak glacial lake in eastern Himalaya, India. Natural Hazards, 93, 393-409.

Shea, J. M., Whitfield, P. H., Fang, X., & Pomeroy, J. W. (2021). The role of basin geometry in mountain snowpack responses to climate change. Frontiers in Water, 3, 604275.

Shekhar, C., Srivastava, S., Negi, H. S., & Dwivedi, M. (2019). Hyper-spectral data based investigations for snow wetness mapping. Geocarto International, 34(6), 664-687.

Shi, J., & Dozier, J. (1995). Inferring snow wetness using C-band data from SIR-C's polarimetric synthetic aperture radar. IEEE transactions on geoscience and remote sensing, 33(4), 905-914.

Shi, J., & Dozier, J. (1997). Mapping seasonal snow with SIR-C/X-SAR in mountainous areas. Remote Sensing of Environment, 59(2), 294-307.

Shi, J., & Dozier, J. (2000). Estimation of snow water equivalence using SIR-C/X-SAR. II. Inferring snow depth and particle size. IEEE Transactions on Geoscience and Remote sensing, 38(6), 2475-2488.

Shi, J., S. Hensley, and J. Dozier. (2000). "Mapping Snow with Repeat Pass Synthetic Aperture Radar." Geosci Remote Sensing, 1997 IGARSS '97 Remote Sens - A Sci Vis Sustain Dev 1997 IEEE Int 2000 (267): 339–342.

Shi, J., Xiong, C., & Jiang, L. (2016). Review of snow water equivalent microwave remote sensing. Science China Earth Sciences, 59(4), 731-745.

Sihvola, A., & Tiuri, M. (1986). Snow fork for field determination of the density and wetness profiles of a snow pack. IEEE Transactions on Geoscience and Remote Sensing, (5), 717-721.

Singh, G., & Venkataraman, G. (2009, July). Snow density estimation using Polarimitric ASAR data. In 2009 IEEE International Geoscience and Remote Sensing Symposium (Vol. 2, pp. II-630). IEEE.

Singh, G., & Venkataraman, G. (2010). Snow permittivity retrieval inversion algorithm for estimating snow wetness. Geocarto International, 25(3), 187-212.

Singh, G., Kumar, V., Mohite, K., Venkatraman, G., & Rao, Y. S. (2006, December). Snow wetness estimation in Himalayan snow-covered regions using ENVISAT-ASAR data. In Microwave Remote Sensing of the Atmosphere and Environment V (Vol. 6410, pp. 67-78). SPIE.

Singh, G., Venkataraman, G., Rao, Y. S., & Kumar, V., (2008). InSAR coherence measurement techniques for snow cover mapping in Himalayan region. In IGARSS 2008-2008 IEEE International Geoscience and Remote Sensing Symposium (Vol. 4, pp. IV-1077). IEEE. https//doi.org// 10.1109/IGARSS.2008.4779913.

Singh, G., Venkataraman, G., Yamaguchi, Y., & Park, S. E. (2013). Capability assessment of fully polarimetric ALOS–PALSAR data for discriminating wet snow from other scattering types in mountainous regions. IEEE transactions on geoscience and remote sensing, 52(2), 1177-1196.

Singh, G., Verma, A., Kumar, S., Ganju, A., Yamaguchi, Y., & Kulkarni, A. V. (2017). Snowpack density retrieval using fully polarimetric TerraSAR-X data in the Himalayas. IEEE Transactions on Geoscience and Remote Sensing, 55(11), 6320-6329.

Singh, H., Rawat, M., Varade, D., & Awasthi, S. (2022). Assessment of PRISMA hyperspectral data for the retrieval of qualitative snow grain size. In International Symposium on Remote Sensing (pp. 16-18).

Snehmani, Venkataraman, G., Nigam, A. K., & Singh, G. (2010). Development of an inversion algorithm for dry snow density estimation and its application with ENVISAT- ASAR dual co-polarization data. Geocarto International, 25(8), 597-616.

Song, C., Woodcock, C. E., Seto, K. C., Lenney, M. P., & Macomber, S. A. (2001). Classification and change detection using Landsat TM data: when and how to correct atmospheric effects? Remote Sensing of Environment, 75(2), 230-244.

Staenz, K., & Haefner, H. (1981). Spectral reflectance properties of snow in the Landsat MSS bands. Canadian Journal of Remote Sensing, 7(1), 41-50.

Stiles, W. H., & Ulaby, F. T. (1980). The active and passive microwave response to snow parameters: 1. Wetness. Journal of Geophysical Research: Oceans, 85(C2), 1037- 1044.

Stiles, W. H., Ulaby, F. T., & Rango, A. (1981). Microwave measurements of snowpack properties. Hydrology Research, 12(3), 143-166.

Stokes, G. G. (1851). On the composition and resolution of streams of polarized light from different sources. Transactions of the Cambridge Philosophical Society, 9, 399.

Strozzi, T., Klimeš, J., Frey, H., Caduff, R., Huggel, C., Wegmüller, U., & Rapre, A. C., (2018). Satellite SAR interferometry for the improved assessment of the state of activity of landslides: A case study from the Cordilleras of Peru. Remote sensing of environment, 217, 111-125. https://doi.org/10.1016/j.rse.2018.08.014.

Strozzi, T., Wiesmann, A., & Mätzler, C. (1997). Active microwave signatures of snow covers at 5.3 and 35 GHz. Radio Science, 32(2), 479-495.

Sturm, M. (2015). White water: Fifty years of snow research in WRR and the outlook for the future. Water Resources Research, 51(7), 4948-4965.

Sturm, M., Taras, B., Liston, G. E., Derksen, C., Jonas, T., & Lea, J. (2010). Estimating snow water equivalent using snow depth data and climate classes. Journal of Hydrometeorology, 11(6), 1380-1394.

Su, H., Cao, B., Zhong, X., Hu, Y., Zheng, L., & Zhang, T. (2022). Comparison of Snow Density Measurements Using Different Methods. Available at SSRN 4659335.

Surendar, M., Bhattacharya, A., Singh, G., & Venkataraman, G. (2015). Estimation of snow density using full-polarimetric synthetic aperture radar (SAR) data. Physics and Chemistry of the Earth, Parts A/B/C, 83, 156-165.

Taheri, M., & Mohammadian, A. (2022). An overview of snow water equivalent: Methods, challenges, and future outlook. Sustainability, 14(18), 11395.

Takeuchi, N. (2009). Temporal and spatial variations in spectral reflectance and characteristics of surface dust on Gulkana Glacier, Alaska Range. Journal of Glaciology, 55(192), 701-709.

Tang, X. G., Liu, D. W., Zhang, B., Du, J., Lei, X. C., Zeng, L. H., Wang, Y.D. and Song, K.S. (2011). Research on hyperspectral remote sensing in monitoring snow contamination concentration. Spectroscopy and Spectral Analysis, 31(5), 1318-1321.

Tanikawa, T., Aoki, T., & Nishio, F. (2002). Remote sensing of snow grain-size and impurities from Airborne Multispectral Scanner data using a snow bidirectional reflectance distribution function model. Annals of Glaciology, 34, 74-80.

Thakur, P. K., Aggarwal, S. P., Arun, G., Sood, S., Senthil Kumar, A., Mani, S., & Dobhal, D. P. (2017). Estimation of snow cover area, snow physical properties and glacier classification in parts of Western Himalayas using C-Band SAR Data. Journal of the Indian Society of Remote Sensing, 45, 525-539.

Thakur, P. K., Aggarwal, S. P., Garg, P. K., Garg, R. D., Mani, S., Pandit, A., & Kumar, S. (2012). Snow physical parameters estimation using space-based Synthetic Aperture Radar. Geocarto International, 27(3), 263-288.

Thakur, P. K., Garg, R. D., Aggarwal, S. P., Garg, P. K., & Shi, J., (2013). Snow density retrieval using SAR data: algorithm validation and applications in part of North Western Himalaya. The Cryosphere Discussions, 7(3), 1927-1960. https://doi.org/10.5194/tcd-7- 1927-2013, 2013.

Thomas, G. E., & Stamnes, K. (2002). Radiative transfer in the atmosphere and ocean. Cambridge University Press.

Tiuri, M., Sihvola, A., Nyfors, E. G., & Hallikaiken, M., (1984). The complex dielectric constant of snow at microwave frequencies. IEEE Journal of oceanic Engineering, 9(5), 377-382. https//doi.org// 10.1109/JOE.1984.1145645.

Tsai, Y. L. S., Dietz, A., Oppelt, N., & Kuenzer, C. (2019). Remote sensing of snow cover using spaceborne SAR: A review. Remote Sensing, 11(12), 1456.

Tsang, L., Liang, D., Xu, X., & Xu, P. (2008, March). Microwave emission from snowpacks: modeling the effects of volume scattering, surface scattering and layering. In 2008 Microwave Radiometry and Remote Sensing of the Environment (pp. 1-4). IEEE.

Ulaby, F. T., & Stiles, W. H. (1981). Microwave response of snow. Advances in Space Research, 1(10), 131-149.

Ulaby, F. T., Kouyate, F., Fung, A. K., & Sieber, A. J. (1982). A backscatter model for a randomly perturbed periodic surface. IEEE Transactions on Geoscience and Remote Sensing, (4), 518-528.

Ulaby, F. T., Moore, R. K., & Fung, A. K. (1986). Microwave Remote Sensing Active and Passive, Artech House. Inc., Addison-Wesley, Reading, MA.
Ulaby, F. T., Stiles, W. H., Dellwig, L. F., & Hanson, B. C. (1977). Experiments on the radar backscatter of snow. IEEE Transactions on Geoscience Electronics, 15(4), 185-189.https//doi.org// 10.1109/TGE.1977.294490.
Varade D, Dikshit O, Manickam S (2019) Dry/wet snow mapping based on the synergistic use of dual polarimetric SAR and multispectral data. J Mt Sci 16(6):1435– 1451.
Varade, D., & Dikshit, O. (2018). Estimation of surface snow wetness using Sentinel-2 multispectral data. ISPRS Annals of the Photogrammetry, Remote Sensing and Spatial Information Sciences, 4, 223-228.
Varade, D., & Dikshit, O. (2019). Improved assessment of atmospheric water vapor content in the Himalayan regions around the Kullu valley in India using Landsat-8 data. Water Resources Research, 55(1), 462-475.
Varade, D., & Dikshit, O. (2020). Potential of multispectral reflectance for assessment of snow geophysical parameters in Solang valley in the lower Indian Himalayas. GIScience & Remote Sensing, 57(1), 107-126.
Varade, D., Dikshit, O., Manickam, S., & Singh, G., (2019). Capability assessment of Sentinel-1 bi-temporal dual polarimetric SAR data for inferences on snow density. In 2019 IEEE MTT-S International Microwave and RF Conference (IMARC) (pp. 1-5). IEEE. https//doi.org// 10.1109/IMaRC45935.2019.9118717.
Varade, D., Manickam, S., Dikshit, O., & Singh, G. (2020). Modelling of early winter snow density using fully polarimetric C-band SAR data in the Indian Himalayas. Remote sensing of environment, 240, 111699
Varade, D., Maurya, A. K., Dikshit, O., Singh, G., & Manickam, S. (2020). Snow depth in Dhundi: An estimate based on weighted bias corrected differential phase observations of dual polarimetric bi-temporal Sentinel-1 data. International Journal of Remote Sensing, 41(8), 3031-3053.
Varade, D., Sure, A., & Dikshit, O. (2019). Potential of Landsat-8 and Sentinel-2A composite for land use land cover analysis. Geocarto International, 34(14), 1552-1567.
Vilímek, V., Emmer, A., Huggel, C., Schaub, Y., & Würmli, S. (2014). Database of glacial lake outburst floods (GLOFs)–IPL project No. 179. Landslides, 11(1), 161-165.
Wang, S., Yang, B., Zhou, Y., Wang, F., Zhang, R., & Zhao, Q., (2018). Snow cover mapping and ice avalanche monitoring from the satellite data of the sentinels. The International Archives of the Photogrammetry, Remote Sensing and Spatial Information Sciences, 42, 1765-1772. https://doi.org/10.5194/isprs-archives-XLII-3-1765-2018.
Warren, S. G. (1982). Optical properties of snow. Reviews of Geophysics, 20(1), 67- 89.
Warren, S. G., & Wiscombe, W. J. (1980). A model for the spectral albedo of snow. II: Snow containing atmospheric aerosols. Journal of the Atmospheric Sciences, 37(12), 2734-2745.
West, R. D. (2000). Potential applications of 1–5 GHz radar backscatter measurements of seasonal land snow cover. Radio Science, 35(4), 967-981.
Wilder, B. A., Meyer, J., Enterkine, J., & Glenn, N. F. (2024). Improved snow property retrievals by solving for topography in the inversion of at-sensor radiance measurements. The Cryosphere, 18(11), 5015-5029.

Winther, J. G., Bruland, O., Sand, K., Gerland, S., Marechal, D., Ivanov, B., ... & König, M. (2003). Snow research in Svalbard—an overview. Polar research, 22(2), 125-144.

Wiscombe, W. J., & Warren, S. G. (1980). A model for the spectral albedo of snow. I: Pure snow. Journal of the Atmospheric Sciences, 37(12), 2712-2733.

Wolf, E. (1954). Optics in terms of observable quantities. Il Nuovo Cimento (1943- 1954), 12(6), 884-888.

Worni, R., Huggel, C., & Stoffel, M. (2013). Glacial lakes in the Indian Himalayas— From an area-wide glacial lake inventory to on-site and modeling based risk assessment of critical glacial lakes. Science of the Total Environment, 468, S71-S84.

Worni, R., Stoffel, M., Huggel, C., Volz, C., Casteller, A., & Luckman, B. (2012). Analysis and dynamic modeling of a moraine failure and glacier lake outburst flood at Ventisquero Negro, Patagonian Andes (Argentina). Journal of Hydrology, 444, 134-145.

Xiao, E., Li, S., Matin Nazar, A., Zhu, R., & Wang, Y. (2024). Antarctic Snow Failure Mechanics: Analysis, Simulations, and Applications. Materials, 17(7), 1490.

Xiao, X., Shen, Z., & Qin, X. (2001). Assessing the potential of VEGETATION sensor data for mapping snow and ice cover: a Normalized Difference Snow and Ice Index. International Journal of Remote Sensing, 22(13), 2479-2487.

Xu, C., Chen, Y., Hamid, Y., Tashpolat, T., Chen, Y., Ge, H., & Li, W. (2009). Long- term change of seasonal snow cover and its effects on river runoff in the Tarim River basin, northwestern China. Hydrological Processes: An International Journal, 23(14), 2045-2055.

Yang, J., Jiang, L., Luojus, K., Pan, J., Lemmetyinen, J., Takala, M., & Wu, S. (2020). Snow depth estimation and historical data reconstruction over China based on a random forest machine learning approach. The Cryosphere, 14(6), 1763-1778.

Yin, F., Gomez-Dans, J., Lewis, P., & Lopez-Saldana, G. (2019, January). The Sensor Independent Atmospheric Correction (SIAC) approach applied to Sentinel-2 and Landsat- 8 data. In Geophysical Research Abstracts (Vol. 21).

Yu, C., Li, Z., Penna, N. T., & Crippa, P., (2018). Generic atmospheric correction model for interferometric synthetic aperture radar observations. Journal of Geophysical Research: Solid Earth, 123(10), 9202-9222. https://doi.org/10.1029/2017JB015305.

Yueh, S. H., Dinardo, S. J., Akgiray, A., West, R., Cline, D. W., & Elder, K. (2009). Airborne Ku-band polarimetric radar remote sensing of terrestrial snow cover. IEEE Transactions on Geoscience and Remote Sensing, 47(10), 3347-3364.

Zhang, T. (2005). Influence of the seasonal snow cover on the ground thermal regime: An overview. Reviews of Geophysics, 43(4).

Zhuravleva, T. B., & Kokhanovsky, A. A. (2011). Influence of surface roughness on the reflective properties of snow. Journal of Quantitative Spectroscopy and Radiative Transfer, 112(8), 1353-1368.

Zink, M., Fiedler, H., Hajnsek, I., Krieger, G., Moreira, A., & Werner, M., (2006). The TanDEM-X mission concept. In 2006 IEEE International Symposium on Geoscience and Remote Sensing (pp. 1938-1941). IEEE. https//doi.org// 10.1109/IGARSS.2006.501.

Zuanon, N. (2013, October). IceCube, a portable and reliable instruments for snow specific surface area measurement in the field. In International Snow Science Workshop Grenoble-Chamonix Mont-Blance-2013 proceedings (pp. 1020-1023).

List of Publications:

Research articles published:

1. Singh, M. K., & Bharti, R. (2023). Inversion model for snow geophysical parameters estimation using sentinel–1 stokes parameter. Earth Science Informatics, 16(2), 1585-1595. https://doi.org/10.1007/s12145-023-00984-y
2. Singh, M. K., Anilkumar, R., & Bharti, R. (2025). Study of contaminated snow cover using remote sensing in the Eastern Himalayas of Arunachal Pradesh, India. Environmental Monitoring and Assessment, 197(1), 1-17. https://doi.org/10.1007/s10661-024-13476-3
3. Singh, M. K., Anilkumar, R., & Bharti, R. (2025). A novel snow depth estimation model for the Eastern Himalayas using DInSAR. Advances in Space Research. https://doi.org/10.1016/j.asr.2025.03.059

Research articles under review:

4. Singh, M. K., & Bharti, R., Recent advances in the snow geophysical inversion model using remote sensing: A Review.

National and International Conferences:

1. Singh, M. K., & Bharti, R. (2022, July). Snow permittivity and density estimation using C- band dual polarimetric sentinel-1A data. In IGARSS 2022-2022 IEEE International Geoscience and Remote Sensing Symposium (pp. 2526-2529). IEEE. 10.1109/IGARSS46834.2022.9884072(Oral Presentation)
2. Manmit Kumar Singh, Bhawana, And Rishikesh Bharti (2023 November). Effective Snow Cover Mapping for Rathong Glacier Region Using Sentinel-2 Dataset. In National Conference on Himalayan Cryosphere22-23, November 2023, DST-Centre for Excellence in climate change, Indian Institute of Science (Oral Presentation).
3. Singh, M. K., Mondal, S. K., & Bharti, R. (2024). South Lhonak Glacial System: Cascade Investigation Using Satellite Remote Sensing (No. EGU24-18788). Copernicus Meetings. https://doi.org/10.5194/egusphere-egu24(Oral Presentation)
4. Singh, M. K., Bhawana, B., & Bharti, R. (2024, July). Snow Grain Size Mapping Using Prisma Hyperspectral Data over the South Lhonak Glacier. In IGARSS 2024-2024 IEEE International Geoscience and Remote Sensing Symposium (pp. 3682-3685). IEEE. (Poster Presentation)
5. Singh, M. K., & Bharti, R. (2024, December). Snow Geophysical Parameters Retrieval Using Prisma Hyperspectral Data Over the South Lhonak Glacier Region 2024 IEEE India Geoscience and Remote Sensing Symposium (Oral Presentation). 2 – 5 December 2024, Goa, India (Accepted: Oral Presentation)
6. Bhawana, Anilkumar, Ritu., Singh, M. K., & Bharti, R. (2024, December). Snow Depth Modelling Using Hybrid Optical – SAR Approach 2024 IEEE India Geoscience and Remote Sensing Symposium (Oral Presentation). 2 – 5 December 2024, Goa, India (Accepted: Oral Presentation)